INFORMATION TO USERS

This reproduction was made from a copy of a manuscript sent to us for publication and microfilming. While the most advanced technology has been used to photograph and reproduce this manuscript, the quality of the reproduction is heavily dependent upon the quality of the material submitted. Pages in any manuscript may have indistinct print. In all cases the best available copy has been filmed.

The following explanation of techniques is provided to help clarify notations which may appear on this reproduction.

1. Manuscripts may not always be complete. When it is not possible to obtain missing pages, a note appears to indicate this.
2. When copyrighted materials are removed from the manuscript, a note appears to indicate this.
3. Oversize materials (maps, drawings, and charts) are photographed by sectioning the original, beginning at the upper left hand corner and continuing from left to right in equal sections with small overlaps. Each oversize page is also filmed as one exposure and is available, for an additional charge, as a standard 35mm slide or in black and white paper format.*
4. Most photographs reproduce acceptably on positive microfilm or microfiche but lack clarity on xerographic copies made from the microfilm. For an additional charge, all photographs are available in black and white standard 35mm slide format.*

***For more information about black and white slides or enlarged paper reproductions, please contact the Dissertations Customer Services Department.**

U·M·I Dissertation Information Service

University Microfilms International
A Bell & Howell Information Company
300 N. Zeeb Road, Ann Arbor, Michigan 48106

8614675

Garland, Denise Andrea Cave

ELECTRON SPIN RESONANCE STUDIES OF MATRIX ISOLATED LITHIUM METAL CLUSTERS

City University of New York PH.D. 1986

University
Microfilms
International 300 N. Zeeb Road, Ann Arbor, MI 48106

ELECTRON SPIN RESONANCE STUDIES OF MATRIX ISOLATED LITHIUM METAL CLUSTERS

by

Denise Andrea Cave Garland

A dissertation submitted to the Graduate Faculty in Chemistry in partial fulfillment of the requirements for the degree of Doctor of Philosophy, The City University of New York.

1986

This manuscript has been read and accepted for the Graduate Faculty in Chemistry in satisfaction of the dissertation requirement for the degree of Doctor of Philosophy.

4/21/86
date

Chairman of Examining Committee

4\22\86
date

A. M.
Executive Officer

Professor Max Diem, Hunter College

Professor John Lombardi, City College

Supervisory Committee

The City University of New York

To my parents.

You can't always get what you want!
You can't always get what you want!
You can't always get what you want!
But if you try,
Sometimes,
You just might find,
Just might find,
You get what you need!

M. Jagger

Forward Ho!

In this final stage of my dissertation I feel like a mountain climber who's reached a summit. I'm winded and the view is more obscured by clouds and other peaks than I had anticipated. But the air is invigorating and the day is bright. And while I may stand here by myself, I have a warm appreciation that my graduate education and this thesis would not have been so readily accomplished without the care and consideration of many people.

First, I wish to thank my mentor, Derek M. Lindsay, for his unobtrusive guidance and his ability to turn an equation into a picture. There are no words!

I also wish to thank my parents, Doris and Frederick H. Cave Jr., for their support and shelter. Without them neither I nor this thesis would be here. Also my second parents, Dr. John and Kay Garland, for their kindness and encouragement. My daughter, Tamara Lynne, for having the grace to make it through adolescence without making me totally bananas. My aunt and cousin, Hazel and Vernon Smith, for giving me a great reason not to spend all my Sundays in the lab. And the rest of my family for their support and tolerance.

Along the way I've had the great good fortune to find some very fine friends, June Ruszkowski, Jackie Downs and Faythe Weaver, who I hope will always want to help me keep my sense of humor, sense of perspective and appreciation of the absurd!

I am especially indebted to Dr. David Locke, who, as Executive Officer, encouraged me to enter the graduate program, and as a valued professor, provided not only sound advice but a gift for dancing through the administrative bureaucracy. I also wish to thank Dean K. Harrison of the Office of Expanded Educational Opportunity, and Dr. Donald Sloan of the Northeast Regional Research Center for Science and Engineering, for making sure I didn't starve to death as a graduate student.

I also wish to thank my colleagues, George Thompson, Karl Kernisant, Peter Brennan, and David Chang, with whom I enjoyed writing equations on the backs of napkins during "Miller Time".

Finally, no matter how many good friends help belay you, or how many others are out there on the cliff face with you, you're the only one making your climb. So, last, but not least, I want to thank myself. Today the Catskills! Tomorrow the Alps!

dag

TABLE OF CONTENTS

CHAPTER PAGE

TABLE OF CONTENTS

LIST OF TABLES

CHAPTER PAGE

LIST OF TABLES

LIST OF TABLES

LIST OF FIGURES

LIST OF FIGURES

LIST OF FIGURES

Chapter One

INTRODUCTION

The main topic of this thesis is the electron spin resonance (ESR) study of bare Lithium metal clusters isolated in rare gas matrices. An additional project involved the production and examination of the superoxide adduct of Lithium. The ESR technique was used, obviously because that was the instrumentation available, and, more significantly, because it provides a subtle yet potentially decisive probe of the molecular geometry and electronic wave function through minimally perturbing low energy magnetic interactions with the species of interest. The obvious disadvantage is the paramagnetic requirement. Alkali atoms have single valence s-orbital electron so that only the atoms and the odd numbered neutral aggregates have transitions that are ESR visible. Lithium superoxide forms a charge transfer pair, $Li^{+}O_2^{-}$, where Lithium, although it now lacks an unpaired electron, can still interact with the transferred electron through its nuclear spin magnetic moment.

Small, neutral, ligand free (or "bare") metal clusters of less than 25-30 atoms have become the recent focus of interest, especially as models for elucidating such phenomena as chemiabsorption processes, catalytic activity, and phase transitions from molecular to bulk metal properties (1-5). Research was stimulated in the mid 1970's by the development and improvement of molecular beam and matrix isolation techniques which allowed more efficient production and observation of metal clusters (6). Molecular beam studies have the advantage that the clusters are in the gas phase and are not, therefore, perturbed by any interactions with a matrix. The cryogenic conditions of matrix isolation, however, insure that the clusters are in their lowest electronic and vibrational energy states. In molecular beam work, vibrationally excited and low lying metastable states are often produced (7). In matrix isolation work, while molecular rotations are not unknown for small molecules such as H_2O, HCl, NH_2, NH_3, and CH_3, no evidence of rotationally excited states were observed for the Lithium species reported here.

Matrix isolation allows the study of unstable, short lived or highly reactive species in a leisurely manner since, once trapped, they can be isolated for as long as the matrix is maintained (8). A major disadvantage arises from the unavoidable guest-host interactions between the trapped species and the matrix. These interactions can be minimized by using inert gases for the matrices. However, matrix perturbations may still be large enough to significantly distort the ground state geometry (9). By studying the species of interest in several matrices and/or over a range of temperatures, it is sometimes possible to determine the degree of guest-host interaction (10), including variations in symmetry and coordination associated with multiple trapping sites. On one hand, invariance of molecular parameters to changes in matrix conditions offers strong support that they represent fundamental molecular properties rather than matrix induced effects. On the other hand, a current goal of cluster research is to develop a scale of guest-host interactions and use this to evaluate and ultimately predict the role of metal-support effects in various phenomena (11-13).

There are several recent comprehensive reviews of metal cluster spectroscopy (14-18) that reflect the growth in this field. However, at the beginning of this project experimental information was limited to several dissociation energies studies (19), UV-Visible absorption experiments (20), vibrational frequencies from 2-photon ionizations (21) and ionization potential values from single-photon photoionizations studies of Sodium and Potassium cluster (22). ESR spectra of matrix isolated Na_3 and K_3 obtained by Lindsay *et al* (23-27) augered well for a similar synthesis and study of the Lithium trimer.

Li_3 is the simplest triatomic molecule capable of being chemically bonded (28) since both H_3 and He_3 do not have formal bonds. By the early 1980's a number of theoretical calculations had been done for the Li_3 system, but there was no consensus as to the ground state geometry (29-31). The isolation of Li_3, even in a matrix could assist in solving the controversy. Almost concurrently with the ESR studies of alkali trimers appeared more sophisticated *ab initio* calculations on the potential energy surfaces of the Lithium and Sodium trimers. These predicted that the surfaces were relatively flat, consisting of three shallow wells separated by low energy saddle points ($\tilde{}$100-300 cm^{-1}) and that the trimer should be able to *pseudorotate* among the wells (32,33). *Pseudorotation* was observed in the ESR studies of the alkali timers. Indeed, experimentally, Li_3 was found to be a totally fluxional molecule with its ground vibronic level lying above the saddle point barrier energy between the wells. The Li_3 work was complemented on either side by the study of a larger cluster, Li_7 and the observation of Lithium atoms in multiple trapping sites.

A second project involved the examination of the triatomic LiO_2 molecule. The alkali superoxides have been extensively studied and a great deal is known about their ground state geometry (34). ESR data is available on the heavier alkali superoxides, but the values for LiO_2 were only tentative because of low intensity signals and poor resolution of transitions (35,36). Of main interest was deducing the crystal field splitting parameter, δ, for LiO_2 and comparing it with those of the other alkali superoxides.

Chapter Two

THEORY

II.1 Introduction

The power of any experiment is the theory behind it and through which a cohesive explanation of the data can be provided. ESR has been around since 1944 when Zavoisky first experimented with $CuCl_2 \cdot H_2O$, and, as expected, there is a wealth of texts that do an excellent job of presenting the theory in various degrees of rigor and detail (16,36-45). Therefore, only a rudimentary summary is attempted here.

Like all spectroscopy, ESR monitors net absorptions of energy from a radiation field when atoms or molecules change their energy state. A rigorous description of ESR theory must come from quantum theory, however, useful analogies can be drawn from classical physics. The basic logic is that a paramagnetic atom or molecule behaves as if it were a small bar magnet and when placed in a strong applied static magnetic field will align itself so that its field is either parallel or anti-parallel to that of the applied field. The difference in energy, ΔE, between the two alignments is a function of the strength of the applied field. If an oscillating magnetic field is applied in a direction perpendicular to that of the static field, and if its energy matches ΔE through the relationship

$$\Delta E = h\nu \qquad [2.1]$$

it will interact with the paramagnet and induce a transition between the two alignment states. The energy required to cause this transition, or *spin flip*, can be modified by any additional local fields such as those arising from nuclei with magnetic moments, or neighboring unpaired electrons, as well as being a function of the applied static field.

In quantum mechanics, the energy operator, or *Hamiltonian*, *H*, is the sum of the potential and kinetic energy of the system. For eigenfunctions, ψ_k, the *Hamiltonian* is

$$H\psi_k = E_k\psi_k \qquad [2.2]$$

If the *Hamiltonian* describes several independent, noninteracting systems, such as the electronic structure due to the motion of the electron and its attraction to the nucleus, and the spin energy in an applied magnetic field, then the total energy is the sum of the individual energies expressed by the *Hamiltonian* and the total wave function is the product of the wave functions of the individual parts of the system.

$$H_{tot} = H_1 + H_2 \qquad (H_1,H_2) = 0 \qquad [2.3]$$

The *Hamiltonians*, H_1 and H_2 commute with each other and with the total *Hamiltonian* and, therefore, have simultaneous eigenvalues.

$$H_1\psi_n = E^1_n\psi^1_n \qquad H_2\psi_m = E^2_m\psi^2_m \qquad [2.4]$$

and

$$H_{tot}\psi_{tot} = E_{tot}\psi_{tot} = (E_n+E_m)\psi_{tot} \qquad [2.5]$$

where $\psi_{tot} = \psi_n\psi_m$.

The total wave function, ψ_{tot}, is the product of the individual wave functions, and the total energy, E_{tot}, is the sum of the individual energies.

If there is an interaction between the two components of the *Hamiltonian*, a third component, H_{12}, is introduced so that

$$H_{tot} = H_1 + H_2 + H_{12} \qquad [2.6]$$

H_{12} produces off-diagonal elements in the *Hamiltonian* energy matrix. ψ_{tot} of the noninteracting system is no longer an eigenfunction of the *Hamiltonian* and the matrix must be diagonalized in order to find the correct eigenvalues.

The total *Hamiltonian* for a molecule can be divided into two parts. One part represents the energy arising from the interaction with a magnetic field, H_{mag}, and the other part represents the energy the system would have in the absence of the field, H_o.

$$H_{tot} = H_o + H_{mag} \qquad [2.7]$$

The pertinent interactions of H_{tot}, collected in H_{mag}, form the *Spin Hamiltonian*, H_S.

$$H_{mag} = H_{LS} + H_Z + H_{hf} + H_Q + H_{ZN} \qquad [2.8]$$

where

H_{LS} is the spin-orbit term, $\sum_i \zeta(r_i)\vec{l}_i \cdot \vec{s}_i$, and has a value of ~$10^2$ - 10^4 cm^{-1}.

H_Z is the Zeeman term which contains the orbital as well as the electronic component, $\beta_e \vec{H} \cdot \sum_i (\vec{l}_i + g_e \vec{s}_i)$ and has a value of ~1 cm^{-1}.

H_{hf} is the nuclear hyperfine term which is a sum of three components and has a value of ~10^{-1} - 10^{-3} cm^{-1}.

$$g_e\beta_e g_n\beta_n \sum_i \left(\frac{\vec{l}_i\cdot\vec{I}}{r_i^3} + \vec{s}_i\cdot\left(\frac{3\vec{r}_i\cdot\vec{r}_i}{r_i^5} - \frac{\tilde{1}}{r_i^3}\right)\cdot\vec{I}_i + \frac{8\pi}{3}\vec{s}_i\cdot\vec{I}_i\cdot\delta(\vec{r}_i) \right).$$

H_Q is the quadrupole term, $\vec{I}\cdot\tilde{Q}\cdot\vec{I}$, and has a value of ~$10^3$cm^{-1}.

H_{ZN} is the nuclear Zeeman term, $g_n\beta_n\vec{H}\cdot\vec{I}$, and has a value of ~$10^{-4}$ cm^{-1}.

II.2 Spin Hamiltonian

The *Spin Hamiltonian* can be written as

$$H_S = \beta_e\vec{H}\cdot\tilde{g}\cdot\vec{S} + \vec{S}\cdot\tilde{A}\cdot\vec{I} + \vec{I}\cdot\tilde{Q}\cdot\vec{I} + g_n\beta_n\vec{H}\cdot\vec{I} \qquad [2.9]$$

where the first term combines matrix elements of the spin--orbit, orbital and electronic Zeeman terms of H_{mag} into a single term. The electron's spin is not quantized along the magnetic field vector $\vec{H}$, but is coupled to it through the molecular framework as represented by the $\tilde{g}$ tensor.

The second term is the nuclear hyperfine interaction, $\mathcal{H}_{hf}$. The third and fourth terms are the same as in Eq.[2.8].

The simplest description of the interaction between a magnetic dipole moment vector, $\vec{\mu}$, and an external magnetic field vector, $\vec{H}$, is given by the *Hamiltonian*

$$\mathcal{H} = -\vec{\mu}\cdot\vec{H} \qquad [2.10]$$

For the case of an electron, $\vec{\mu}$ has two possible components. The first arises from the intrinsic angular momentum, $\vec{S}$, of the electron

$$\vec{\mu}_S = 2(-\frac{e}{2mc})\vec{S} \qquad [2.11]$$

The second occurs if the electron also has an orbital angular momentum, $\vec{L}$

$$\vec{\mu}_L = -\frac{e}{2mc}\vec{L} \qquad [2.12]$$

where $\vec{S} = \sum_i \vec{s}_i$, $\vec{L} = \sum_i \vec{l}_i$, e is the charge of the electron, m its mass, and c the speed of light. Classically, the electron can have any energy described by

$$E = -\mu H\cos\theta \qquad [2.13]$$

where θ is the angle between the vectors. Quantum mechanically, however, θ is space quantized so that only certain energies are allowed. A quantum system with total angular momentum vector $\vec{J}$ can be described by the total angular quantum number, J. All that can be measured with certainty with respect to the vector, is its square, J^2, and one component, arbitrarilly labeled J_z. As a consequence of the Uncertainty Principle, it is impossible to have complete knowledge of the direction of the angular momentum vector. For a particular system, the magnitude of J_z can have any of 2J+1 values given by the quantum number M_J, where

$$M_J = J\hbar,\ (J-1)\hbar, \ldots.,\ -J\hbar \qquad [2.14]$$

The magnitude of J^2 is $J(J+1)\hbar^2$. $\hbar = h/2\pi$.

The magnetic moments in Eqs.[2.11] and [2.12] can be represented quantum mechanically by replacing the coefficients with $g_e\beta_e/\hbar$ and $g_L\beta_e/\hbar$ respectively. The Bohr magneton, $\beta_e = e\hbar/2mc = 9.2470 \times 10^{-21}$ erg Gauss^{-1}. For a free electron, $g_L = 1$ and $g_e = 2.00232$. The deviation of g_e from the classical value of 2 is due to a relativistic correction.

Angular momentum vectors are individually quantized. Thus, the allowed projections of the orbital angular momentum vector $\vec{L}$ are given by the 2L+1 values of the orbital angular quantum number M_L, and those of the spin vector, $\vec{S}$, by M_S. For a single electron, the spin quantum number is $S = 1/2$ and S_z has the two possible values, $M_S = +1/2\ \hbar$ and $-1/2\ \hbar$. The magnitude of S^2 is $3/4\ \hbar^2$ and the magnitude of the vector $\vec{S}$ is $(\sqrt{3}/2)\hbar$. In the absence of orbital angular momentum, the two energy levels for the electron in a magnetic field with component H_z, along an arbitrary direction z, are given by the electronic Zeeman term

$$H = g_e \beta_e M_S H_z = E_{M_S} \qquad [2.15]$$

and the energy difference between the two levels is

$$\Delta E = E_{M_{S=+1/2}} - E_{M_{S=-1/2}} = g_e \beta_e H_z = h\nu \qquad [2.16]$$

where ν is the microwave frequency at which transitions between the two levels occurs. Typically, ν is fixed for a given spectrometer and the field, H_z, is varied until the resonance condition is satisfied.

Orbital angular momentum is rarely completely missing or *quenched*. The deviation of the experimental g value from g_e is a measure of the extent of the orbital interaction. In the conventional description for the magnetic interactions of a "free atom", such as a gas phase atom, not subject to external fields from a molecular or crystalline environment, the spin and orbital angular momenta couple to give a resultant which is a constant of the motion. For orbitally degenerate atomic states, $(L\neq 0)$, with Russell-Saunders coupling, $\vec{J} = \vec{L} + \vec{S}$. The Wigner-Eckart Theorm allows the spin orbit interaction, H_{LS}, to be rewritten as

$$\sum_{i}\zeta(\vec{r}_i)\vec{l}_i\cdot\vec{s}_i = \lambda\vec{L}\cdot\vec{S} \qquad [2.17]$$

where λ is the spin-orbit coupling constant, and allows the orbital and spin Zeeman terms to be rewritten as

$$\vec{L} + g_e\vec{S} = g_J\vec{J} \qquad [2.18]$$

The first term of Eq.[2.9] is represented by the *Hamiltonian*

$$H = g_J\beta_e\vec{H}\cdot\vec{S} \qquad [2.19]$$

with energy levels given by

$$E_{M_J} = g_J\beta_e M_J H_z \qquad [2.20]$$

where the Landé g factor

$$g_J = 1 + \frac{S(S+1) + J(J+1) + L(L+1)}{2J(J+1)} \qquad [2.21]$$

gives the classical free electron value $g = 2$ when $L = 0$.

For a ^2S atom, there will be a single transition at a magnetic field value corresponding to the particular g_J of the atom and the frequency of the spectrometer. Not much information outside of the g_J value can be gleaned from the single transition, and ESR spectra would be pretty boring if this were the only magnetic interaction possible. Fortunately, this is not the case and other interactions, especially those between the electron and surrounding nuclei, increase the number of transitions possible and, thereby, the amount of information. If the nucleus has a nonzero magnetic moment, $I \neq 0$, this can interact with the electron's moment to split the ESR signal into 2I+1 hyperfine components, M_I, where I is the nuclear spin quantum number. This means the electron "sees" 2I+1 local contributions to the overall magnetic environment in addition to that of the external static field. This produces 2I+1 fields at which resonance can occur.

In polyatomic molecules and solids, $\vec{L}$ and $\vec{S}$ are uncoupled. The orbital motion of the electron is quenched through the electrostatic interaction with the lattice of the nuclei. The orbital angular momentum operator does not commute with the total *Hamiltonian* and, therefore, can't form simultaneous eigenstates with the energy of the system. That is, the orbital motion is not in a stationary state and is not an eigenvalue of the system. The orbital motion is affected by it's orientation relative to the x, y, and z axes of the molecule. In molecules with cubic or tetrahedral symmetry, the orbital motion is affected isotropically by the nuclear fields. In systems with axial symmetry, two of the directions, arbitrarily x and y, are equivalent and the third, z, is different. Finally, in systems with no symmetry, the electron's orbit is quenched to different extents about each molecular axis. The transition field position depends on the competition between the effect which tends to quench the orbital angular momentum, and the effect that tends to generate it. The dynamics of these effects are buried in the details of the $\tilde{g}$ tensor given by the first term of Eq.[2.9].

If the orbital angular momentum is completely quenched, the electron possesses only spin angular momentum and the $\tilde{g}$ tensor is isotropic and has the the free electron value $g_e = 2.00232$. Therefore, if $\tilde{g}$ is anisotropic, then $\vec{S}$ can not represent the true electron spin, but reflects a "fictitous" spin that includes the contributions from the orbital motion (39). Indeed, magnetic interactions that involve the orbital angular momentum of the electron are the sole source of deviation of g from g_e; and since the orbital angular momentum depends on the chemical environment of the atom, molecule or crystal, the g value(s) reflect the paramagnet's environment. There are two magnetic interactions involving the orbital angular momentum. The first is the spin-orbit coupling interaction

$$\mathcal{H}_{SO} = \zeta\vec{L}\cdot\vec{S} \qquad [2.22]$$

which arises because the electron "sees" a magnetic field due to the nuclear orbital motion. The second interaction is with the external magnetic field

$$\mathcal{H}_{ZO} = \beta_e\vec{L}\cdot\vec{H} \qquad [2.23]$$

where the larger the expectation value of the orbital angular momentum L, the greater the shift in g. The direction of the shift depends on the sign of the spin-orbit coupling constant, ζ. If ζ is positive, then g is generally less than g_e.

The coupling of the electronic and nuclear spins is represented by the second term in Eq.[2.9], $\vec{S}\cdot\bar{A}\cdot\vec{I}$. The hyperfine interaction actually has two components, an isotropic or Fermi contact term, A_{iso}, and an anisotopic or dipolar term, A_{dip} contained in the tensor $\vec{A}$. The hyperfine *Hamiltonian* can be expressed as

$$H_{hf} = [A_{iso} + A_{dip}]\vec{S}\cdot\vec{I} \qquad [2.24]$$

The structure due to the Fermi term arises from the interaction of the nuclear magnetic moment with the magnetic field produced at the nucleus by the electric current of the electron cloud. The *Hamiltonian* for this interaction is

$$H_{iso} = a\vec{I}\cdot\vec{S} = a(I_xS_x + I_yS_y + I_zS_z) \qquad [2.25]$$

where a is the isotropic hyperfine coupling constant and is proportional to the square of the amplitude of the electronic wave function at the nucleus

$$a = A_{iso} = \frac{8\pi}{3}g_e\beta_e g_n\beta_n|\psi(0)|^2 \qquad [2.26]$$

The sign of a depends on the sign of g_n and on the sign of the spin density. The expression is integrated over the coordinates of the electron, therefore, the contact term has a nonzero value only when the electron has a finite probability density at the nucleus, i.e. has s-orbital character.

The dipole interaction term is analogous to the classical interaction energy between two magnetic moments, $\vec{\mu}_e$ and $\vec{\mu}_n$.

$$E = \frac{\vec{\mu}_e \cdot \vec{\mu}_n}{r^3} - \frac{3(\vec{\mu}_e \cdot \vec{r})(\vec{\mu}_n \cdot \vec{r})}{r^5} \qquad [2.27]$$

where $\vec{r}$ is the radius vector from $\vec{\mu}_e$ to $\vec{\mu}_n$, and r is its magnitude. The quantum mechanical version has $\vec{\mu}_e = -g_e\beta_e\vec{S}$ and $\vec{\mu}_n = g_n\beta_n\vec{I}$ so that

$$\mathcal{H}_{dip} = -g_e\beta_e g_n\beta_n(\vec{I}\cdot\vec{S} - 3(\vec{I}\cdot\vec{r})(\vec{S}\cdot\vec{r})) \qquad [2.28]$$

where

$$A_{dip} = g_e\beta_e g_n\beta_n\left\langle\frac{3\cos^2\theta - 1}{2r^3}\right\rangle \qquad [2.29]$$

This is averaged over the entire probability distribution, $|\psi(\vec{r})|^2$, of the unpaired electron and averages to zero whenever the electron cloud has spherical symmetry.

Eq. [2.24] can be rewritten in tensor form

$$\mathcal{H}_{hf} = \vec{I}\cdot(A_{iso}\tilde{1} + \tilde{T})\cdot\vec{S} \qquad [2.30]$$

where

$$\tilde{A} = \begin{bmatrix} A_{iso} & 0 & 0 \\ 0 & A_{iso} & 0 \\ 0 & 0 & A_{iso} \end{bmatrix} + \begin{bmatrix} T_x & 0 & 0 \\ 0 & T_y & 0 \\ 0 & 0 & T_z \end{bmatrix}$$

Each diagonal element in the traceless tensor $\bar{T}$ is

$$T_i = -g_e\beta_e g_n\beta_n \frac{<r^2 - 3i^2>}{r_5} \qquad [2.31]$$

where i = x,y, or z.

For nuclei with nonzero nuclear spins, the energy levels can be further perturbed by the interaction between the nucleus and the external field. This nuclear Zeeman interaction is given by the last term in Eq.[2.9] and is analogous to the electronic Zeeman term but is typically ~3 orders of magnitude less. For the Lithium systems reported in this thesis the nuclear Zeeman, as well as the quadrupole term, are neglected.

II.3 Resonance Conditions and Transition Field Positions

As previously noted, the magnetic field value at which transition occurs depends on the frequency pf the spectrometer. Line positions must be independent of the spectrometer used. However, different spectrometers operate at different frequencies. Even for a given instrument, the frequency may vary with cavity conditions and temperatures. Consequently, neither the field value H, nor the frequency ν, can be used seperately to give the line position. Instead, the g value is used, which is essentially the ratio of the frequency to the field at resonance.

ESR spectra can be taken under three conditions of the external magnetic field, the weak field, the strong field, and the intermediate field strength cases.

(i) <u>Weak Field</u>: The splitting due to the external field, $\vec{H}$, is small with respect to the splitting due to the field independent hyperfine term. That is, for some general angular momentum vector, $\vec{J}$,

$$a\vec{I}\cdot\vec{J} > g_J\beta_e\vec{H}\cdot\vec{J} \qquad [2.32]$$

In this case, $\vec{I}$ and $\vec{J}$ couple to give a resultant vector, $\vec{F} = \vec{I} + \vec{J}$. F is the good quantum number and its 2F+1 projections are given by $M_F = F, F-1, \ldots, -F$.

(ii) <u>Strong Field</u>: Here the splitting due to $\vec{H}$ is greater than the hyperfine splitting, i.e.

$$g_J\beta_e\vec{H}\cdot\vec{J} > a\vec{I}\cdot\vec{J} \qquad [2.33]$$

This decouples $\vec{I}$ and $\vec{J}$ making them good quantum numbers, and replacing M_F with M_I and M_J to give (2I+1)(2J+1) levels. That is, each M_J value has a complement of M_I levels.

(iii) Intermediate Field: The Zeeman and hyperfine splittings are the same order of magnitude. In the limiting cases, it approaches either the M_F or the $M_J + M_I$ regime.

All spectra presented here were obtained under strong field conditions. This is also called the *high field approximation*. Fig.II.1 shows the effect of the magnetic field strength on the energy levels of a ^2S atom such as ^6Li where $I = 1$ and $S = 1/2$. The states are labeled in both the weak field basis, $|F,M_F>$, and the high filed basis, $|S,M_S,I,M_I>$.

The general solution for the magnetic energy levels for a two spin system using the *Hamiltonian* in Eq.[2.9] and ignoring the quadrupole term, can be evaluated in the $|S,M_S,I,M_I>$ basis (46). For the hyperfine interaction, the I_zS_z terms of the expansions in Eqs.[2.25] and [2.26] act to perturbe the zero order wave functions and give the first order hyperfine energies. The remaining terms, I_xS_x and I_yS_y, mix wave functions to produce the second order changes in the energies. By appropriately ordering the basis functions, the *Hamiltonian* can be block diagonalized into a set of pure states represented by 1x1 matrices, and a seies of mixed states represented by 2x2 matrices. The diagonal elements are given by

$$\langle S,M_S,I,M_I|\ \mathcal{H}_S\ |S,M_S',I,M_I'\rangle =$$

$$g_e\beta_e H M_S \delta_{M_S M_S'} + g_n\beta_n H M_I \delta_{M_I M_I'}$$

$$+ (A_{iso} - 2A_{dip}) M_S M_I \delta_{M_S M_I'} \delta_{M_I M_S'} \qquad [2.34]$$

The off-diagonal elements are given by

$$\langle S,M_S,I,M_I|\ \mathcal{H}_S\ |S,M_S-1,I,M_I+1\rangle =$$

$$1/2\ \{(S+M_S)(S-M_S+1)(I-M_I)(I+M_I+1)\}^{1/2} \times (A_{iso} + A_{dip}) \qquad [2.35]$$

and

$$\langle S,M_S,I,M_I|\ \mathcal{H}_S\ |S,M_S+1,I,M_I-1\rangle =$$

$$1/2\ \{(S-M_S)(S+M_S+1)(I+M_I)(I-M_I+1)\}^{1/2} \times (A_{iso} + A_{dip}) \qquad [2.36]$$

When the external field is very large, the off-diagonal elements, which are field independent, can be neglected. Using this approximation the eigenvalues can be read off of the diagonal of the matrix.

The ESR selection rules $\Delta M_I = 0$ and $\Delta M_S = \pm 1$, are evident from examining the above three equations and understanding the probability of transition. In the ESR experiment, the slowly swept static field lifts the magnetic degeneracy of the states and produces the Zeeman levels. Transitions between these levels are accomplished by a second, oscillating field, $\vec{H}_{osc.}$, provided by the standing microwaves produced in the cavity by the klystron. The transition probability is given by

$$P = |g\beta_e \langle M_S, M_I| \; \vec{S} \cdot \vec{H}_{osc} \; |M_S', M_I'\rangle|^2 \qquad [2.37]$$

where g is assumed to be isotropic, and the basis functions are abbreviated since S and I are constant for a given molecular state. If $\vec{H}_{osc}$ is parallel to the static field, $\vec{H}_{ext}$, say along the z-axis, it can only interact with the S_z spin component. Since $S_z|M_S\rangle = M_S|M_S\rangle$, P is nonzero only if $M_S = M_S$ and $M_I = M_I$. That is, no transition occurs and $\vec{H}_{osc}$ only serves to modulate the Zeeman levels. However, if $\vec{H}_{osc}$ is perpendicular to $\vec{H}_{ext}$, say along the x-axis, it will interact with the S_x spin component. Since $S_x = 1/2(S_+ + S_-)$, $S_x|M_S\rangle = 1/2(|M_S-1\rangle + |M_S+1\rangle)$ and P is nonzero only when $M_S = M_S \pm 1$.

For the Lithium atom, the dipolar term of the hyperfine interaction in zero. Further, the nuclear

Zeeman term can be neglected. The six energy levels associated with ^{6}Li are represented in Fig.II.2. The field positions for the corresponding transitions, given to second order, are

$$H(I,M) = \frac{g_e}{g_o}(H_e - a_o M) + \frac{(g_e a_o)^2}{g_o} \frac{(I(I+1)-M^2)}{2H(I,M)} \qquad [2.38]$$

where H(I,M) is the observed line position, in Gauss. For molecules, relace I with J, the sum of the nuclear spins of each set of j equivalent nuclei, and aM with the sum $\Sigma a_j m_j$, taken over the set of j magnetic nuclei.

Figure II.1 Zeeman energy level diagram for a ^2S, I=1 atom such as ^{6}Li.

$$h\nu = H + aM_I + \tfrac{1}{2}\{I(I+1) - M_I^2\}\frac{a^2}{(H+h)} + \tfrac{1}{2}M_I\{M_I^2 + \tfrac{1}{2} - I(I+1)\}\frac{a^3}{(H+h)^2}$$

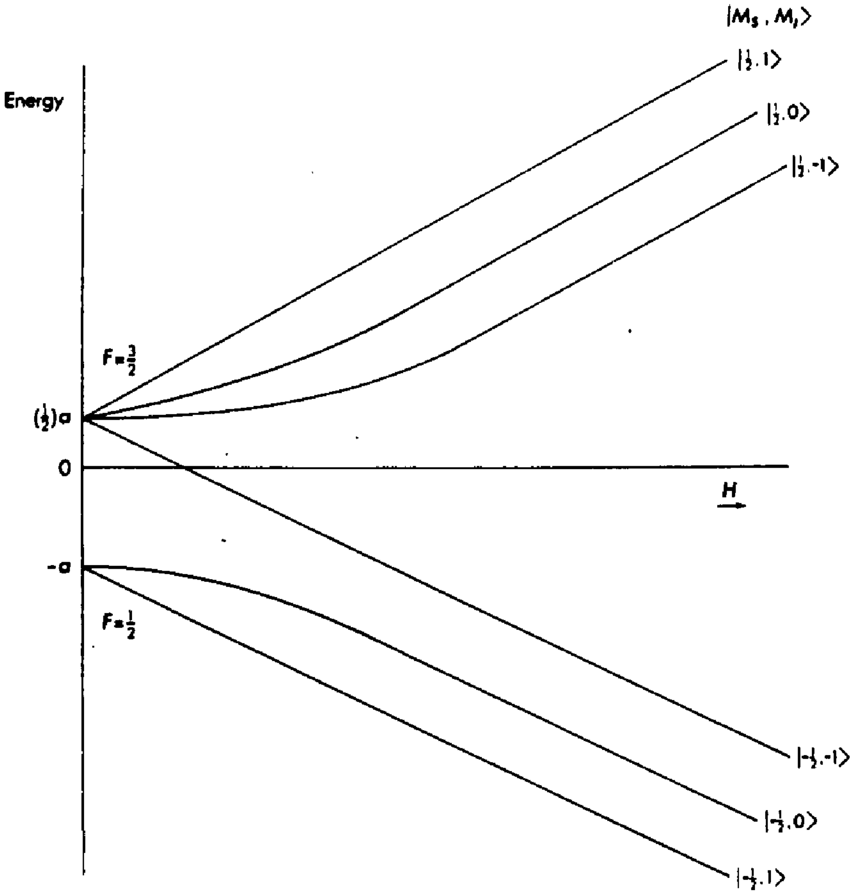

Figure II.2 Diagram of the energy levels and corresponding *Spin Hamiltonian* matrix elements for a ^2S, I=1 atom such as ^{6}Li.

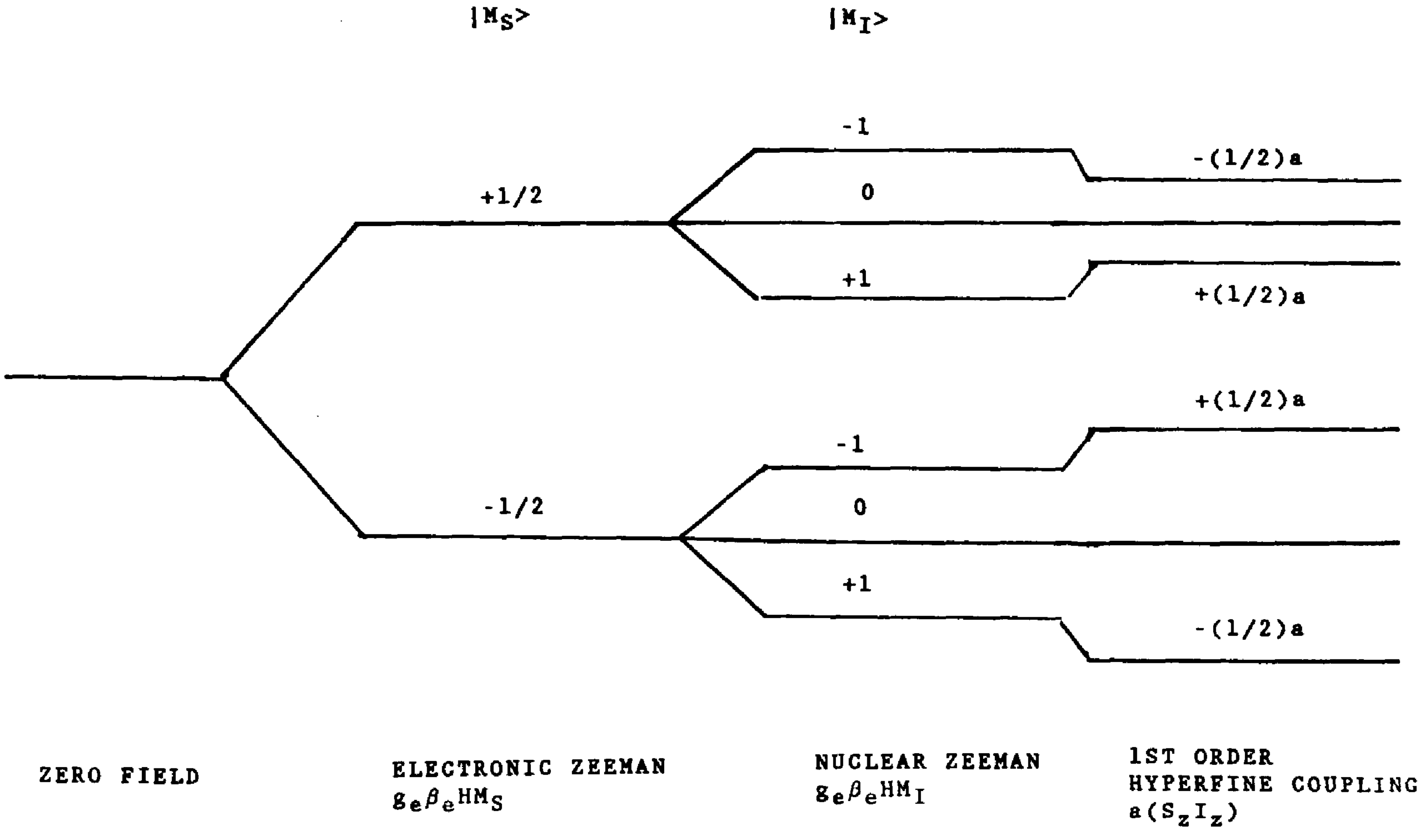

Chapter Three

EXPERIMENTAL

III.1 Introduction

Lithium species of interest were formed by conventional matrix isolation methods. Metallic Lithium was vaporized from a Knudsen type effusion source and codeposited with an excess amount of some nonreactive gas. The two beams intersect on a liquid helium (LHe) cooled target surface mounted within an ESR cavity. At the cryogenic surface, the vapors rapidly condense and individual atoms and molecules of Lithium are "trapped" in the frozen matrix. Solidification is not instantaneous and reactive atoms may aggregate into small clusters via diffusion. The high dilution provided by the matrix, however, effectively prevents aggregation into the bulk metal. Diffusive aggregation during deposition can be increased by having the modulation power on during deposition, or by maintaining the target surface at a temperature above 4.2°K. Once deposition is completed, aggregation can sometimes be facilitated by annealing and/or photolyzing the matrix sample. For example, the Lithium trimer is not generally evident in samples prior to photolysis. Also, LiO_4 signals are frequently observed after annealing samples containing LiO_2.

Annealing is accomplished by gradually warming the matrix to approximately 1/3 of the matrix gas' melting point. During the resulting "softening" the matrix atoms tend to orient themselves to form the regular lattice structure (hcc for noble gas solids) associated with the pure solid. This forces the trapped species into a smaller number of preferred lattice positions and their transition signals generally become narrower and easier to observe.

The matrix gases used most often were Argon, Krypton, and Nitrogen. A small number of experiments were done using Neon and Xenon. These two were more difficult to work with. Neon, because of its low heat capacity and high scattering ratio (9) tended not to stick to the target. Since the m.p. of Neon is only about 25°K, annealing above 9 or 10°K produced serious boil off. Those matrices that did form were easily degraded by minor changes in cavity temperature. The problem with Xenon is that natural abundance samples contain 26.4% of ^{129}Xe with I=1/2 and 21.1% of ^{131}Xe with I=3/2. Signals from trapped species were greatly attenuated by the resulting dipolar broadening.

Natural abundance Lithium contains two isotopes: 92.58% of ^{7}Li with I=3/2 and 7.42% of ^{6}Li with I=1.

Table III.1 Lithium Properties.

Isotope	Natural Abundance %	Nuclear Spin, I	Magnetic Moment[a]		Quadrupole ($10^{-21} cm^2$)	Gas Phase hf, Gauss
			g_n	μ_n		
^7Li	92.58	3/2	2.1707	3.2560	-3×10^{-2}	143.4
^6Li	7.42	1	0.82192	0.82192	$+6.9 \times 10^{-4}$	54.3

(a) g_n is in units of $_n$; $=gI$ (scalar).

Note: The ratio of $^7g_n/^6g_n = {}^7a/^6a = 2.64$

Table III.2 Materials Used.

Material	Supplier	Purity, %
^{nat}Li	Alfa Chemicals	99.9
^{7}Li	ORNL[(a)]	99.9
^{6}Li	ORNL	98
Argon	Airco	99.998
Krypton	Airco	99.995
Nitrogen (N_2)	Airco	99.9995
Xenon	Airco	99.995
Neon	Matheson	99.99
Oxygen (O_2)	Matheson	99.997

(a) Oak Ridge National Laboratories.

Figure III.1 Schematic of experimental apparatus.

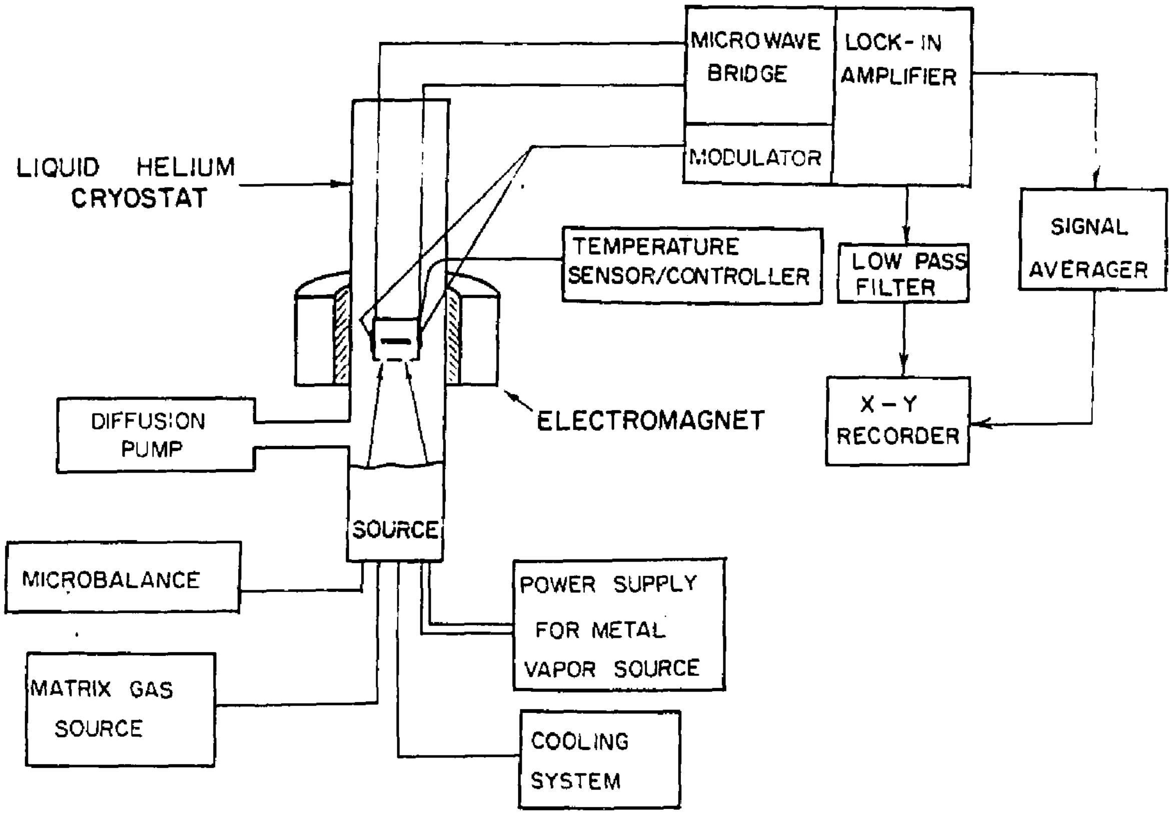

III.2 Experimental Apparatus

A schematic of the operating system is shown in Fig.III.1. Only a brief description of the major commercial components is given here since details are readily available from the manufacturers' manuals. More detail is supplied for those components that were modified to better suit the experimental requirements.

III.2.1 Spectrometer and Magnet

Two commercial ESR spectrometers were used during the course of these experiments. Most of the spectra presented in this thesis were obtained using a JEOLCO-ME-3X Spectrometer (47). In September 1983, it was replaced with an IBM-Bruker ER 2000 ESR Spectrometer (48). Most of the LiO_2 data was obtained with this latter system. The IBM-Bruker was substantially less temperamental than the older JEOLCO. Not only was tuning easier to accomplish and maintain, but there was an approximately three fold increase in sensitivity.

Both spectrometers were standard x-band instruments with the klystron locked to the sample cavity by either a hybrid-T bridge or a three port circulator with directional coupler. The AFC stabilized klystron supplied monochromatic radiation at a frequency of ~9.2 GHz with a maximum power output of ~200 mW. Typically 0.5-1.0 mW of microwave power was incident on the cavity. The microwaves pass through a mica window and into the resonance cavity via a length of evacuated rectangular wave guide. The guide and cavity are both enclosed in the cryostat. An iris is present between the end of the wave guide and the cavity.

The reference arm of the spectrometer was tuned at ~4.2°K to the resonance frequency of the unloaded cavity (i.e. before deposition). The ability of the cavity to respond to an absorption of energy is represented by the quality, Q, of the cavity. The larger the value of Q, the more sensitive the cavity is to small changes in the energy absorbed. The customized cavity used had an estimated Q of 3500-4500 (36). After deposition, Q has changed and the cavity is no longer balanced to the reference arm. At resonance the misbalance in output between the microwaves reflected back from the cavity and the unattenuated value in the reference arm is detected by a semiconducting diode.

Unless the sample has a very high concentration of paramagnets, the signal can be weak and easily masked by noise. To overcome this, an oscillating magnetic field at a known frequency is superposed on the static field. When the static field passes through a resonance, the modulating frequency is superposed on the ESR absorption signal. A 100 kHz modulation is supplied by customized low impedance modulation coils mounted on the cavity (36).

This field has a peak-to-peak amplitude range of 0.25-5.0 Gauss. When the static field sweeps through a resonance value absorption occurs and a signal is generated at 100 kHz with an amplitude proportional to the first derivative of the absorption signal. The signal now goes through a lock-in-amplifier that acts as a phase sensitive detector to give a dc output. The detector is only sensitive to an input frequency at or near the modulation frequency. Since only a small fraction of random noise is expected to have this frequency the signal-to-noise ratio, S/N, increases and weaker intensity transitions can be resolved. The final signal is either plotted directly on an XY recorder or stored digitally on a signal averager (Tracor-Northern model 1710-4K). The recorder and the signal averager are interfaced to an IBM-9000 minicomputer so that spectra can be further processed.

The static magnetic field source for both spectrometers was a JEOLCO magnet and power supply. This is a water cooled low impedance electromagnet with a field range of 0 to 10 kG. The homogeneity of the field depends on the pole diameters and and gap width. The flat polecaps are 300mm in diameter. The original air gap of 60mm was widened to 90mm to accommodate the tail of the dewar. The field was relatively stable and linear over the range 3.5 kG ± 1 kG used in these experiments, although transient "jitter" as well as field drift occurred with the JEOLCO spectrometer. This reduced the efficiency of signal averaging in some experiments. However, since all spectra were individually calibrated using a proton magnetometer (Micronow, model 515), any transient field instabilities were not expected to compromise the accuracy of field positions assigned to transitions. The resonance frequency of the cavity plus sample was monitored using a microwave frequency counter (Hewlett-Packard, model 5245L plus HP5255A plug-in). Relative and absolute field positions were judged accurate to ±0.5% and ±1.0G respectively for the JEOLCO spectrometer and to ±0.2% and ±0.5G for the Bruker spectrometer.

III.2.2 The Dewar

The liquid Helium cryostat used for these experiments is a customized modular variant of an Andonian 3-litre Dewar (Adonian Associates Inc., Waltham, Mass.). An exhaustive description of the engineering and construction details is given in Ref. 36. A schematic of the dewar is shown in Fig.III.2. The dewar has an upper section that is essentially a reservoir and temperature sink. Below this is a smaller "working tail" where the resonance cavity and vaporization source are located. The dewar consists of five concentrically nested modules. From the outside in, first, of course, is an outer vacuum jacket.

This is followed by a liquid Nitrogen (LN_2) reservoir and a second vacuum jacket. Next is a two stage liquid Helium (LHe) chamber. The upper reservoir has an ~2 1/2 litre capacity and is the reservoir proper. Below it is a smaller LHe "tail" with a capacity of ~1/2 litre. The two are connected by a variable position valve that allows the tail reservoir to be evacuated of LHe so that variable temperature experiments can be performed on the matrix sample. Finally, running down the center of the apparatus is a length of evacuated waveguide to which the resonance cavity is attached.

Variable temperature work was monitored by several different systems over the course of these experiments. Initially, a Carbon resistor, calibrated at three fixed points (4.2°K, 77°K, 300°K) and rated accurate to ±5%, was used. The calibration scheme is given in Ref. 36. This was later replaced by a factory calibrated Germanium resistance thermocouple (Cryocal Inc., St. Paul, Minn.) with a rated precision of ±0.0005°K. The final system consisted of a Gallium-Arsenide diode, with a precision of ±0.2°K, interfaced to s Series 5500 Microprocessor Based Temperature Indicator/Controller (Scientific Instruments, Inc., West Palm Beach, Fl.). This system gives the easiest and most comprehensive dewar tail temperature

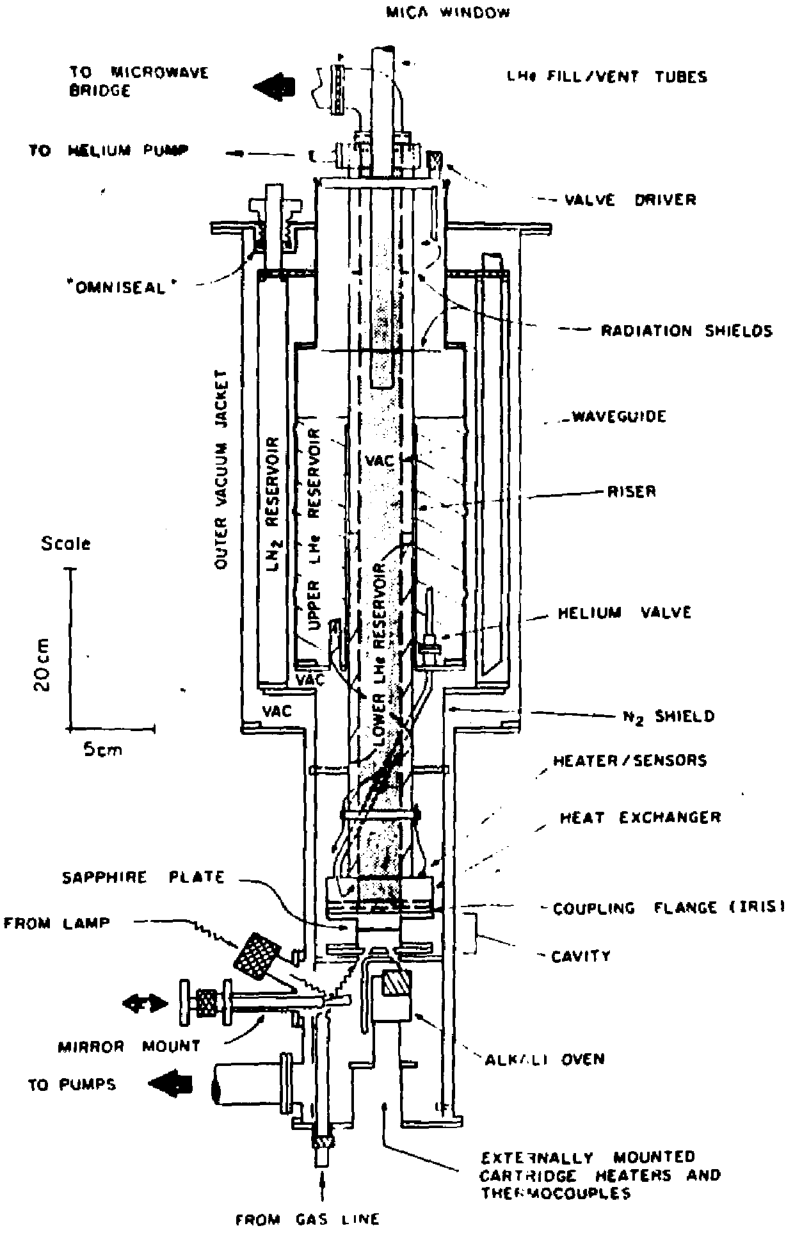

Figure III.2 The Liquid Helium Dewar.

control, providing for maintenance of selected temperatures as well as for small step-wise changes in temperature. All the temperature transducers were mounted on a heat exchanger connected to the cavity and not at the target surface itself. Because of this, reported temperatures are really "nominal" values although there is not expected to be more than a 1 or 2 °K difference between the two points. Temperature gradients as well as significant heat loads to the cavity arise from the elevated temperatures of the incoming gases, the current in the modulation coils surmounting the cavity, and the microwave power from the klystron that is dissipated in the cavity walls.

III.2.3 Resonance Cavity and Target

The resonance cavity used is a custom built TE_{102} type. The cavity designation gives the type and pattern of the internal field set up in the cavity. This rectangular model provides a transverse electric field mode (i.e. having no z-component of the electric field). The subscripts give the number of 1/2 period variations of the electric field along the x,y, and z axes, respectively, of the cavity. The cavity is constructed of brass and Gold plated to increase the reflectivity. The cavity quality factor is in the range Q ~ 3500-4500 (36). The value is temperature dependent and increases as T decreases. The cavity is mounted to a heat exchanger at the end of the microwave guide. The target plate on which the sample is deposited sits within the cavity between the modulation coils. Two types of target plates were used. The first was a sapphire plate 0.021" thick. A sample of the spectrum for this target is given in Fig.III.3. The transitions observed are due to impurities and the pattern is unique to each sapphire crystal. The patterns for all targets used were accurately recorded at 4.2°K prior to deposition so that transitions due to sapphire impurities were easily distinguished from those of the matrix sample. The particular plate shown in Fig.III.3 was used extensively. Most of the experimental data, including all the bare cluster work as well as the initial LiO_2 data were taken using this plate. The strong downfield pair of peaks was used to optimized the tuning of the spectrometers. The actual positions and intensities of the impurity signals changed slightly whenever the plate was remounted after removal from the cavity for repairs or cleaning. This is because a slight variability is possible in the mounting position of the target in the cavity. This plate was relatively clear in the $g = 2$ region as seen in the smaller region scanned in Fig.III.4. The resonance field of the free electron, H_e, in the cavity had a steady value of 3312.3 G when the sapphire

Figure III.3 Sapphire plate background spectrum taken at ~4.2°K. This is a 6000 G scan centered at 3000 G. The scan time was 200 sec. with a 100msec time constant, 2 G modulation, and ~1mW microwave power.

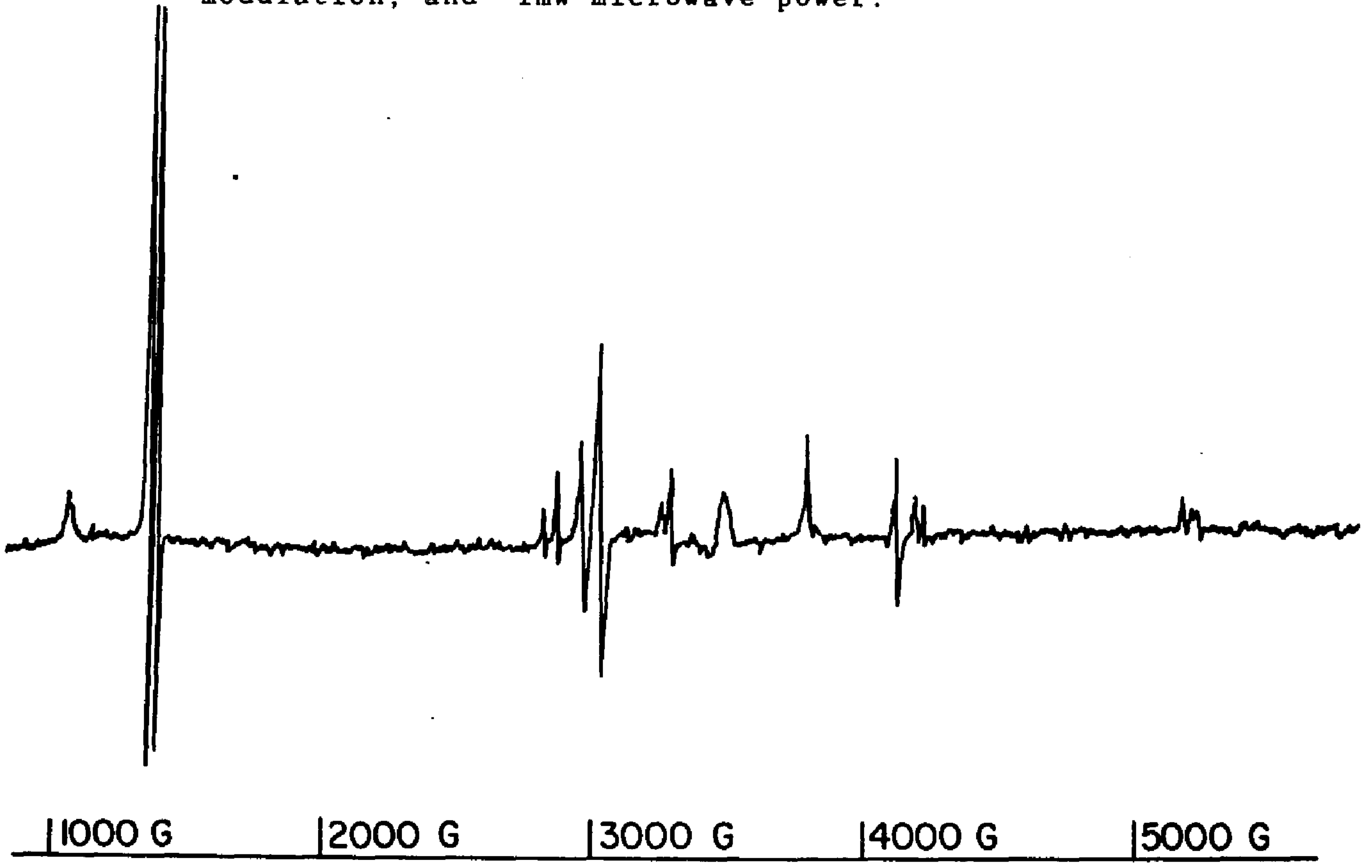

Figure III.4 Sapphire plate background spectrum taken at ~4.2°K. This is a 500 G scan centered at 3300 G (~g=2). The scan time was 200 sec. with a 100msec time constant, 2 G modulation, and ~1mW microwave power.

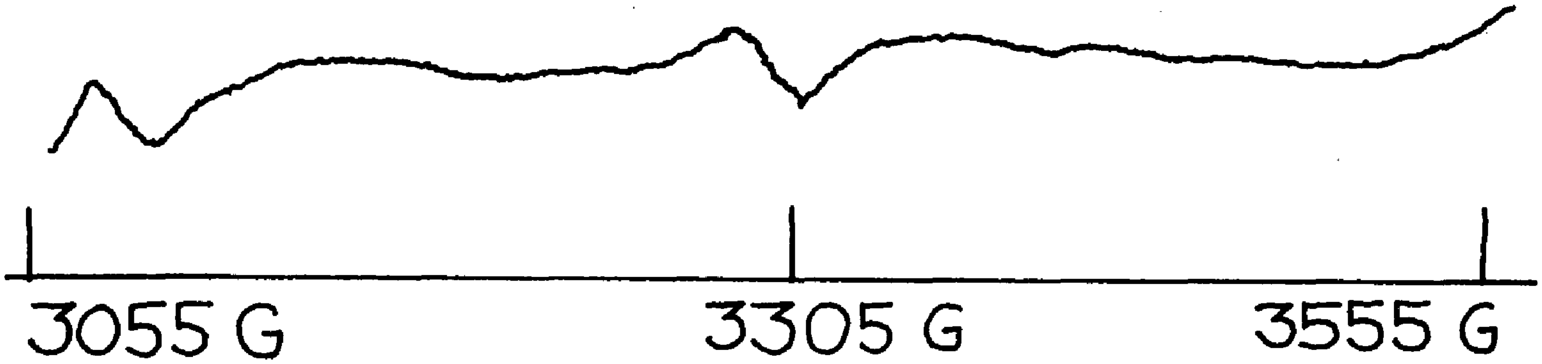

Figure III.5 Copper plate backgound spectrum taken at ~4.2°K. This is a 6000 G scan centered at 3000 G. The scan time was 10 min. with a 500msec time constant, 2 G modulation, and ~1mW microwave power.

target was used. This value varied by less than ±0.5G over the 4-77°K range and did not change significantly upon deposition.

The second target was a Copper plate, 0.031" thick. This target had a counterbored hole in its center to accommodate a 0.094" diameter quartz window. This allowed the target to be used by other experimenters doing optical absorption studies. This target was introduced in an attempt to improve the thermal contact between the plate and cavity to facilitate the growing of Neon matrices. A typical 4.2°K background spectrum for the Cu target is shown in Fig.III.5. The free electron field value had a value of 3320.4 G ± 0.5 G.

III.2.4 <u>The Effusion Source</u>

Lithium is evaporated from a Knudsen effusion source. This source is the same one originally described in detail in Ref.36, but with several modifications added. The stainless steel source consists of a block containing a tubular hole in which metal to be vaporized is placed. Vaporization occurs by resistive heating of this block (65 W resisitor, Hottwatt, Inc.). The metal vapor is collimated into a beam by passing through a slit block that fits atop the oven block. The slit is independently heated using a second 65W resistor to prevent it from clogging during deposition. An input tube carries the matrix (and any additional reactive) gases into the source chamber. This tube ends in a slit that directs the matrix gas so that its beam crosses that of the metal vapor's at the surface of the target plate in the cavity. For Argon, this effusion slit allows $\tilde{}10^{15}$ molecs/sec into the cavity.

During the experiments an intermittent "thermal short" developed, but when the source was removed from the dewar and examined nothing appeared to be wrong. The problem was eventually traced to a hard solder joint in the oven block. The source is a "low temperature" furnace originally designed to vaporize the higher weight alkali metals (Na→Cs). Lithium has the highest m.p. of the alkali series and suitable vapor fluxes required that the source be heated to temperatures of >500°C. At the higher temperatures needed to get suitable Li vapor pressures, the solder softened and the oven block "bowed" and made thermal contact with part of the LN_2 shield. This problem was eliminated by adding a water cooled shield around the source. Schematics of the source are given in Fig.III.6 and 7. A second problem was the production of a black, laminar, "sooty" appearing deposit on the oven block and inside the water cooled shield during Lithium vaporization. This deposit clogged the slit block and seriously attenuated the Li beam reaching the target.

Figure III.6 The effusion source. Front view of slit block. Side view of oven block.

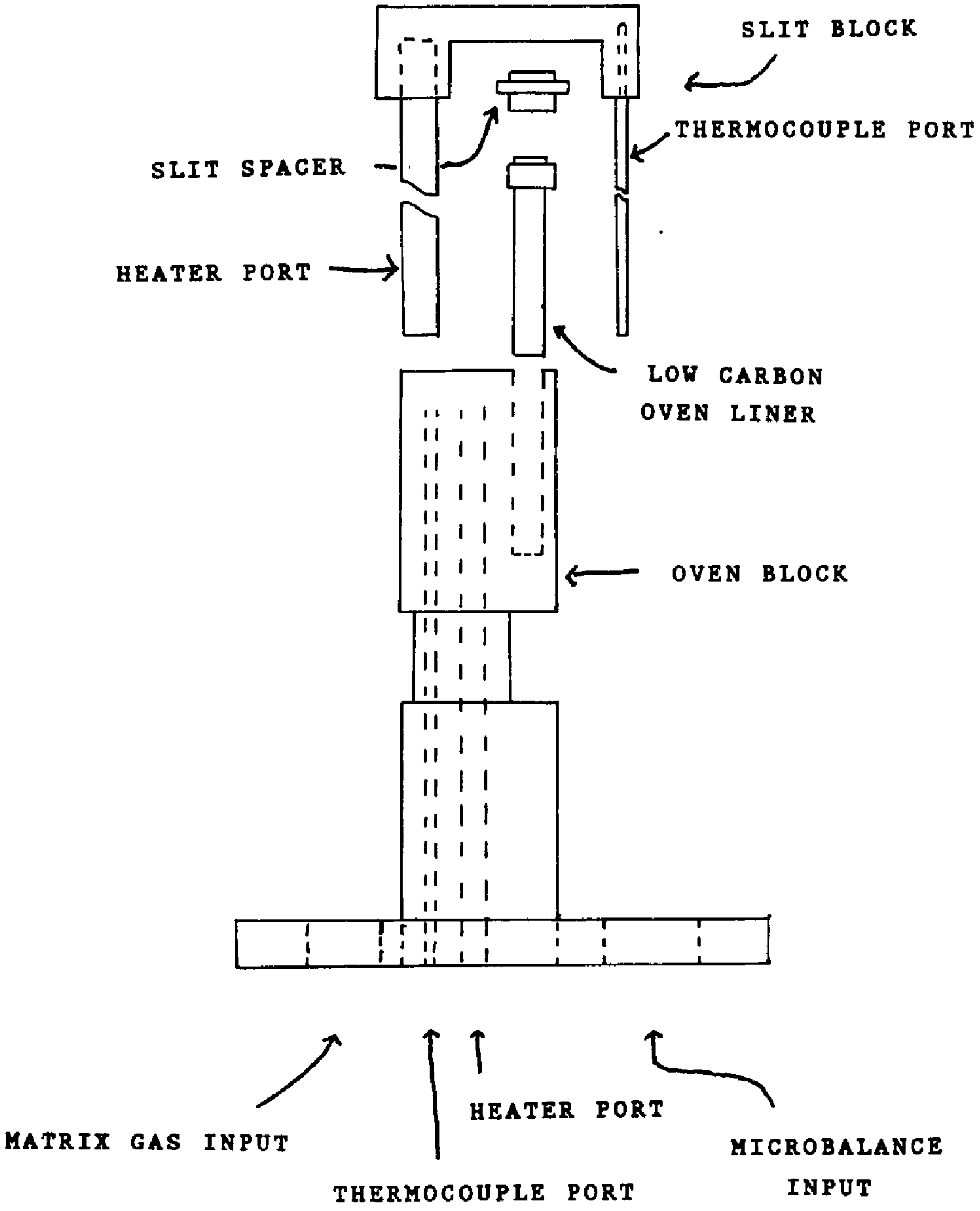

Figure III.7 Side view of source showing the water cooled shield and quartz microbalance.

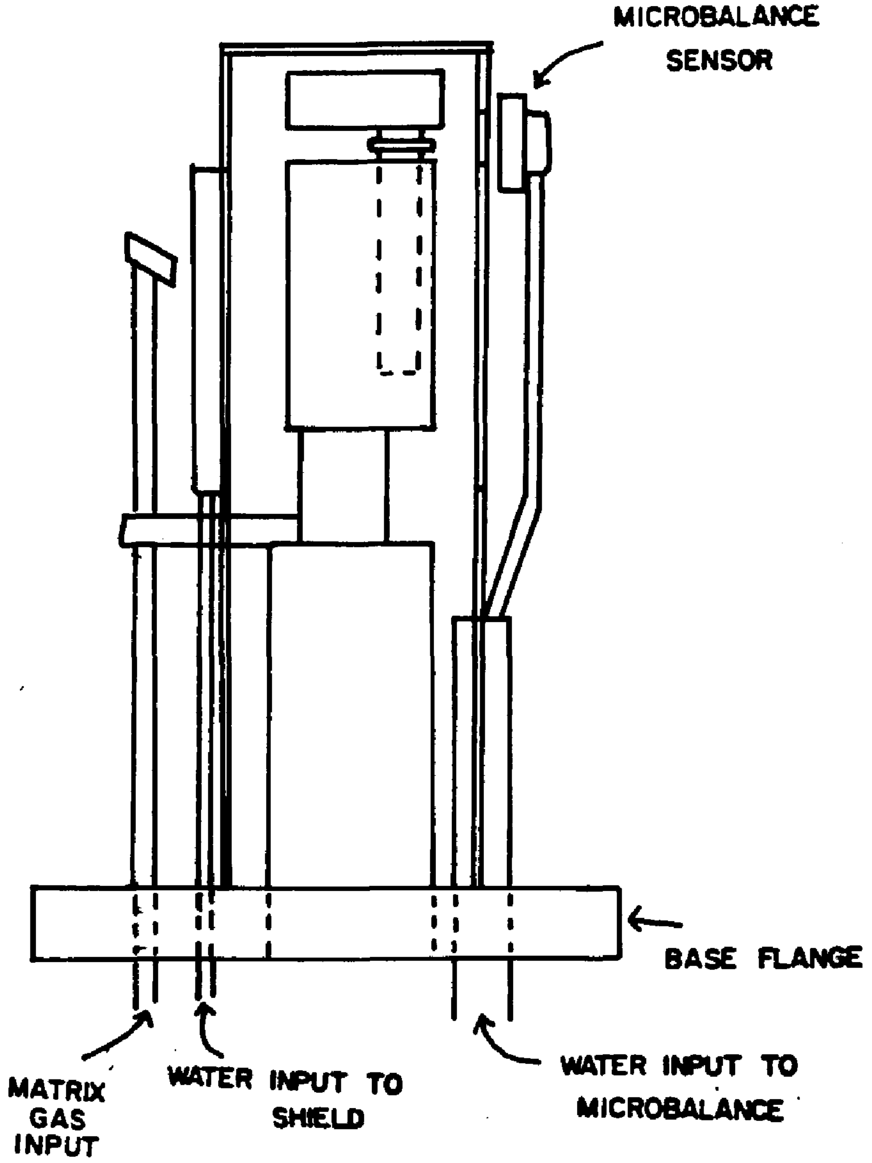

Since Lithium is capable of leaching Carbon out of steel, these deposits may have been graphite. The problem was eliminated by placing Li into a low Carbon steel liner (SS 303, 4% Carbon) before placing it in the oven block.

The final modification to the source was the addition of a quartz microbalance to directly monitor the Lithium vapor fluxes.

III.2.5 Monitoring Fluxes

Two fluxes were involved in these experiments, that of the matrix gas and that of the Lithium vapor. The details of the gas line input are given in Ref.36, and the matrix gas flux is expressed by

$$F_{mat} = 6.14 \times 10^{17} \frac{P}{(MT)^{1/2}} \qquad [3.1]$$

where P is the pressure, in Torrs, behind the input slit. This pressure was monitored with a capacitance manometer (MKS Series 200, MKS Industries, Burlington, Mass.) that had a 10 Torr head and a 0.001 Torr precision rating. M is the gram molecular weight of the matrix gas, and T is the temperature in °K, assumed to be room temperature, of the input gas. A typical value for Argon where $P = 0.96$ Torr, $M = 40$ g mole^{-1}, and $T = 300$°K is

$$F_{Ar} = 5.38\text{x}10^{15} \text{ molecs sec}^{-1} \qquad [3.3]$$

The Lithium vapor fluxes were originally estimated from the Nesmeyanov Tables (49) that plot vapor pressure of metal vs temperature. A more accurate measure was obtained when a commercial quartz crystal microbalance (Veeco QM 301, Veeco Instruments, Inc., Plainview, N.Y.) was retractably mounted on the source flange. The microbalance was modified by water cooling the head. This was done to stabilize the readings and reduce the crystal failure rate by reducing the thermal shock to the crystal when it was raised to intercept the hot Lithium beam.

The flux, in A/sec, is read directly off of the microbalance unit. However, this reading has to be manipulated to get the actual flux of Li at the target plate. First, as shown in Fig.III.7, the quartz crystal is parallel to the actual Li beam. A pinhole in the slit spacer that sits between the oven and slit blocks allows some Li vapor to hit the crystal. This sampling, however, is perpendicular to the direction in which the Li beam is directed, so there is a geometric factor involved. The flux of Li at the cavity equals the geometric factor times the Li flux at the crystal. In addition, the microbalance is calibrated for Aluminum atoms (presumably because Al has ~ the same density as quartz), and must be adjusted for the difference between the densities of Al and Li. A sample calculation follows:

ρ_{Al} = 2.645 kg/l at 20°C

ρ_{Li} = 0.533 kg/l at 20°C

MWA_{l} = 26.98

MW_{Li} = 6.941

Diameter of microbalance crystal = 0.762 cm

Area of crystal = 0.46 cm^2

Volume/hour = (Flux)x(Area)

A flux of 2A/sec gives:

$$(Flux)(Area)(\rho_{Al})(MW_{Al}^{-1}) = 3.2 \text{ mole/hr of Lithium}$$

after appropriate unit conversions..

Chapter Four

BARE LITHIUM CLUSTERS

IV.1 Spectra and Analysis

ESR spectra were obtained for the Lithium atom, trimer and septemer species in Argon matrices. The atom and septemer signal intensities could be followed during the deposition. The timer signal was generally not evident prior to photolyzing the sample after deposition was completed. The relative intensities of the atom and septemer signals were used to find optimized conditions for producing both the trimer and septemer clusters. A summary of optimum deposition conditions is given in Table IV.1. A typical growth curve as a function of deposition time is presented in Fig. IV.1. The curve is for a ^{7}Li doped sample and follows the $M_I = +3/2$ transition for the atom and an arbitrary superhyperfine (shf) feature of the septemer. The graph is only qualitative because at the low resolution used for deposition time scans, the identity of the shf feature is not well established. Also, the relative intensities were not exactly the same for any two experiments or "runs". The growth curves were useful, however, in finding the point at which the growth rates tended to "plateau". Continued deposition after

Table IV.1 Lithium Cluster Deposition Conditions.

Cluster	Target T	Source T	Li v.p.(a)	Li flux (b)		Dep.Time	Ar:Li
	°K	°K		A/sec	mol/hr	hrs	
Li_3	4.2	450-500	1.0	0.5-1.5	0.1	5-7	75:1
Li_7	4.2-8.0	500-530	5.0	2.0-5.0	0.3	5-7	30:1

(a) Trimer conditions include 2-5 hr photolysis after deposition.

(b) Eq.[3.4].

Figure IV.1 Growth curve for the $M_I=+3/2$ transition of ^{7}Li, a shf transition of $^7Li_7$, and the bulk metal signal at g˜2.

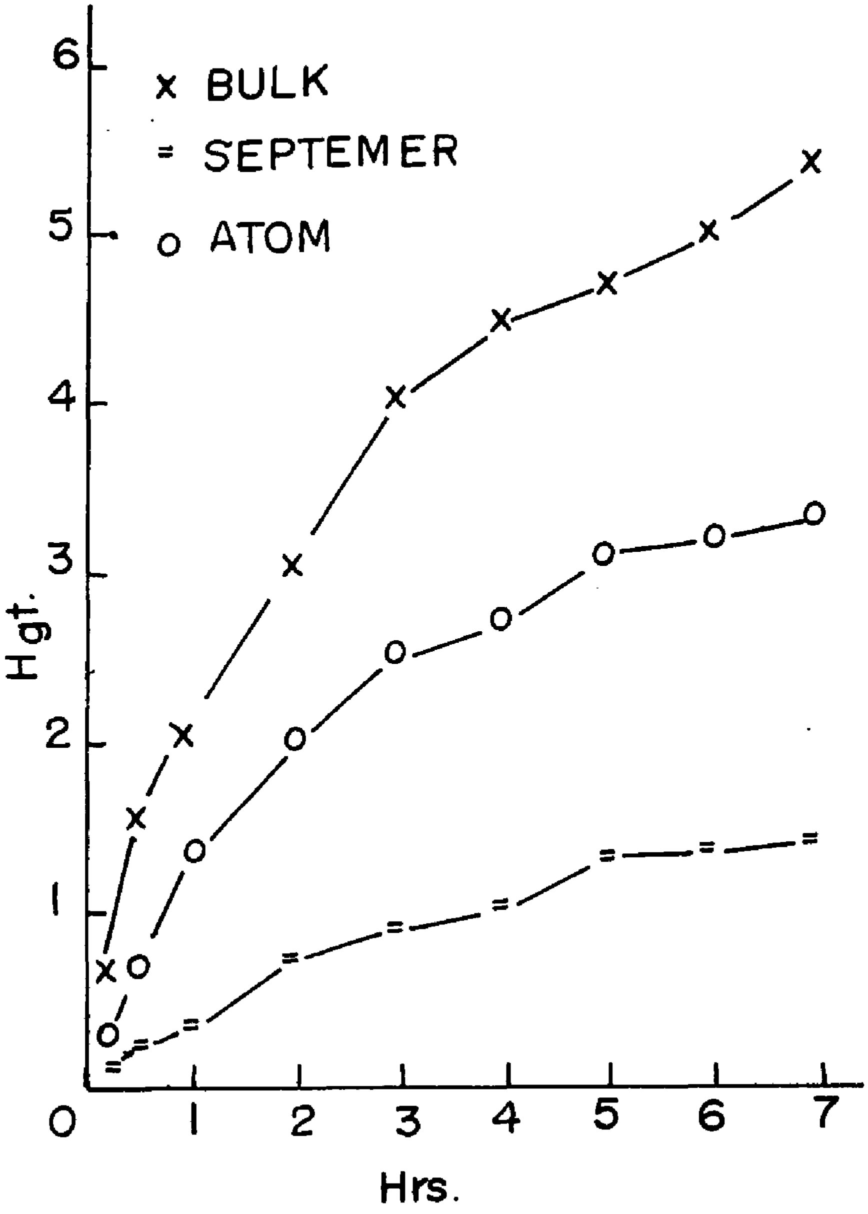

this point didn't produce significant increases in cluster intensities, but could be roughly correlated to increases in a broad feature at $g^{\sim}2$ probably associated with the formation of bulk Li metal.

All spectra were fit to the second order Breit-Rabi formula. For convenience and consistency with the published results (23-27,50-52), the notation used in applying the equation to each species is reviewed below:

(i) For atomic spectra the equation is used as written in Eq.[2.38].

(ii) For the trimer the first-order hf line positions are expressed by

$$H(M,m) = \frac{g_e}{g_o}(H_e - \sum_{i=1}^{3} a_i m_i) \qquad [4.1]$$

For the static trimer case, this becomes

$$H(M,m) = \frac{g_e}{g_o}(H_e - a_o M - a_3 m_3) \qquad [4.2]$$

where M is the sum of the magnetic quantum numbers of the equivalent nuclei, $M=m_1+m_2$, and $a_1=a_2=a_o$. The parameters for the nonequivalent third nucleus are m_3 and a_3. For the *pseudorotating* trimer,

$$H(M) = \frac{g_e}{g_o}(H_e - \bar{a}M) \qquad [4.3]$$

where $M=m_1-m_2-m_3$, the spin projection quantum number of the three equivalent nuclei, and the hf constant is expressed as the average

$$\bar{a} = (1/3)(a_1+a_2+a_3) \qquad [4.4]$$

(iii) For the septemer, Eq. [4.1] can be extended to include the second order hf interaction

$$H(J_1,M_1) = \frac{g_e}{g_o}(H_e - a_1M_1) - (1/2)(g_e/g_o)^2\frac{a_1}{H}(J_1(J_1+1) - M_1) \qquad [4.5]$$

where the subscript 1 refers to the set of nuclei producing the hf pattern. J is the total nuclear spin angular momentum for the equivalent nuclei, $\Sigma I_i \geq J$. Since M is the projection of J onto the magnetic field, $J \geq |M|$. Each transition with a given M is split into components with J ranging from $|M|$ to ΣI_i in integer steps.

Superimposed on each (J_1,M_1) hf transition is a superhyperfine (shf) pattern described by

$$H(M_2) = -(g_e/g_o)a_2M_2 \qquad [4.6]$$

where the subscript 2 refers to a second set of equivalent nuclei with $a_2 << a_1$.

The observed ESR transitions are fit to the appropriate form of Eq. 2.38 to provide the best fit values of the parameters g and a. The hfs constant is proportional to the spin density of the unpaired electron at a given nucleus (Eq. 2.23), and, therefore, can provide a description of its relative distribution over the molecular framework. This, in turn, can provide information on the geometry and bonding patterns of the species. To facilitate comparison of hf information for different species, the hf constant is expressed as the dimensionless spin population, ρ. This gives the probability of having the unpaired electron in the orbitals assigned to a given nucleus. This is done by taking the ratio of the experimental isotropic hfs constant to that of the gas phase atomic value. the gas phase isotropic hfs constants are $a(^6Li) = 54.29G$ and $a(^7Li) = 143.36G$ (53). There is some ambiguity in evaluating spin populations because of complications such as contraction of the atomic wave function on formation of the molecule, or matrix interaction effects. The assumption that these effects are either insignificant or consistent for different species is not necessarily true.

Additional information is contained in the line shapes and intensity distribution patterns. For the species reported in this section all transitions had clean first-derivative lineshapes characteristic of paramagnetic species with isotropic g tensors ($\tilde{g} = g\tilde{1}$) and hf tensors ($\tilde{A} = a\tilde{1}$).

IV.1.1 Lithium Atoms

The atomic ground state of Li is $^2S_{1/2}$. The four ESR transitions of ^{7}Li and the three of ^{6}Li have the strong first-derivative line shapes expected. The atoms were isolated in Argon in multiple matrix sites. Tables IV.2 and IV.3 present comparisons between the observed and calculated field positions for the major matrix site (Site I) of each isotope at 4.2°K. In Argon as many as 6-8 sites could be observed in some samples prior to annealing. Annealing reduced the number of sites to 1 or 2 major sites, where the second site, at 4.2°K, was generally 75-50% the intensity of the primary site, and 1 or 2 minor sites with intensities of less than 10% that of Site I. Once the sample was annealed the number of sites became invariant under further temperature changes. However, the g and a values as well as the relative intensities of the sites varied with temperature even after annealing. Table IV.4 summarizes the magnetic parameters for Site I of both isotopes at 4.2 and 30°K. Equally unpredictable were the changes in relative intensity between sites as a function of temperature.

Table IV.2 Comparison between the experimental and calculated line positions for ^{7}Li (Site I) in Argon at 4.2°K.

M_I	Experimental H(M), Gauss	Calculated H(M), Gauss	Difference
+3/2	3088.2	3088.2	0.0
+1/2	3231.1	3230.8	+0.3
-1/2	3378.7	3378.6	+0.1
-3/2	3533.5	3534.2	-0.6

Table IV.3 Comparison between the experimental and calculated line positions for ^{6}Li (Site I) in Argon at 4.2°K.

M_I	Experimental H(M), Gauss	Calculated H(M), Gauss	Difference
+1	3259.6	3258.8	+0.8
0	3315.1	3315.5	-0.4
-1	3371.9	3371.2	+0.7

Only the values for Site I are reported since they were the only ones consistently reproducible from one run to another. In all cases, however, the transition line width increased with increasing T. Shifts in intensity were reversible.

The multiple sites showed a variation in intensity as a function of photolysis time. Photolysis decreased the relative intensities of all sites. The changes were irreversible, in contrast to the case of thermal variation. The results were not quantitatively predictable. In some samples 4 hours of photolysis using a 150 W or 450 W Xenon arc lamp reduced major site intensity by less than 50% while in others the atom signals were "bleached" away to less than 5% of their prephotolysis intensities.

IV.1.2 Lithium Trimer

ESR spectra assigned to the *pseudorotating* trimer, p-$^6Li_3$, were obtained after photolyzing samples produce by codepositing either atomic ^{6}Li or ^{7}Li with Argon for ~5-7 hours at 4.2°. The Knudsen effusion source was run at ~450-500°C and produced a Lithium flux of ~0.1μmol/hr incident on the target sapphire plate. The average Ar:Li ratio was 75:1. Samples were annealed at ~31°K and then photolyzed at ~30°K for up to 4 hours. Although weak timer signals were observed in a few samples prior to.

Table IV.4 Magnetic parameters of ^{6}Li (Site I) and ^{7}Li (Site I) in Argon at 4.2°K and 30°K.

	Temp., °K	g	$\Delta g^{(a)}$ (-10^{4})	a, Gauss	ρ
^{6}Li	4.2	2.00011(1)	2.7	56.06(3)	1.03
^{6}Li	30.0	2.00038(7)		55.95(3)	1.03
^{7}Li	4.2	2.00019(2)	2.6	147.96(1)	1.03
^{7}Li	30.0	2.00045(4)		149.42(4)	1.04

$^{(a)}\Delta g = g(4.2°K) - g(30.0°K)$.

photolysis, generally, the signal was absent and grew in monotonically with photolysis time. Also present in the sample was the spectrum of a larger Li cluster, Li_7. Its intensity decreased with photolysis as the trimer signal grew in. Figure IV.2 shows typical changes in these two signals as a function of photolysis time.

Figure IV.3 shows the spectrum assigned to p-$^6Li_3$. It consists of seven equally spaced hyperfine transitions centered around g˜2. The spacing and line shapes indicate that the $\tilde{g}$ and $\tilde{A}$ tensors are essentially isotropic in character (38-42). The observed intensity distribution of 1.1:3.3:6.2:7.0:5.7:3.0:1.1 is excellent agreement with the 1:3:6:7:6:3:1 ratio expected for three equivalent I=1 nuclei. Careful examination of the downfield region showed no zero-field transitions or ΔM_S transitions greater than ±1, and supports the assignment of a doublet ground state to the trimer. The trimer occurred in three matrix sites, but the intensity pattern and line shapes of the minor sites were poorly resolved due to overlap with each other as well as with the more intense primary site and septemer signals. Table IV.5 lists the observed transition fields for the seven components along with their calculated positions.

Argon matrices doped with ^7Li produced a comparable spectrum of 10 equally spaced first-derivative transitions with intensities again in excellent agreement with the expected ratio of 1:3:6:10:12:12:10:6:3:1 for three equivalent I=3/2 nuclei. Table IV.6 compares the observed and calculated field positions of p-$^7Li_3$. Two of the trimer transitions were overlapped by the very intense ^{7}Li atom signals. The estimated field positions of these two transitions are given in parenthesis. The trimer again occurred in three matrix sites but resolution of the two weaker sites was even poorer than in the p-$^6Li_3$ case.

For both isotopes, the g and a values for the sites were invariant with temperature. However, the linewidths decreased monotonically and reversibly with increasing temperature. At temperatures above ~32°K the trimer intensity abruptly and irreversibly decreased by half. Typical values for these trends are listed on Table IV.7 for the M=+1 and M=0 components of p-$^6Li_3$. Γ_{pp} is the peak-to-peak linewidth, in Gauss, of the first derivative signal. The height is the the crest to trough value, in arbitrary units. The intensity is calculated as the square of the linewidth times the height and represents the area under the derivative. A graphical representation of the linewidth is given in Figure IV.4. The solid line is a least squares fit to the values. Figure IV.5 plots the intensity, as height, vs temperature. The intensity increased steadily for both components with a maximum at ~17±2°K, and then decreased.

Table IV.5 Comparison between the experimental and calculated field positions of p-$^{6}Li_3$ (Site I) in Argon at 4.2°K.

M	Experimental H(M), Gauss	Calculated H(M), Gauss	Difference
+3	3274.9	3274.8	+0.1
+2	3287.1	3287.2	-0.1
+1	3299.3	3299.2	+0.1
0	3311.5	3311.5	0.0
-1	3323.7	3323.8	-0.1
-2	3335.8	3335.8	0.0
-3	3348.1	3348.0	+0.0

Table IV.6 Comparison between the experimental and calculated field positions of p-$^7Li_3$ (Site I) in Argon at 4.2°K.

M	Experimental H(M), Gauss	Calculated H(M), Gauss	Difference
+9/2	3166.3	3166.9	-0.6
+7/2	3199.1	3199.0	+0.1
+5/2	(3230.8)	3231.2	-0.4
+3/2	3263.2	3263.4	-0.2
+1/2	3295.7	3295.6	+0.1
-1/2	3327.7	3327.8	-0.1
-3/2	3360.0	3360.0	0.0
-5/2	3392.3	3392.2	+0.1
-7/2	3424.3	3424.4	-0.1
-9/2	(3456.3)	3456.6	-0.3

Table IV.7 Intensity changes in the M=+1 and M=0 components of p-$^{6}Li_3$ as a function of temperature.

Temp. °K	M=0			M=+1		
	Γ_{pp},G	Hgt.	Area	Γ_{pp},G	Hgt.	Area
28.7	0.49	2.16	0.52	0.49	1.97	0.47
25.3	0.56	2.35	0.73	0.56	2.12	0.66
22.1	0.70	3.60	1.76	0.56	2.72	0.85
19.4	0.70	3.03	1.49	0.56	2.72	0.85
16.3	0.70	2.86	1.40	0.56	2.73	0.86
14.8	0.77	2.68	1.59	0.70	2.78	1.36
13.9	0.77	2.43	1.44	0.83	2.45	1.69
11.2	0.90	1.76	1.43	0.80	1.87	1.20
9.0	1.06	1.03	1.16	0.87	1.10	0.83
6.5	-	-	-	0.93	0.48	0.42

Figure IV.2 Relative intensities of the M=-1 and M=-2 components of $^6Li_3$ and the M_I=-1 group of shf components of $^6Li_7$ as a function of photolysis time.

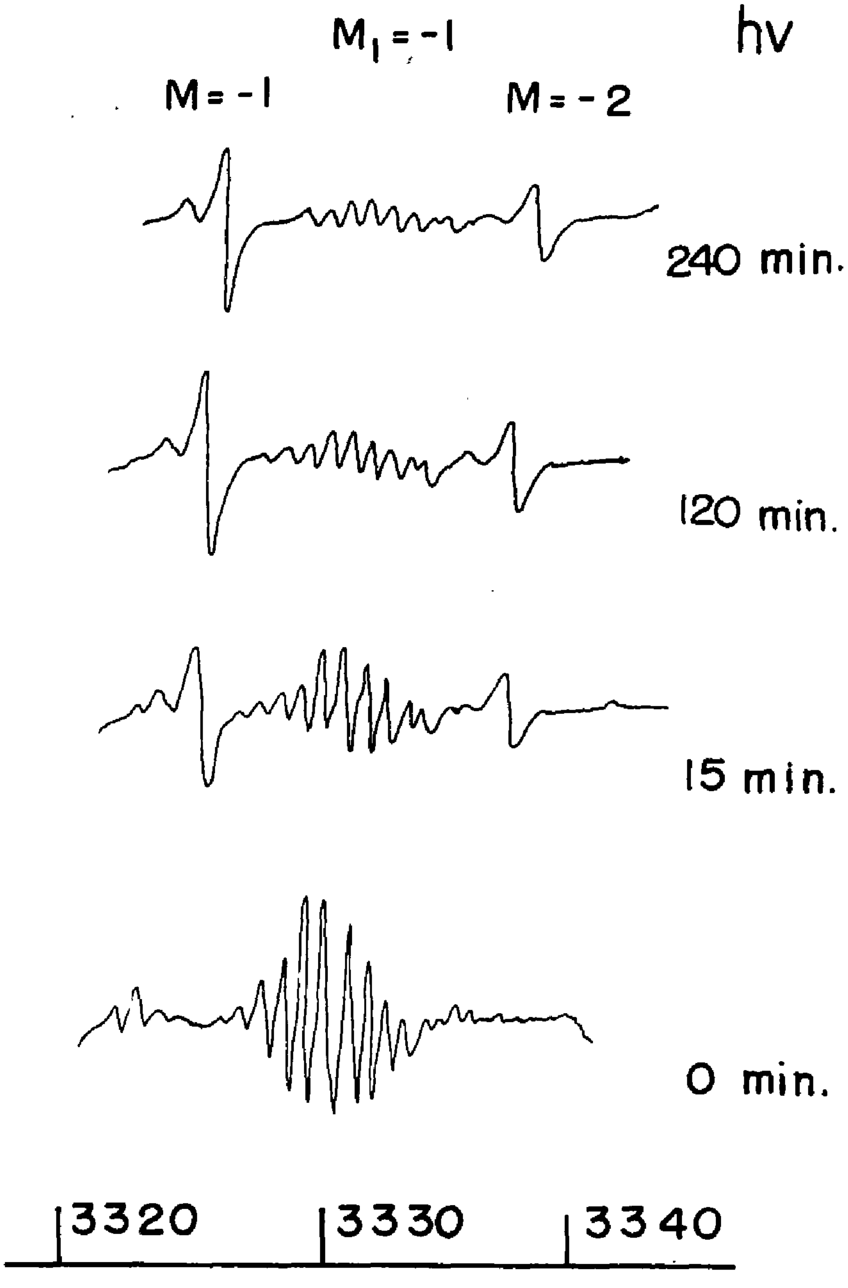

Figure IV.3 ESR spectrum of p-$^6Li_3$ in Argon at 28.5°K. Roman numerals designate matrix sites. M is the nuclear spin projection for three magnetically equivalent ^6Li nuclei. Also shown are atomis Lithium, $^6Li_7$, and an unidentified radical designated ^6LiX.

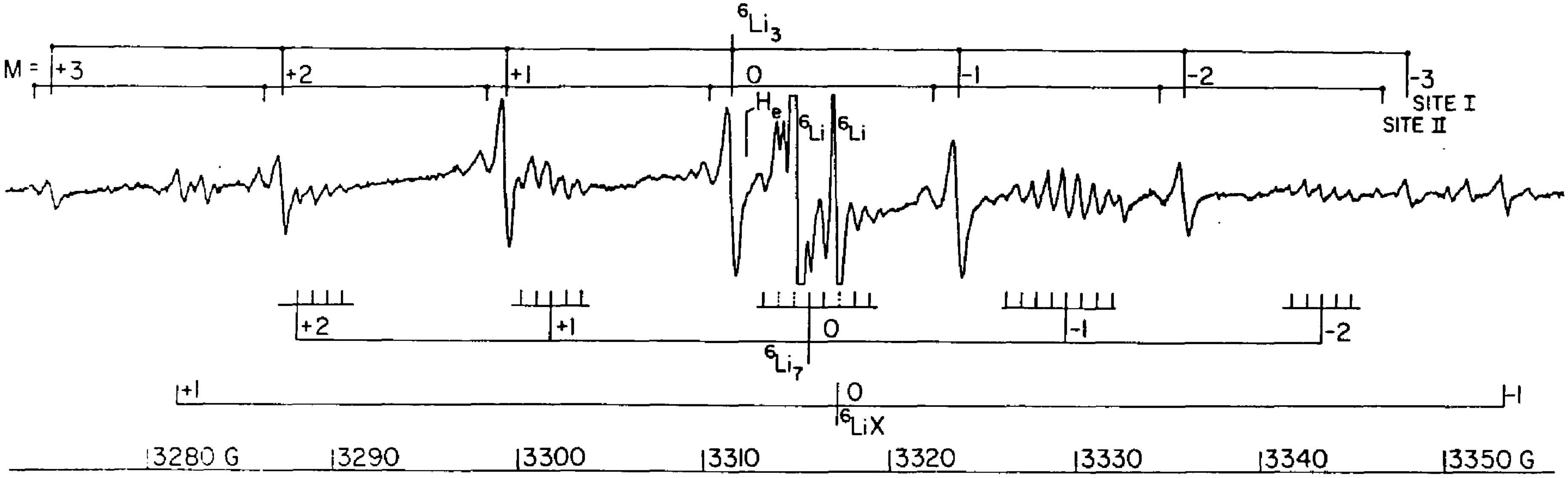

Figure IV.4 Comparison of trimer linewidths for the M=0 and M=+1 components of $^{6}Li_3$ as a function of temperature.

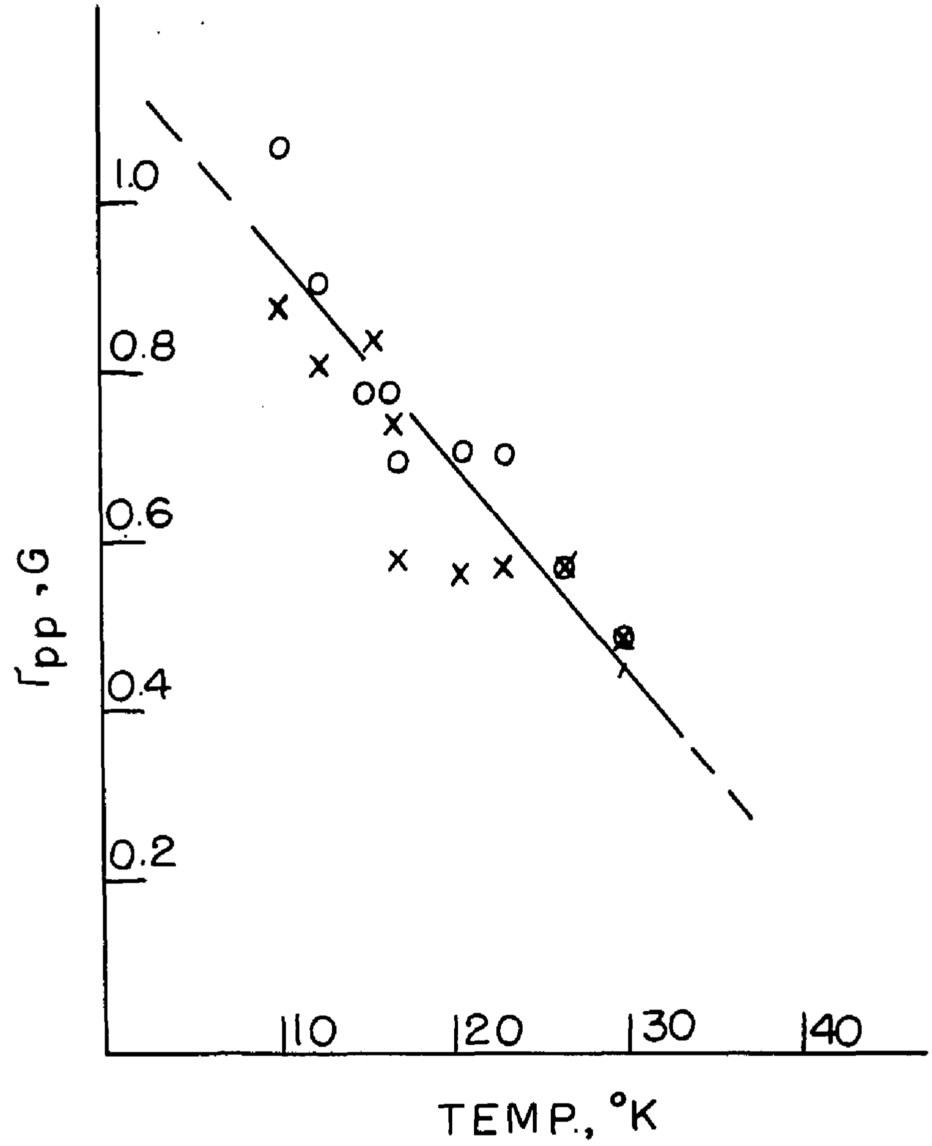

Figure IV.5 Comparison of the trimer intensity (height, in arbitrary units) of the M=0 and M=+1 components of $^6Li_3$ as a function of temperature.

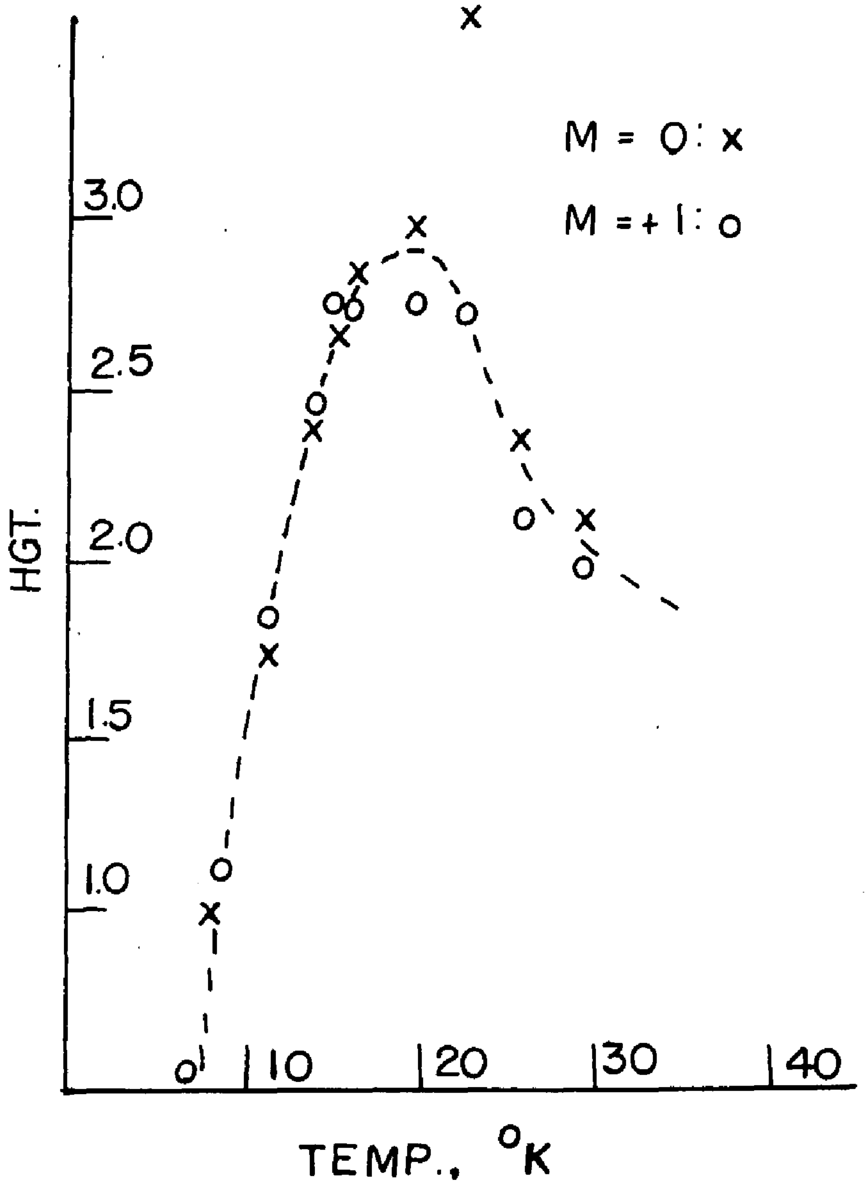

Unlike the cases reported for Na_3 (23,24) and K_3 (26,27), no evidence of a static Lithium trimer was observed despite a careful search over a 3.2 - 32°K temperature range. However, in one run using ^7Li, several transitions that might have been associated with s-$^7Li_3$ were observed. The signals formed a septet of quartets expected for a hf pattern arising from two magnetically eqivalent nuclei and a shf pattern due to a single nonequivalent nucleus. The pattern agreed with the $^2B_2$ ground state of the static Sodium and Potassium trimers. The spectrum, tentatively assigned to s-$^7Li_3$ was obscurred by overlap with other signals from other carriers. Its intensity decreased as the sample was annealed and disappeared entirely at ~14°K. The change in intensity was not reversible and the transitions were not observed again. Also in contrast to Na_3 and K_3, there was no evidences of p-Li_3 developing as the static signal decayed. The s-Li_3 signal had been observed in an unphotolyzed sample.

Table IV.8 gives a summary of the magnetic parameters of the Lithium trimers.

Table IV.8 Magnetic parameters for the Lithium trimers.

	Site	Temp. °K	g_o	$\bar{a}$,Gauss[a]	$\bar{\rho}$[b]
p-$^6Li_3$	I	4.2	2.0028(2)	12.21(1)	0.225
"	II	"	2.0035(2)	12.21(2)	0.223
"	III	"	2.0040(5)	12.09(3)	0.223
"	I	30.0	2.0028(2)	12.21(1)	0.225
"	II	"	2.0035(0)	12.11(3)	0.223
p-$^7Li_3$	I	4.2	2.0026(2)	32.19(8)	0.225
"	I	30.0	2.0044(4)	32.60(1)	0.227
s-$^7Li_3$		4.2	2.0047(4)	33.0(1)[a]	0.230[b]

(a) $\bar{a} = (1/3)(2a_o + a_3)$; where $a_o = 46.1(2)$G, $a_3 = \pm 6.8(3)$G; value above assumes $a_3<0$.

(b) $\bar{\rho} = (1/3)(2\rho_o + \rho_3)$; where $\rho_o = 0.320$, $\rho_3 = 0.047$.

IV.1.3 Lithium Septemer

A polyatomic Li cluster was initially observed in Argon samples during trimer studies. Modification of the deposition conditions increased the cluster's overall intensity and resolution and permitted the tentative assignment of the spectrum to the septemer. The cluster occured in multiple matrix sites with transition fields that show a small but distinct temperature dependence.

The optimum conditions for forming Li_7 were different from those for trimer production. Lithium was vaporized at ~500-550°K to produce a flux of ~0.3μmol/hr incident on the sapphire plate. This is a three fold increase over the fluxes that gave optimum trimer production. Deposition times were still ~5-7 hours. At high Argon dilution, i.e. Ar:Li ~ 400:1, and at deposition temperatures for the plate of close to 4.2°K, the septemer intensity was weak. In fact, the main spectral feature was atomic Lithium in a single matrix site. By running the modulation coils at ~0.25G peak-to-peak amplitude, the cavity was warmed by Joule heating to ~5.8°K. This "warm" deposition technique (50) resulted in a two fold increase in septemer intensity at the original Ar:Li ratio. The atom signal showed a corresponding four fold decrease in intensity. By decreasing the Ar:Li ratio to ~30:1 a further 2-3 fold increase in septemer intensity was produced. All experiments were run at approximately the same Argon flux of ~950 Torr. Annealing the samples to ~30°K improved the resolution of the signals but didn't change the overall intensities. This is in contrast to the thermally induced changes observed in trimer samples. When those postphotolyzed samples were warmed above ~32°K, the trimer intensity decreased by ~50% (as noted previously). Concurrently, the septemer intensity increased threefold and remained approximately constant as the temperature was further increased to ~38°K where degradation of the matrix became significant.

Figure IV.6 shows the ESR spectrum at 4.2°K of an Argon matrix doped with ^{7}Li and annealed to ~30°K. It consists of seven approximately evenly spaced groups of first derivative transitions centered near g~2. The lineshape and spacing indicate predominantly isotrpic g and $\tilde{A}$ tensors. The absence of any downfield transitions corresponding to a zero-field splitting or to a change in the electron spin projection value, ΔM_S, greater than unity, support assigning a doublet ground state. The hf pattern arises from the interaction of the unpaired electron with two magnetically equivalent I=3/2 nuclei. Each hf transition has superimposed on it at least 16 shf components produced by the electron's much weaker interaction with a second set of at least five equivalent

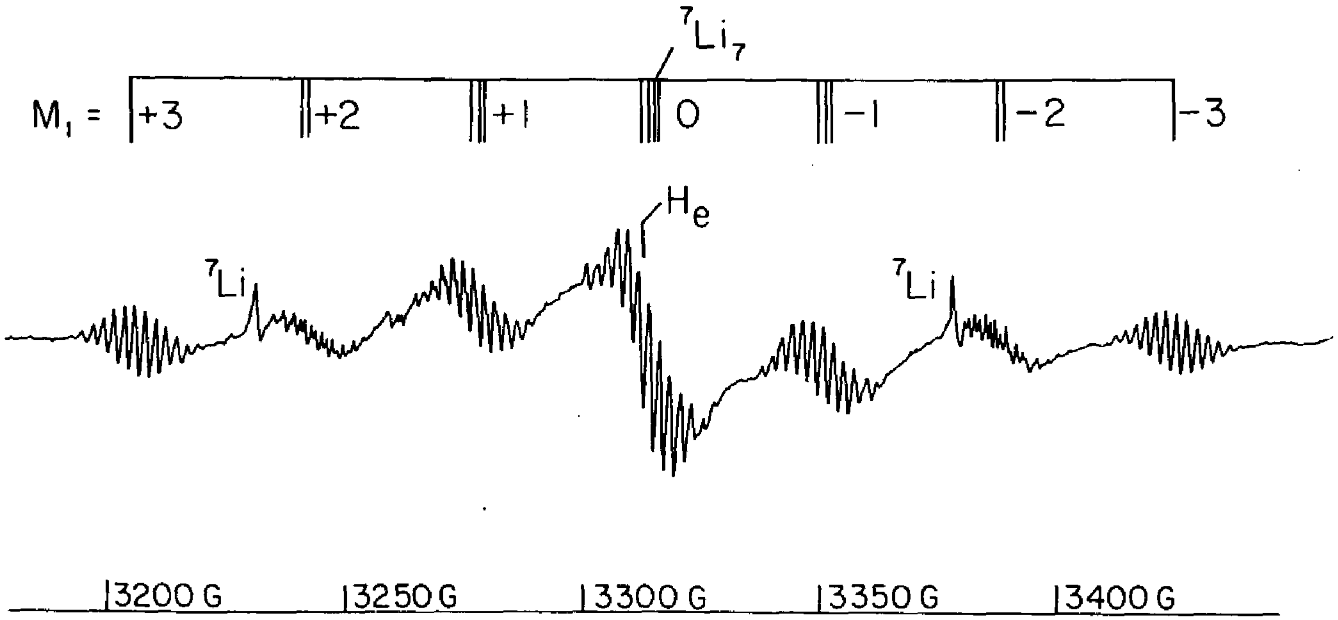

Figure IV.6 ESR spectrum of $^7Li_7$ in Argon at 4.2°K. M_1 is the nuclear spin projection for two equivalent ^7Li atoms. Also shown are the $m=\pm 1/2$ ^7Li transitions. Isotopically enriched ^7Li was used.

$I=3/2$ nuclei. Table IV.9 gives a comparison of the observed transition fields of the hf pattern with their calculated positions. Second order effects have lifted the J degeneracy of each M_1 transition. The last column lists the average shf splitting, $<a_2>$, associated with each (J_1,M_1).

While it is clear that the hf interaction involves only two nuclei, there is some uncertainty as to the number of nuclei responsible for the shf pattern. Figure IV.7 is a high signal-to-noise (S/N) spectrum obtained but signal averaging the $M_1=-3$ hf component for 3 hours. There are clearly at least 16 shf transitions, labelled $M_2 = +15/2$ to $-15/2$. The high resolution detail of the region centered at $M_2=-15/2$ was obtained by signal averaging over a 4 hour period. Because the relative intensities fall off rapidly for large M_2, it is difficult to set an unambiguous upper bound to $|M_2|$ based on the scans obtained. For a cluster larger than the septemer, $M_2=\pm17/2$ components with intensities of about a third those of the $\pm15/2$ signals are expected. In the M_2 region detailed in the figure, the S/N ratio is ~3:1, therefore, if the $-17/2$ transition were present its intensity would be comparable to the noise and it would not be readily discernable. Instabilities in the magnetic field scan circuitry made longer signal averaging periods impractical.

Table IV.9 Comparison of the experimental and calculated transition fields, $H(J_1,M_1)$ for $^7Li_7$ (Site I) in Argon at 4.2°K. Experimental $\langle a_2 \rangle$ are average shf constants for individual (J_1,M_1). Units are in Gauss.

M_1	J_1	Experimental	Calculated	Difference	$\langle a_2 \rangle$ ±≤0.01
+3	3	3205.4	3205.6	-0.2	2.19
+2	2	3242.3	3242.2	+0.1	2.19
	3	3241.1	3241.0	+0.1	2.19
+1	1	3279.0	3278.8	+0.2	2.18
	2	3278.1	3278.0	+0.1	2.19
	3	3276.9	3276.8	+0.1	2.18
0	0	3315.4	3315.4	0.0	2.22
	1	3315.2	3315.0	+0.2	2.22
	2	3314.2	3314.1	+0.1	2.20
	3	3313.0	3313.0	0.0	2.22
-1	1	3351.9	3351.6	+0.3	2.18
	2	3350.9	3350.8	+0.1	2.18
	3	3349.7	3349.6	+0.1	2.18
-2	2	3387.9	3387.8	+0.1	2.18
	3	3386.8	3386.6	+0.2	2.18
-3	3	3423.6	3324.0	-0.4	2.16

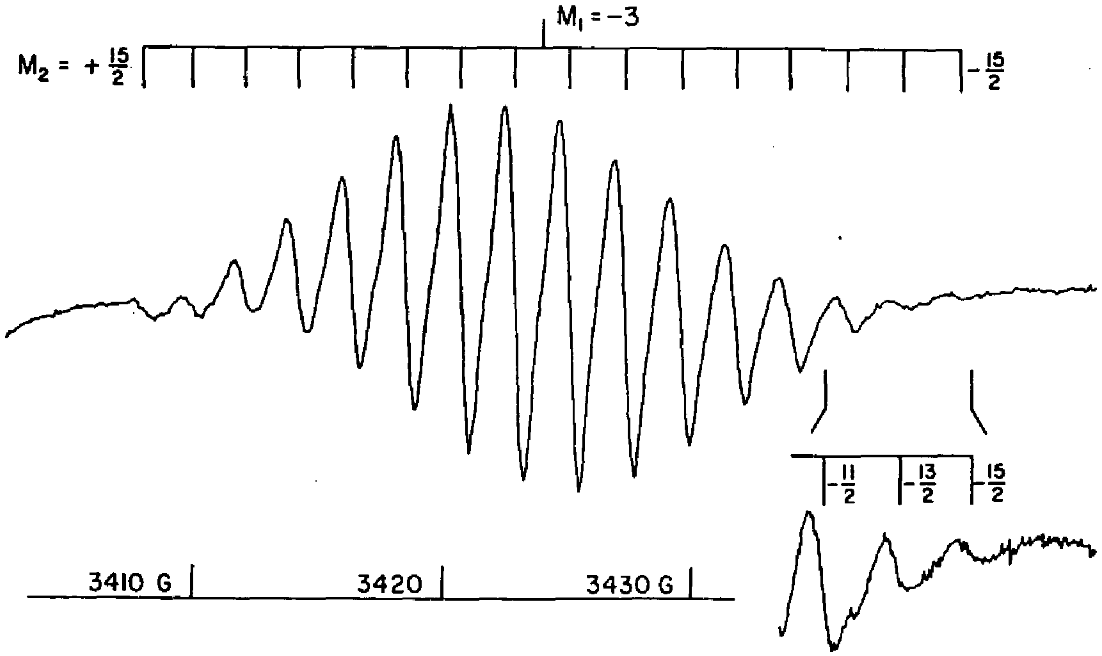

Figure IV.7 High S/N spectrum of the $M_1 = -3$ transition of $^7Li_7$ in Argon at 4.2°K. The overall spectrum and the high field detail were obtained by signal averaging for 3 and 4 hrs respectively. Isotopically enriched ^7Li was used to prepare the sample.

The corresponding spectrum for $^6Li_7$ consists of a quintet of hf transition groups arising from the set of two equivalent I=1 nuclei and labelled M_1=+2 to -2. Each hf transition has at least 11 shf components produced by the second set of at least five equivalent I=1 nuclei and labelled M_2= +5 to -5. As in the case of $^7Li_7$, the $^6Li_7$ spectra also do not completely rule out a cluster larger than the septemer as the carrier. $^6Li_7$ spectra were less well resolved and more obscured by overlap with other carriers' signals than were the $^7Li_7$ spectra. For this reason relative intensity measurements of the shf components were less reliable than for $^7Li_7$. Table IV.10 compares the observed and calculated hf positions of $^6Li_7$. The splittings between transition of the same M_1 but different J_1 was not resolved (except for (2,0)) because of the small value of a_1. This is reflected in the small differences between observed values and the calculated values where the the second order lifting of the J degeneracies were included. The last column gives the average shf splitting $<a_2>$, associated with each M_1 group. The shf line widths for both isotopes were the same, ~300-400 mG. These widths are considered remarkably narrow for polycrystalline samples (45).

Table IV.11 lists the best fit parameters for the isotopic septemers. While the sign of a splitting constant cannot be determined by ESR, the values of a_1 are

Table IV.10 Comparison of the experimental and calculated transition fields, $H(J_1,M_1)$, for $^6Li_7$ (Site I) in Argon at 4.2°K. Experimental $<a_2>$ are average shf constants for individual (J_1,M_1). Units are in Gauss.

M_1	J_1	Experimental	Calculated	Difference	$<a_2>$ ±≤0.01
+2	2	3288.1	3288.0	+0.1	0.82
+1	1	3301.9	3301.9	0.0	0.82
	2	3301.9	3301.8	+0.1	
0	0	3315.8	3315.8	0.0	0.83
	1	3315.8	3315.8	0.0	
	2	3315.8	3315.6	+0.2	
-1	1	3329.6	3329.6	0.0	0.83
	2	3329.6	3329.5	+0.1	
-2	2	3343.3	3343.2	+0.1	0.80

Table IV.11 Magnetic parameters for the Lithium septemers.

	g_o	a_1	$\pm a_2$	ρ_1(a)	$\pm\rho_2$(a)
$^6Li_7$	2.00011(1)	13.78(3)	0.83(1)	0.254	0.015
$^7Li_7$	2.00045(6)	36.39(5)	2.19(2)	0.254	0.015

(a) Isotropic spin populations ρ_1 and ρ_2 are ratios of a_1 and a_2 to hf constants of the free atom a(^{6}Li)=54.29G and ^{a}(7Li)=143.36G.

assumed to be positive because of their magnitudes. The sign of the smaller a_2 constant, however, is not known. The shf value is 6% that of the hf constant and probably arises from spin polarization effects. The ratios of the hf and shf constants, $^{7}a_1/^{7}a_1 = 2.641(3)$, and $^{7}a_2/^{6}a_2 = 2.639(15)$ respectively, are in excellent agreement with the ratio of the nuclear g factors $^{7}g/^{6}g = 2.641$. There is a small discrepancy of $\sim$0.7G between the g values of the two septemers in their major site. It probably arises from calibration uncertainties. The last two columns give the isotropic spin populations deduced from the splitting constants.

Since the actual number of shf interaction could not be conclusively deduced from the spectra, an alternative technique of comparing the observed intensity distribution among the shf components to the predicted ratios for several clusters was attempted. The results discussed here are for the $^{7}Li_7$ studies. Results for $^{6}Li_7$ were not useful because of the poor resolution already mentioned. This was further complicated by the fact that the a_2 value is comparable in magnitude to the shf linewidths. For the ^{7}Li isotope, the five nuclei responsible for the shf structure in Li_7 have a predicted intensity distribution of 1:5:15:35:65:101:135:155: etc. The seven nuclei of Li_9 give 22 shf transitions in the ratio of 1:7:28:84:202:413:728:1128:1554:1918:2128: etc. Table

Table IV.12 Comparison of calculated intensities of $^7Li_7$ and $^7Li_9$ to the observed intensities of the $M_1=\pm3$(a) shf components at 31.1°K.

	Intensities			
	Observed(b)		Calculated	
$\lvert M_2 \rvert$	$M_1=+3$	$M_1=-3$	Li_7(c)	Li_9(d)
15/2	2(2)	3(2)	1	6
13/2	5(2)	6(2)	5	15
11/2	15(2)	18(4)	15	30
9/2	26(5)	43(5)	35	53
7/2	59(20)	73(7)	65	82
5/2	82(7)	109(3)	101	113
3/2	116(6)	138(7)	135	140
1/2	157(2)	155(1)	155	155

(a) Values taken from signal averaged scans: ±25G centered at $M_1=+3$ or -3, 300 scans at 50 sec/scan.

(b) Average $\pm M_2$.

(c) Scaling factor: x33.19.

(d) Scaling factor: x0.073.

IV.12 presents a comparison of these intensities with the observed values for the M_1=±3 hf transitions. These were selected because they have only a single J level and were not overlapped by any other signals. The values were scaled so that the M_2=±1/2 components of each had the predicted septemer intensity of 155. The results were not conclusive but tended towards the septemer values. Comparisons of other M_1 groups were less rewarding. The observed intensity ratios of the shf transitions vary with (J_1,M_1) and usually are not quite symmetrical about the origin. A contributing factor to this distortion is the partial overlap of J levels for a given M_1. A second factor is the partial, and apparently, temperature dependent overlap of spectra for the cluster in different matrix sites. Comparison of the M_1=±3 intensities with the expected values of Li_{11} clearly ruled it out as the carrier.

The septemer of both isotopes were isolated in multiple matrix sites. At least four sites were observed for $^7Li_7$ samples. Of the two most prominant, Site II had ~2/3 the intensity of Site I. The others were considerably weaker and difficult to follow as the temperatire was varied. The sites for $^6Li_7$ were poorly resolved and their temperature dependence too small to analyze accurately.

Figure IV.8 ESR spectra comparing the $M_1=+3$ transition of $^7Li_7$ in Argon at (a)31.2°K and (b)4.2°K. Roman numerals denote principal matrix sites.

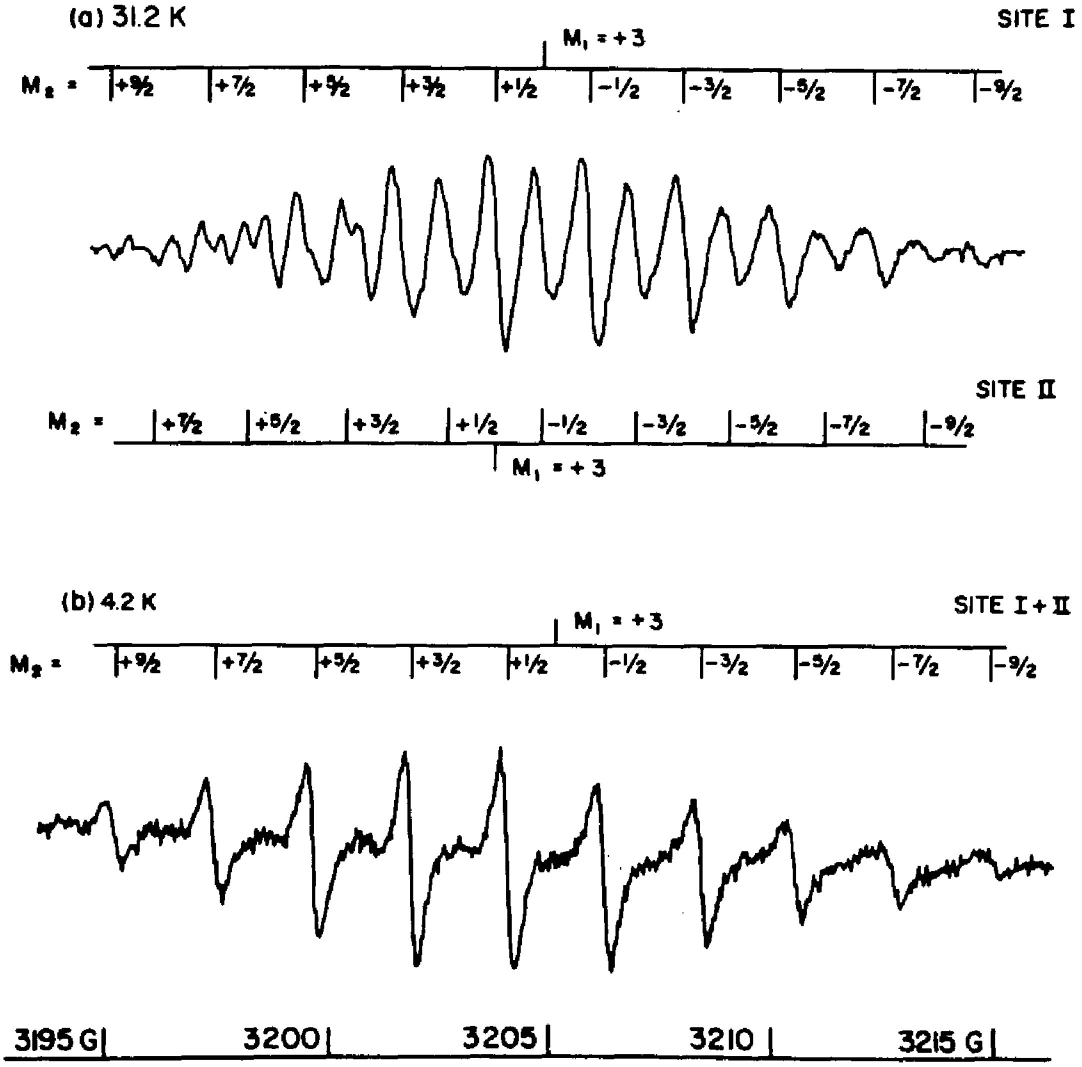

Figure IV.8 shows the spectrum for the $M_1=+3$ component of $^7Li_7$ at 4.2°K and 31.2°K with the two sites as labelled. At the higher temperature the two sites are well resolved, but at 4.2°K they almost completely overlap. The temperature dependent field position can be expressed as

$$H_i(M_1,T) = H_{o\,i}(T) - a_{1\,i}(T)M_1 \qquad [4.7]$$

where $H_o(T) = g_eH_e/g_o(T)$, the transition field origin, and a(T), the hf constant are both functions of temperature, and i indicates the site label. Changes in the relative line positions for the origins of the two sites are given by

$$\Delta H_o = H_I(M_I,T) - H_{II}(M_1,T) \qquad [4.8]$$

Although the "absolute" field position of each site changed by less than 0.02G/°K, the relative values were quite well determined (because calibration errors tend to cancel). Figure IV.9 shows the measured temperature dependence of the relative origins (H_I-H_{II}) of the $M_1=\pm3$ transitions. The graph suggests that H_I-H_{II} varies linearly over the range $10\leq T\leq 35$°K, although it does not preclude higher order interactions.

Figure IV.9 Temperature dependence of the relative origins (H_I-H_{II}) of M_I=±3 transitions for matrix sites I and II of $^7Li_7$ in Argon.

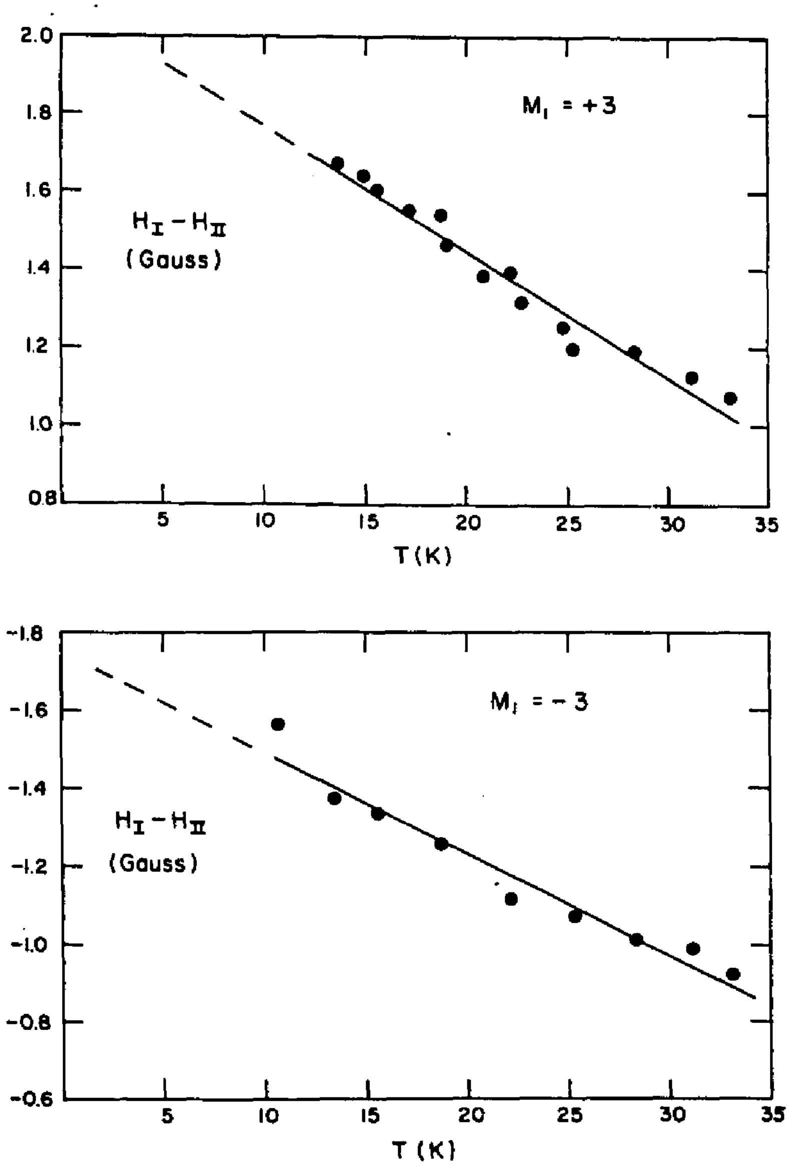

All the M_I transitions showed similar behavior, although the actual analyses were less complete and reliable due to spectral congestion. Experimental values for $M_I = \pm 3$ were used to estimate $\Delta H_o(T)$ and $\Delta a_1(T)$ for each site from the relationships

$$\Delta H_o(T) = 1/2(\Delta H(+3) + \Delta H(-3))$$

$$\Delta a_1(T) = 1/6(\Delta H(+3) + \Delta H(-3)) \qquad [4.9]$$

These values were then used to predict the line shifts for the $M_I = \pm 2$ components. Resolution of these transitions was poor because of significant overlap of the J levels for the two sites. Table IV.13 lists the values of $a_1(T)$, $H_o(T)$ and $g_o(T)$ for the two sites at 4.2 and 31.2°K. Over this temperature range $a_1(T)$ for Site II remained constant (within experimental error), while the value for Site I changed by $\Delta a/a \sim 1/2\%$. These trends can be attributed to a small temperature dependence in the a_1 hf constants and the g values for the two sites. Any temperature dependency in a_2 was too small to observe.

Values for H_o (Eq.[4.8]) were fit to a quadratic and to a linear least squares equation in T and gave the following:

Quadtratic:

$$\Delta H_o = 0.19 - 3.5\times10^{-3}T - 1.3\times10^{-5}T^2$$

Table IV.13 Comparison of the temperature dependence of the magnetic parameters for $^7Li_7$ Sites I and II at 4.2 and 31.2°K.

	a_1		H_o		g_o (a)	
Temp.,°K	Site I	Site II	Site I	Site II	Site I	Site II
31.2	36.59(3)	36.95(5)	3315.26(5)	3315.12(10)	2.00047(3)	2.00056
4.2	36.39(5)	36.99(5)	3315.39(9)	3315.23(9)	2.00039(6)	2.00049
31.2-4.2	+0.20(6)	-0.04(7)	-0.13(10)	-0.11(13)	$+8(7)\times10^{-5}$	+7(8)x1

(a) g_o assumes $H_e = 3312.20$ G.

$$\Delta a = -0.77 + 2.17\times10^{-2}T - 2.7\times10^{-4}T^2$$

Linear:

$$\Delta H_o = 0.172 - 3.2\times10^{-3}T$$

$$\Delta a = 0.640 + 9.7\times10^{-3}T$$

All values are in Gauss.

The best fit to the data was provided by the linear equation. Although these results were based on the observed $M_1=\pm3$ transitions, they predicted quite well the observed temperature behavior of H_I-H_{II} for $M_1=\pm2$.

IV.2 Interpretation

IV.2.1 Lithium Atom

Multiple trapping site are common in matrix isolation and well documented for the alkali atoms (54,55), although the exact nature of the sites is generally not known. The rare gases form face centered cubic (fcc) solids providing three possible types of trapping sites. These are substitutional, octahedral and tetrahedral, where the guest atom or molecule is surrounded, respectively, by 12, 6, and 4 nearest neighbor matrix atoms (56). In Argon, a metastable hexagonal closest packing (hcp) lattice can coexist with the fcc form even at low temperatures (9). Surface and microcrystal interfaces are also potential trapping sites. The variability of their occurrence may explain the weaker variable preanneal and nonreproducible postanneal sites. They are ignored here because of the reproducibility of the reported parameters and the general narrowness of the atom signals (which is not expected for the unsymmetric fields of surface sites). The sites associated with fcc and hcp lattices are idealized pictures. The actual packing around a guest atom depends on its size relative to that of the matrix atoms. Assuming that all atoms involved are uncharged and spherically symmetric, only two interactions are important:

(i) van der Waals force: The attraction between the guest and matrix atoms produces a small expansion of both charge clouds and decreases the guest atoms hfs constant. This effect is generally associated with sites that are large relative to the guest's volume.

(ii) Pauli exclusion force: Here the electron cloud of the guest penetrates the closed shell of the matrix atoms. This produces an effect opposite to (i), and increases the guest's hfs value. It is associated with sites that are cramped relative to the guest's volume. In addition, the overlap mixes matrix atom properties into the guest atom wave function by transferring a small amount of the charge density from the unpaired electron onto the matrix atoms. The spin orbit interaction with the matrix produces negative shifts in the g values of the guest regardless of the nature of the site (57).

Because these two competing interactions are associated with different sites, it is sometimes possible to assign the probably type of site occupied based on the difference, Δa, between the observed hf constant and the gas phase value. The Li atom site parameters most frequently referred to are the values of Jen et al (54,55). In Argon, Li was isolated in two major sites with the following parameters:

	Site I	Site II
a, Gauss	141.07	147.80
ρ	0.98	1.03
(Δa/a)x100%	-0.6	+3.1
Δgx(-100)	0.05	0.13

where $\Delta a/a = ((a-a^*)/a)\times 100\%$ and $\Delta g = g-g^*$, where the * denotes the gas phase atomic value.

The values reported in section IV.1.1 agree with the Jen values for Site II, but there was no evidence of a site corresponding to Jen Site I. This is not unexpected since calculations on the overlap values of the alkali atoms indicate they are all too large to fit in substitutional sites in Argon (58). Site I may occur in the Jen matrices because of the techniques used to generate the atoms and anneal the samples. As expected, the g shifts are negative. Indeed, calculations predict that this shift is always negative for Li atoms in Argon or Krypton matrices (59).

IV.2.2 Lithium Trimer

Lithium trimer spectra are consistent with a molecule that has three magnetically equivalent nuclei. The absence of any additional finer structure within the seven transitions of $^{6}Li_3$ or the ten of $^{7}Li_3$ implies that no other magnetic nuclei are present. The observed hf constants indicate that the unpaired electron spin in the trimer has been significantly redistributed from that of the probable precursors: 3 non-interacting atoms or a dimer + an atom. Thus, Li_3 is chemically bound and not a van der Waals adduct. Describing the actual distribution of the spin on the individual nuclei presents a bit of a challenge.

Figure IV.10 shows a simple Huckel molecular orbital scheme for a timer along with a Walsh type correlation diagram for the bending coordinates. It is analogous to the bonding scheme in the allyl radical but with the Carbon 2p basis functions replaced by the valance s-orbitals of the alkali atoms. The symmetry of the ground state depends on the value of the central angle. If it is "obtuse" or "acute" relative to 60°, the molecule will have C_{2v} symmetry and a $^2B_2$ or $^2A_1$ ground state, respectively. For the $^2B_2$ state the unpaired electron density is divided between the two terminal nuclei to produce the hf interaction. The central nucleus lies in a nodal plane. In the alkali trimers this atom is only approximately nodal. There is some spin density induced there by spin polarization effects. This will produce a weak shf interaction. For the $^2A_1$ state the hf splitting comes from ~50% of the electron density concentrated on the central atom. The terminal atoms each carry ~25% of the density and will produce a relatively large shf interaction. Difficulty arises at an apical angle of 60° where the b_2 and a_1 energy levels become degenerate. The molecule now has the D_{3h} symmetry implied by the Li_3 spectra, but it's doubly degenerate $^2E'$ ground state should cause it to undergo a Jahn-Teller distortion (60-62) down to one of the C_{2v} structures.

The basic theory of the dynamic Jahn-Teller effect applies the Born-Oppenheimer approximation to systems where two electronsic states, represented by the orthonormal wave functions ψ_{e_1} and ψ_{e_2} are strongly coupled through the nuclear kinetic energy terms of the full Hamiltonian. To a first approximation, the overall wave function can be represented by

$$\psi(q,Q) - \psi_{e\,1}(q,Q)\psi_{n\,1}(Q) + \psi_{e\,2}(q,Q)\psi_{n\,2}(Q)$$

where q and Q are the electronic and nuclear coordinates, respectively, and ψ_n is the nuclear wave function. $\psi(q,Q)$ represents the total vibronic coupled wave function. The 3N-6 vibrational modes of the trimer can be represented by the three normal coordinates Q_a,Q_x and Q_y. Under D_{3h} symmetry the two electronic wave functions are degenerate. This degeneracy is unaltered by the totally symmetric vibration, Q_a, and it can be considered as separate, uncoupled from the remaining vibrational and electronic motions of the molecule. The degenerate coordinates, Q_x and Q_y form a basis for the e' representation in the D_{3h} point group. Because of the vibronic coupling, the electronic degeneracy is lifted by the vibrational distortion along these coordinates. Vibronic coupling produces the dynamic Jahn-Teller effect.

The normal coordinates can be used to describe the geometry of a timer with D_{3h} symmetry most readily by rewriting them in polar coordinate for (63).

$$\rho - (Q_x^2 + Q_y^2)^{1/2}$$

$$\Phi - \cos^{-1}(Q_x/(Q_x^2 + Q_y^2))$$

Holding ρ fixed at any arbitrary value and varying Φ by $(2/3)\pi$ or $(4/3)\pi$ produces symmetrically equivalent molecules. Therefore, the potential energy surface for the two electronic wave functions has a three fold degeneracy with respect to rotation about an axis perpendicular to the molecular plane. The addition of other symmetry operations such as the replacements:

$$\Phi\rightarrow(2/3)\pi-\Phi,\quad \Phi\rightarrow(4/3)\pi-\Phi,\quad \Phi\rightarrow-\Phi$$

generates a group isomorphic with C_{2v}. Figure IV.11 represents the symmetry as a function of Φ. Figure IV.12 is a schematic of the trimer potential energy surface. Each circle represents an energy contour. In the center is a high energy peak corresponding to the D_{3h} geometry. It is surrounded by a trough in which there are three wells separated by three saddle points and enclosed by a high energy wall. The general appearance is that of a "Mexican" hat. Starting with the equilateral triangular geometry, distortions down to the lower C_{2v} symmetry can occur by "opening up" any one of the three internuclear bonds. This leads to three equivalent energy wells that differ from each other only in the original arbitrary labelling of the three nuclei. If the barrier between the wells is high enough, the trimer will be "frozen" out with ~1/3 of the population isolated in each well, and the

Figure IV.10 Simple Huckel type molecular orbital scheme for alkali trimer molecules.

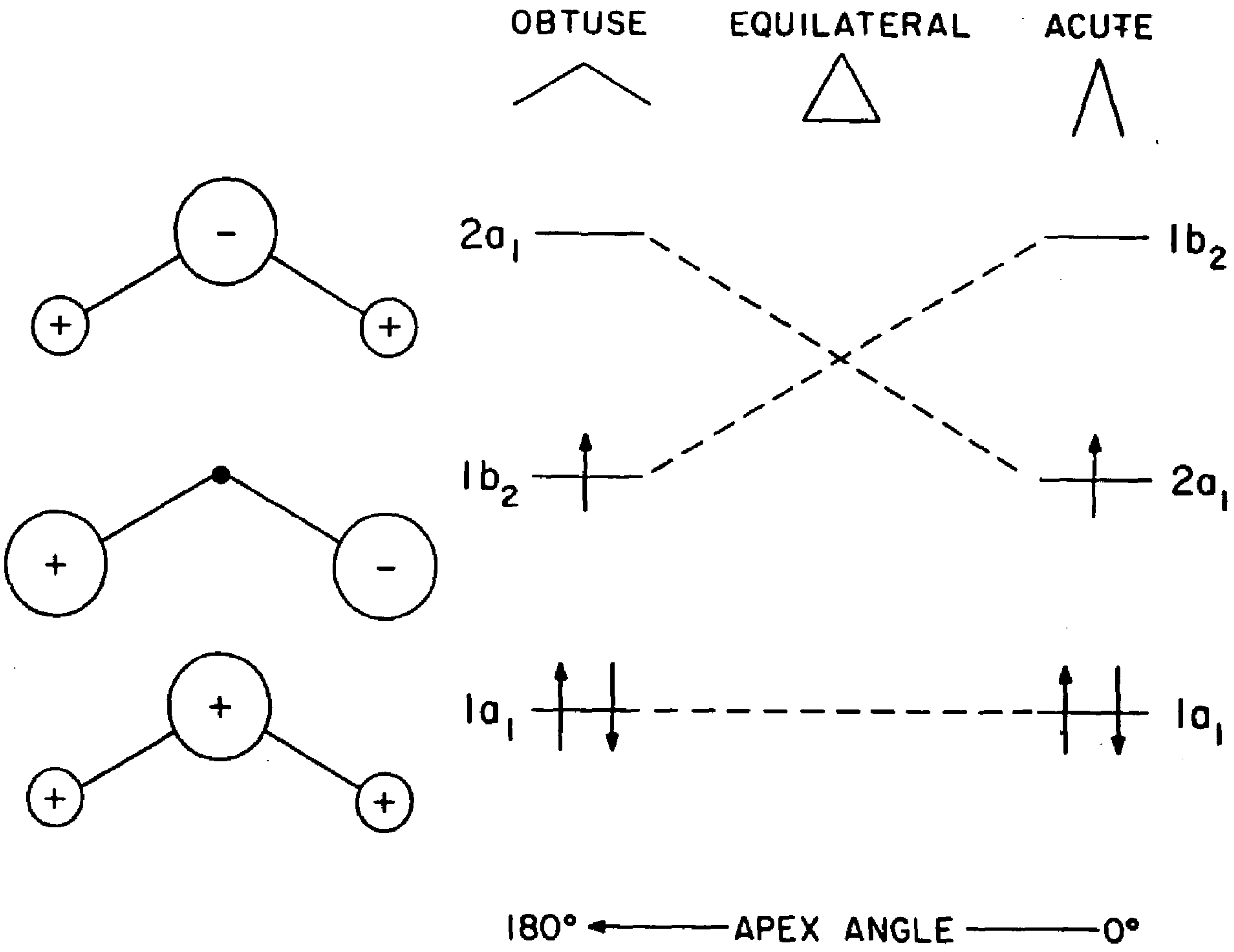

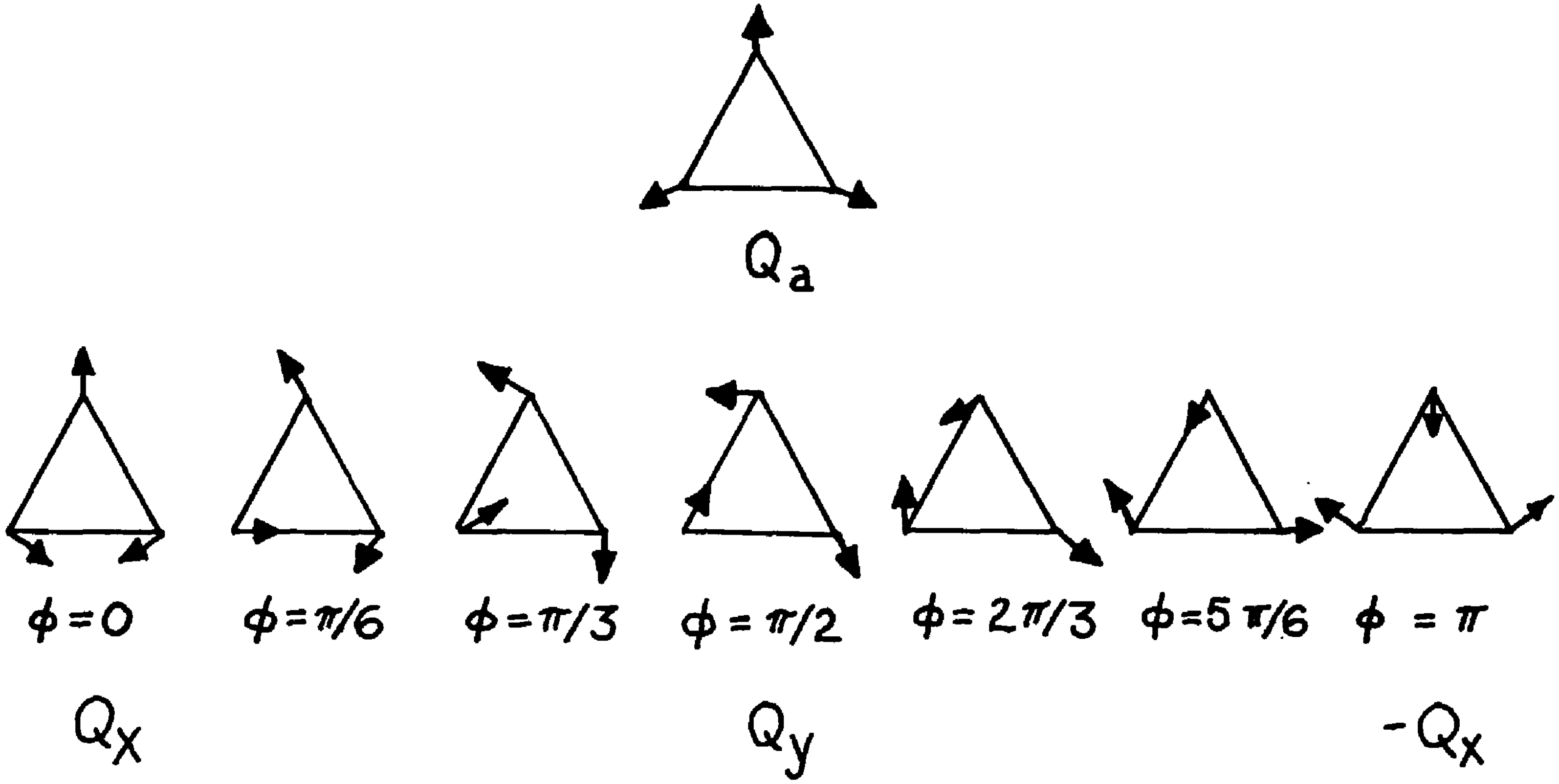

Figure IV.11 Representation of the vibrational motions in D_{3h} symmetry.

Figure IV.12 Trimer potential energy surface. (a) gives the normal coordinate and real space description of pseudorotating Li_3 with circles representing energy contours. (b) gives the surface initially calculated by Gerber and Schumacher (Ref.32).

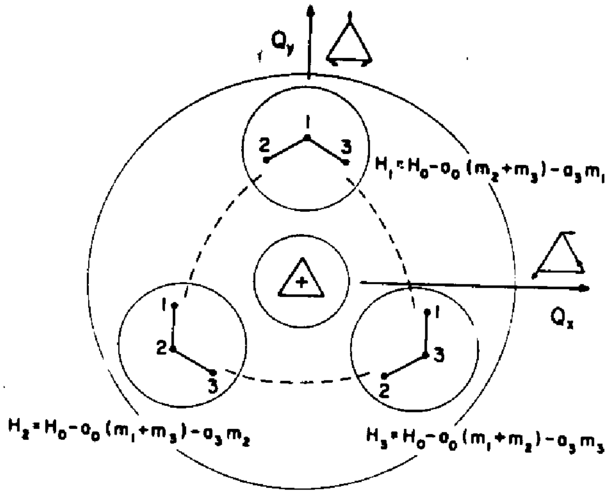
Qy
1
2
3
H₁ = H₀ − a₀ (m₂ + m₃) − a₃ m₁
+
Qx
1
2
3
1
3
2
H₂ = H₀ − a₀ (m₁ + m₃) − a₃ m₂
H₃ = H₀ − a₀ (m₁ + m₂) − a₃ m₃

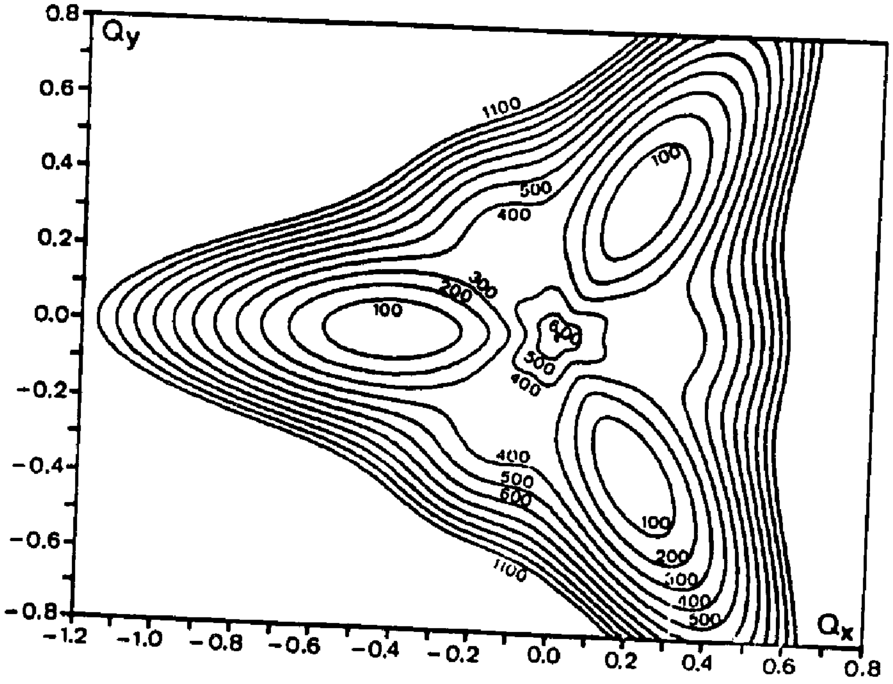
Qy
Qx
0.8
0.6
0.4
0.2
0.0
−0.2
−0.4
−0.6
−0.8
−1.2
−1.0
−0.8
−0.6
−0.4
−0.2
0.0
0.2
0.4
0.6
0.8
1100
500
400
100
300
200
100
600
500
400
400
500
600
1100
100
200
300
400
500

static trimer spectrum will be observed. If, however, the trimer can hop over or tunnel through the barrier or if the lowest vibronic level lies above the saddle point energy, then the molecule is free to move among the three wells spending ~1/3 of its time in each. This results in an averaged value of the three orientations. Therefore, the three nuclei appear to be equivalent without the molecule having to assume the electronically unstable D_{3h} geometry.

For the trimers of Na (23,24) and K (25,26), both static and *pseudorotating* spectra were observed, depending on the temperature of the Argon matrix. This indicates that their ground vibronic state is bound within the wells. For Li_3 even at temperatures slightly below 4.2°K only the *pseudorotating* trimer was observed, suggesting that the molecule is completely fluxional. This confirms the most recent *ab initio* calculations on Li_3 which predict the Li_3 surface to be fairly flat. Gerber and Schumacher (32) were the first to produce the adiabatic Born-Oppenheimer energy hypersurface of Li_3 as a function of the normal coordinates in a realistic nonharmonic approximation. Their method used the coupled electron pair approximation (CEPA) to calculate the adiabatic potential and then applied the B-O approximation for degenerate electronic states to the coupled vibronic states. The calculation predicted Li_3 to be bound by

~3000 cm^{-1} relative to the $Li_3 \rightarrow Li_2 + Li$ dissociation and with the D_{3h} intersection and the saddle points at 350 and 250 cm^{-1} respectively above the well minima. A recalculation using improved wave functions (63) later predicted the saddle points to be absent. Both calculations predicted that Li_3 was free to *pseudorotate*. *Ab initio* calculations on Na_3 (33) gave similar results although the dynamical behavior was expected to be less pronounced since the surface was predicted to have distinct though shallow wells.

The Li trimer is a common molecule for computational studies because of its simple electronic configuration (51,64-67). Table IV.14 summarizes the isotroic spin populations predicted by several sophisticated computational methods and compares them with the ESR experimental results. ρ_o gives the isotropic spin population on each terminal atom, ρ_3 that on the central nucleus and $3\bar{\rho}$ represents the sum, where

$$\bar{\rho} = (1/3)(2\rho_o + \rho_3)$$

While the spin distribution of $^2A_1$ and $^2B_2$ are very different, they both average to approximately the same total isotropic spin population value. A similar total was calculated for the linear geometry with $^2\Sigma_u$ ground state not listed in the table (30). For this reason,

Table IV.14 Comparison of the experimentally estimated isotropic spin populations of the Lithium trimer M_o-M_3-M_o with several calculated values.

Method	$^2A_1$			$2B_2$		
	ρ_o	ρ_3	$3\bar{\rho}$	ρ_o	ρ_3	$3\bar{\rho}$
Li_3(RHF)	0.15	0.13	0.43			
Li_3(CEPA)	0.19	0.22	0.60	0.35	0.02	0.72
Li_3(CI)	0.14	0.31	0.59	0.28	0.05	0.61
p-Li_3(ESR)						0.68
s-Li_3(ESR)				0.32	0.05	0.69

RFH: Restricted Hartree-Fock. Ref.29.

CEPA: Coupled Electron-Pair Approximation. Ref.32.

CI: Configuration Interaction. Ref.30.

ESR: Experimental ESR values.

Note: $3\bar{\rho} = (2\rho_o + \rho_3)$.

there was no strong consensus on the ground state geometry. Isolation of s-Na_3 (23) gave the first spectral support for a $^2B_2$ ground state for the alkali trimers. For Li_3 CEPA values of $^2B_2$ give results closest to the experimental values. This ambiguity is understandable in light of the evidence that Li_3 is a fluxional molecule with the $^2B_2$ and $^2A_1$ states of comparable energy. Inadequacies in some methods arose from ignoring the vibrations of the nuclei and/or the nuclear-electronic motional interactions essential to understanding a dynamic Jahn-Teller effect.

The signs of the isotropic hf and shf interactions are not explicitly determined by ESR. The hf values are assumed to be positive because of their magnitude, but the sign of a_3 is in doubt because it arises from spin polarization effects. Since the *pseudorotating* trimer gives an average hf value

$$\bar{a} - 3(2a_o \pm a_3)$$

the sign of a_3, and consequently of ρ_3, can be determined if both the static and *pseudorotating* trimers have been observed. Table IV.15 compares the experimental ρ values for the alkali trimer. The static values agree with the *pseudorotating* average for Na_3 and K_3 if the sign of a_3 (ρ_3) is negative. In contrast, the Li_3 values indicate a_3

Table IV.15 Comparison of the experimentally deduced isotropic spin populations for the alkali timers.

	ρ_1	ρ_3	$\bar{\rho}^{(a)}$	$3\bar{\rho}$
s-Li_3	0.32	0.05	0.23	0.69
p-Li_3			0.23	0.68
s-K_3	0.47	0.06	0.30	0.89
p-K_3			0.30	0.89
s-Na_3	0.47	0.07	0.29	0.87
p-Na_3			0.30	0.88

(a) $\bar{\rho} = (1/3)(2\rho_1 + \rho_3)$

is positive. The last column lists the total isotropic spin population of each species. Li_3 has ~30% p-character in its valence bonding compared to only ~10% for Na_3 and K_3.

IV.2.3 Lithium Septemer

The analysis of the ESR data does not rule out the nanomer as the signal carrier, however, recent theoretical calculations support assignment to the septemer. Simple Huckel calculations were performed on a number of sodium cluster geometries including Na_7, Na_9 and Na_{11} (68). The molecular orbitals (MOs) for the bipyramid geometries agreed well with the observed spectra. The calculations, while clearly not computationally sophisticated, qualitatively paralleled the relative energies predicted by more sophisticated (and more expensive) methods. Several geometries are consistent with the ESR picture of the distribution of the unpaired electron density. Three of the more likely septemer geometries are illustrated in Figure IV.13. The energies, given in arbitrary units, are too close to make any one more likely than the others. Diatomics-in-Molecules (DIM) calculations on clusters up to the heximer suggest several trends(69,70):

(i) There are two competing effects, the bond length increases with increasing coordination number so that individual bonds become weaker, however, the total number

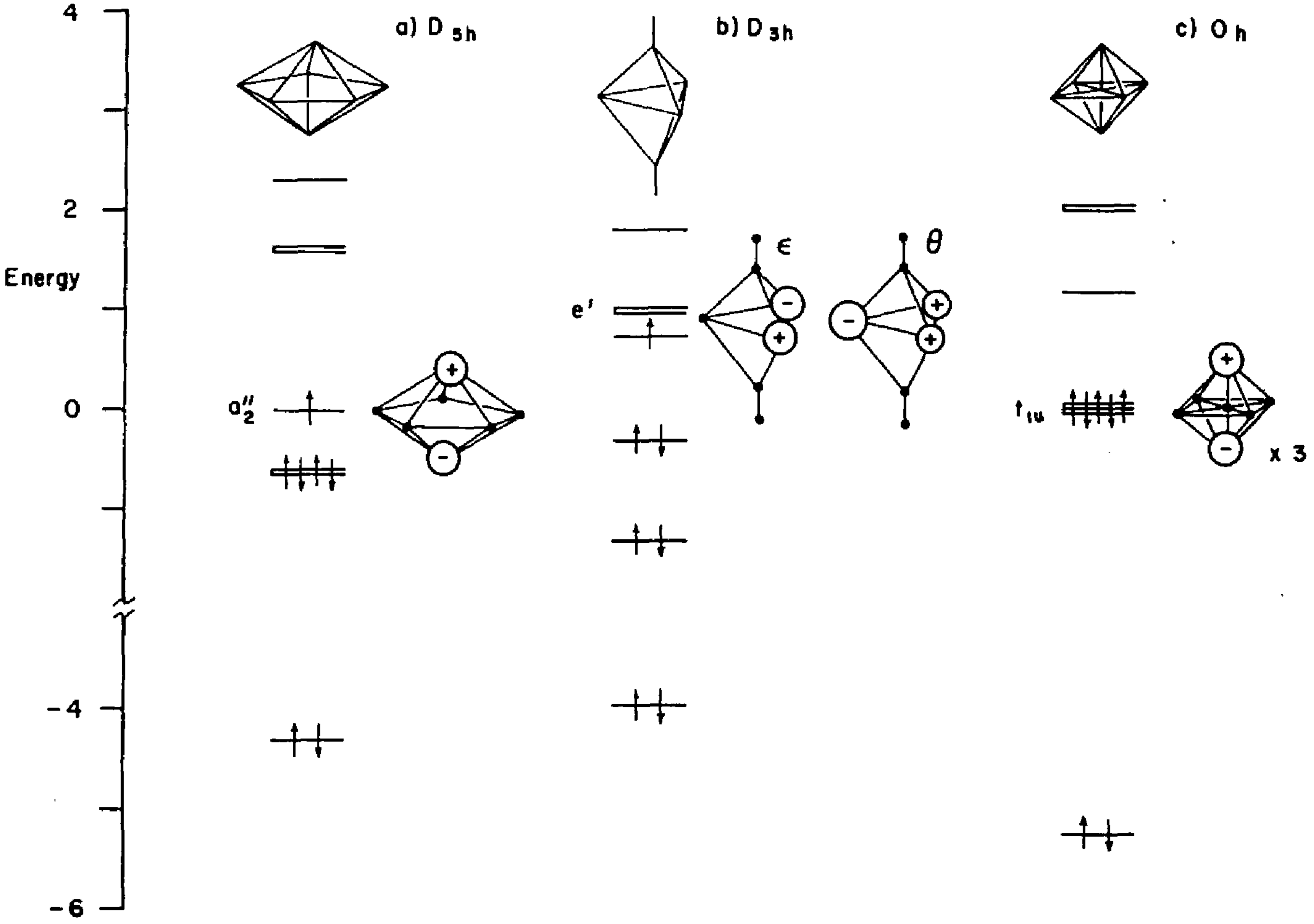

Figure IV.13 Schematic showing relative energies of several septemer geometries. The energies were based on simple Huckel calculations.

of bonds increases so that generally, cluster stability increases with increasing size.

(ii) Compact, highly symmetric structures are energetically favored, and, because of their high symmetry, Jahn-Teller effects are expected to be important.

(iii) There are always at least two most stable compact structures of comparable energy with respect to dissociation to smaller cluster sizes.

(iv) As the number of atoms in the cluster increases, the difference in energy between the two structures decreases.

Ab initio calculations suggest that Jahn-Teller effects and the tendency towards more compact geometries may be crucial factors in determining cluster structures. The square bipyramid, O_h and the D_{3h}, geometries represent three fold and two fold electronically degenerate ground states, respectively, and would be subject to Jahn-Teller distortions.

The pentagonal bipyramid, D_{5h}, however, has the aesthetic appeal of being compact without being electronically degenerate. All degenerate one electron levels in the leading configuration of the CI ground state wave function, $a_1'^1 e_1'^4 a_2''^1$, are fully occupied and there is no Jahn-Teller distortion expected. Also, the ground state has minimal spin multiplicity. In addition, the importance of pentagonal symmetry is well recognized in the nucleation and growth sequence of small clusters and microcrystals (71-73). Despite the cubic structure of most solids, the preferred packing of seven atoms is the pentagonal bipyramid.

Ab initio calculations predict comparable binding energies for the pentagonal bipyramid and a second septemer of C_s symmetry. This second septemer, $Li_7(2.4.1)$ has it 2, 4 and 1 centers in the 1st, 2nd and 3rd planes of the fcc lattice. The binding energies are 14.1 and 14.8 kcal/mol for the C_s and D_{3h} molecules respectively, giving the pentagonal bipyramid a slightly greater stability (74). ESR spectra reported for Li_7 (52), Na_7 (68) and K_7 (25) closely match recent *ab initio* calculations on the pentagonal bipyramid (75). There is complete agreement between theory and experiment on the importance of the participation of p-orbitals with increasing cluster size, the similarity between the alkali clusters in their bonding and especially the high degree of sp-hybridization for the Li clusters.

The temperature dependence of the relative site positions follows the arguments outlined in Section IV.2.1. The symmetry associated with each of the several possible lattice structures (fcc and hcp), the relative positions of nearest neighbors and the symmetry of the vacancies that the metal cluster might occupy are quite different and can reasonably be expected to show different temperature dependencies. For the fcc vacancies studied at temperatures up to 60°K, there is an oscillating displacement field that pushes the nearest neighbors toward the vacancies while the second row of nearest neighbors is displaced away from the vacancies. The net result is a decrease in the volume of the vacancy corresponding to the Pauli exclusion force mentioned elsewhere. Several other mechanisms are often used to describe the temperature dependence of the hf parameter (78-80). As the temperature increases, higher vibrational levels may become populated so that a_1 becomes dependent on the vibrational energy. Vibrational distortions of the ground state symmetry may also promote admixture of higher energy unoccupied orbital components into the ground state wave function. In addition to the interaction of the hf parameter with the intramolecular vibrational mode(s) of the cluster, it can also interact with the matrix. Through the orbital-lattice coupling, the hf term can interact with the phonon continuum of the lattice, although generally, the increase in amplitude of the phonon vibration with increasing temperature produces a decrease in the value of $a_1(T)$. Both the intramolecular and the phonon interactions are explicit functions of temperature. Finally, there is an implicit effect possible through the thermal expansion of the lattice which is expected to increase the value of $a_1(T)$ with increasing temperature. However, because of the scatter in the data points for the shifts in H_I-H_{II} and a_1 it was not possible to show quantitatively which of the several interactions possible were producing the observed shifts for the two sites.

IV.2.4 Comparison of Alkali Clusters

Table IV.16 summarizes the s-character of the bonding in Li, Na and K as a function of cluster size. For the alkali metals, neither experiment nor theory give total isotropic spin populations, ξ, close to unity. This deficit provides a measure of the average degree of hybridization in each cluster. For the atom, ξ_1 is constrained to be unity because the alkali valence electron is in an s-orbital. All cases where the parameter is less than unity are assumed to indicate p-orbital involvement in the bond. ξ_2 is not actually a spin population. It is the average s-character for an electron in the doubly occupied Ů valence bond of the dimer. The values were deduced by Linus Pauling in 1949 (81). ξ_2 = 1-fractional p-character. For the timer, ξ_3 is the sum of the spin populations, $3\rho_3$, for the three nuclei. Similarly, for the septemer, ξ_7 is the sum of the measured spin populations $2\rho_1 + 5\rho_2$, assuming that the polarization effects induce a negative spin population on

Table IV.16 Orbital composition (average s-character) for the "Fermi" electron of alkali atom clusters, M_n.

	ξ_1	ξ_2	ξ_3	ξ_7	ξ_∞
Li	1.00	0.86	0.68	0.45	0.42(2)
Na	1.00	0.93	0.87	0.64	0.66(4)
K	1.00	0.94	0.89	0.63	0.66(4)

the five nuclei responsible for the shf interaction. In the last column, ξ_∞ is the bulk metal parameter (41) given by

$$\xi_\infty = |\psi_F(0)|^2/|\psi_A(0)|^2$$

where $|\psi_F(0)|^2$ is the square of the wave function at the nucleus for an electron on the Fermi surface of the metal, given by

$$|\psi_F(0)|^2 = 1.277\times10^{23}\ \frac{KT_F}{\chi_\rho/\chi_0}\ \mathrm{cm}^{-3}$$

where K is the experimental Knight shift arising from the magnetic field of the electron at the nucleus and T_F is the Fermi temperature (82). χ_ρ/χ_0 is the ratio of the Pauli spin susceptibility of the metal to the paramagnetic susceptibility of the metal to the paramagnetic susceptibility of a Fermi gas of conduction electrons. The assumed ratios were 2.8(1), 1.6(1) and 1.7(1) for ^{7}Li, ^{23}Na and ^{39}K respectively, and represent averages from several tabulated values (83). $|\psi_A(0)|^2$ is the square of the wave function at the nucleus of the free atom.

The ESR values fit very nicely between the independently deduced dimer and bulk metal values. Examination of Table IV.16 suggest several trends:

(i) For each alkali metal, the s-character of the bonding decreases monotonically as the cluster size increases.

(ii) For any given cluster size, the s-character of the Fermi electron in Na_n and K_n are almost identical while,

(iii) The corresponding Li_n values are consistently lower implying a greater proportion of p-character in the bonding. This trend in orbital composition does not follow the order of ns → sp promotion energies of 1.85, 2.10 and 1.61 eV of for LI, Na and K respectively (84). The discrepancy probably reflects the relative ease of overlap between adjacent p-orbitals and suggests that the overlap is most favorable for the smaller Li atom.

(iv) By at least the septemer stage, the orbital composition is comparable to that of the bulk metal.

Chapter Five

LITHIUM SUPEROXIDES

V.1 Introduction

The alkali superoxides have been studied extensively as prototypes for general metal atom-oxygen molecule interactions (85,94). The bonding of O_2 to metals has significant consequences in technology and nature in a number of areas including corrosive and catalytic processes and the physiological importance of hemoglobin. More recently, interest was further stimulated by the discovery that the color centers produced when O_2^- replaces X^- in the alkali halide crystals play a role in lasing that has potential applications for tunable solid state lasers that radiate in the visible (85,86).

The impetus for the current experiments was threefold:

(i) First, accurate measurements of the ESR parameters for LiO_2 and an examination of their dependence on the matrix involved had not been established. A complete ESR study of the alkali superoxides was presented by Lindsay (35,36), but the spectrum of LiO_2 was not conclusively assigned. And except for that tentative identification, no ESR spectra of LiO_2 have been previously reported.

(ii) Second, the possible inversion of the ground state symmetry from $^2A_2$ to $^2B_1$ for the heavier alkali superoxides, RbO_2 and CsO_2, was suggested by the Lindsay work and there was interest in finding out how LiO_2 would fit into the estimated crystal field splitting trend of the alkali superoxide series.

(iii) Third, was the need for a careful search for any evidence of $Li^+O_2^-$ geometries other than the C_{2v} already observed for the alkali superoxides. The pioneering IR and Raman studies of Andrews *et al* (34) on matrix isolated alkali superoxides strongly supported their being bound triatomic charge transfer species, $Li^+O_2^-$ of C_{2v} symmetry. This was confirmed by ESR experiments where the small hfs values support the conclusions of virtually complete electron transfer. While the IR, Raman, and ESR data are only consistent with an isosceles triangular geometry, theoretical calculations raised some question as to the true ground state geometry. There are three geometries for which a successful approach of a Li atom to an O_2 molecule can be expected. These give product geometries belonging to the $C_{\infty v}$, C_s and C_{2v} point groups,

$Li^+[-O-O]^-$

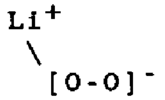

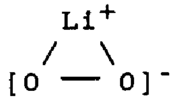

respectively. The lowest energy states and corresponding electron configurations for the charge transfer species $Li^+O_2^-$ under those three geometries are:

$C_{\infty v}$: $1\sigma^2 2\sigma^2 3\sigma^2 4\sigma^2 5\sigma^2 1\pi^4 6\sigma^2 2\pi^3$ $^2\Pi$

C_s: $1a'^2 2a'^2 3a'^2 4a'^2 5a'^2 1a''^2 6a'^2 7a'^2 2a''^2 8a'$ $^2A'$
................................$2a'' 8a'^2$ $^2A''$

where these lowest states, $^2A'$ and $^2A''$, of C_s are the degenerate components of the ^{2} state for $C_{\infty v}$.

C_{2v}: $1a_1^2 1b_2^2 2a_1^2 3a_1^2 2b_2^2 4a_1^2 1b_1^2 5a_1^2 1a_2^2 3b_2$ $^2B_2$
................................$1a_2 3b_2^2$ $^2A_2$

The potential energy surfaces of the reactants, $Li(^2S_g)$ + $O_2(^3\Sigma_g^-)$ correlate to the following states of each product geometry. For $C_{\infty v}$, the proper states are $^4\Sigma^-$ and $^2\Sigma^-$: for C_s, the states are $^4A'$ and $^2A'$: and for C_{2v} the states are $^4B_1$ and $^2B_1$. That is, the reactants do not correlate with any of the electronic states of LiO_2 with $C_{\infty v}$ and C_{2v} geometries. Instead, essentially all successful collisions will occur for C_s geometries giving $^2A''$ as either the ground or first excited state of the ion pair (87,90).

Starting at the simplistic level of a Walsh diagram for AB_2 tiatomics (93), the predicted geometry for LiO_2

(with 13 valence electrons) is linear with $D_{\infty h}$ symmetry. Constraining it to a C_{2v} geometry predicts $^2B_2$ to be slightly below the $^2A_2$ state. Modifying the description to the HAB form of the Walsh diagram (and neglecting Li core 1s orbital electrons) gives a predicted C_s geometry with an angle of ˜105° and a $^2A''$ ground state analogous to the geometry of HO_2 (88,94). Apparently BO_2 is the simplest dioxide molecule for which Walsh diagrams are applicable (90). Moving on to the more sophisticated *ab initio* calculations, the pioneering work on LiO_2 of Billingsley and Trindle (87) predicted the true ground state to have the C_s geometry. When the molecule was constrained to the C_{2v} geometry, their calculations predicted $^2B_2$ to be the ground state. A more complete *ab initio* SCF calculation carried out by O'Neill (90) predicted that for C_{2v}, the $^2A_2$ state was 14kcal/mol below the $^2B_2$ state and gave ground state geometry values that were in good qualitative agreement with those estimated from the experimental data of Andrews *et al*. O'Neill, however, tempered his results with several observations:

1) The energy difference between the $^2A_2$ and $^2B_2$ states and the great similarity in their equilibrium geometries is analogous to *ab initio* predictions for HO_2 (95). This is suspicious since LiO_2 is expected to be much more ionic than HO_2 and, therefore, should have a less analogous electronic structure.

2) Similar calculations on the C_{2v} and $C_{\infty v}$ forms predict little or no energy barrier between the two geometries.

3) The $^2A_2$ ground state wave function correlates with the $^2A''$ wave function which is a wave function of both the C_s form and one of the degenerate members of the $^2\Pi$ state of the $C_{\infty v}$ form. The $^2\Pi$ state is predicted to lie only 1.2 kcal/mole above the $^2A_2$ state. This very small energy difference is interpreted as suggesting that the true equilibrium geometry is, again, C_s, in analogy with HO_2.

V.2 Spectra and Analysis

The ESR spectra of LiO_2, in agreement with those of the other alkali superoxides, consists of three transitions corresponding to the principle values of an orthorhombic $\bar{g}$ tensor. The downfield transition, g_z coincides with the O-O axis. The first derivative g_x transition corresponds to the C_2 symmetry axis and the transition g_y corresponds to an axis perpendicular to the molecular plane. This labelling corresponds to g_{zz}, g_{xx}, g_{yy} (35) and to g_3, g_2 and g_1 (34) in the ESR references cited previously.

For LiO_2 there is no significant quadrupole interaction, and the field position of transitions, to first order, is given by

$$H_i(I,m_I) = (g_e/g_i)(H_e - A_i m_I) \qquad [5.1]$$

where $A_i = a + T_i$, $i = x$, y or z.

For spectra where the hf detail is resolved, the parameters g_i and A_i can be measured directly. For the $I=3/2$ case

$$(g_e H_e)/g_i = (1/4)\{[H_i(+3/2)+H_i(-1/2)] + [H_i(-3/2)+H_i(+1/2)]\} \qquad [5.2]$$

and

$$(g_e A_i)/g_i = (1/2)\{[H_i(+1/2)-H_i(+3/2)] + [H_i(-3/2)-H_i(-1/2)]\} \qquad [5.3]$$

and for the $I=1$ case

$$(g_e H_e)/g_i = (1/4)\{[H_i(+1)+H_i(0)] + [H_i(0)+H_i(-1)]\} \qquad [5.4]$$

$$(g_e A_i)/g_i = (1/2)\{[H_i(+1)-H_i(0)] + [H_i(0)-H_i(-1)]\} \qquad [5.5]$$

Where the hf detail is not resolved

$$g_i = (1/2)(H_{max} + H_{min}) \qquad [5.6]$$

where H_{max} and H_{min} are the maximum and minimum field positions of the unresolved first derivative signal or the full width at half maximum height (FWHM) of the absorption or emission like signals.

There was greater variability in the depositions for producing good spectra than was found for bare Lithium clusters. Table V.1 summarizes the conditions that produced the most useful spectra. Although those samples grown at lower $P_{O_2+matrix}$ pressures (~750 mtorr) gave the best results, the quality of the spectra were not predictable. For example, while the g values for a given matrix were invariant, hf details present in the spectra of one run might be absent in a second sample produced under the same nominal conditions. Generally photolysis produced an increase in the intensity of the g_x transition but had little effect on the intensity or resolution of g_z or g_y. Photolysis also did not cause production of LiO_4 which did appear occasionally as a post-anneal contaminant although its occurrence was not consistent. A similar unpredictability was found for the number of matrix sites, as well as their intensities and stabilities with respect to temperature changes or photolysis time, for Li atom signals. In some Krypton matrices, for example, up to 18 prephotolysis, preannealed atom sites were observed. In some samples 1 or 2 sites remained intense after photolysis and/or annealing. In others, photolysis caused the complete irreversible disappearance of the signals.

Details of spectra in various matrices are outlined below:

Table V.1 Summary of deposition conditions for LiO_2 production.

Matrix	Total Dep. hrs.	Li flux A/sec	P_{O_2} mtorr	P_{O_2}+Matrix[(a)] mtorr
N_2	5-6	0.1-1.4	5-19	730-740/955
Ar	6-7	0.5-3.0	4-20	750-760/960
Kr	7-8	0.5-1.5	2-23	750-760/ 930-950
Ne	2-5	0.5-0.75	15	450-550

(a) The two sets of values are for two sets of deposition pressures.

(i) Nitrogen matrices: Figure V.1 shows the spectrum of $^7LiO_2$ at 4.2°K. The g_z value at 2.067 has a well resolved hf quartet, A_z=2.3G. The derivative signal of g_x shows no hf detail. The g_y region is overlapped by the strong triplet N atom signal. Generally the Nitrogen atom signals were very intense. In one sample, however, annealing bleached them out. The process is shown in Figure V.2. In spectrum (a), taken at 20.5°K, the signal at 2.10123 is the g_2 value associated with LiO_4. Increasing the temperature to 25.5°K brings out the g_1 transition of LiO_4 at 2.0413. There was a corresponding increase in the g_2 signal and a decrease in the N atom intensities. Curiously, dropping the temperature back to 5.7°K produced spectrum (c) where the g_z and g_x transitions of LiO_2 show up at 2.068 and 2.008 respectively. The signals had full widths at half max of 13.7 and 9.4 G respectively, but showed no hf detail. The N atom signals have vanished but no strong feature for g_y is observed suggesting that it lies too close to g_x to be resolved. In contrast to typical postannealed spectra no evidence of the LiO_4 signal remained. $^6LiO_2$ samples gave g_z and g_x without any hf detail. The g_y regions were consistently obscured by the Nitrogen atom transitions.

(ii) Krypton matrices: The g_z, g_x and g_y values were 2.0570, 2.0094 and 2.0027 respectively. Figure V.3 shows the ESR spectrum of $^6LiO_2$ at 4.2°K.

Figure V.1 ESR spectrum of $^7LiO_2$ in a Nitrogen matrix at 4.2°K.

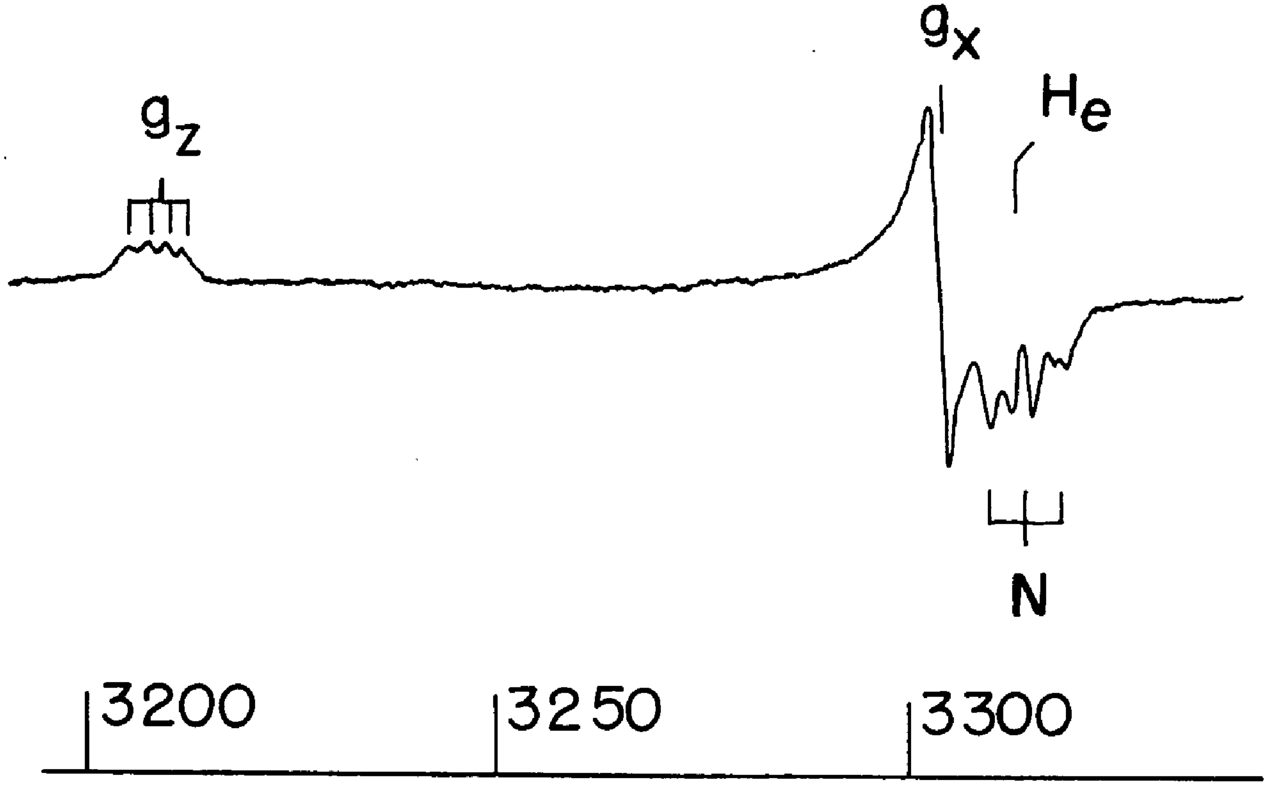

Figure V.2 ESR spectra for $^7LiO_2$ in N_2 at several temperatures. (a) taken at 20.5°K shows the g_x transition of LiO_2 between the g_2 transition of LiO_4 and the strong triplet signal from N atoms in the matrix. (b) taken at 25.5°K shows an increase in the g_2 as well as the appearance of the g_1 transition of LiO_4, and a decrease in the N signal intensity. (c)is the postanneal spectrum taken at 4.2°K. The signals associated with LiO_4 and N are no longer evident. The g_z signal of LiO_2 is observed and there is a noticable increase in the intensity of the g_x signal. There is no sharp indication of the g_y transition.

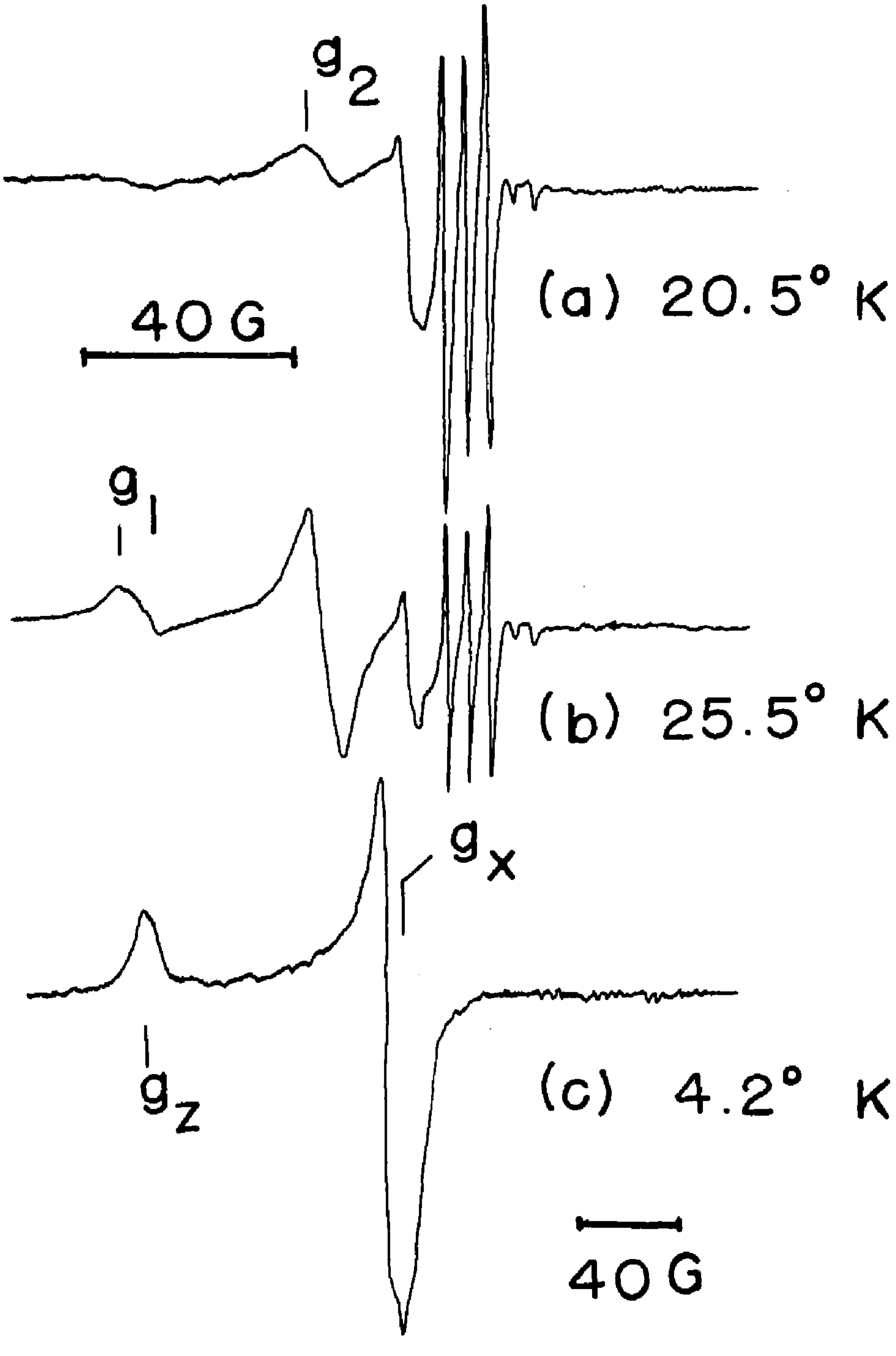
g2
(a) 20.5° K
40 G
g1
(b) 25.5° K
gx
gz
(c) 4.2° K
40 G

Figures V.4 and 5 show the hf detail of the transition of g_z transition of $^6LiO_2$, and the g_y transition of $^7LiO_2$. The splittings were 0.97G and 2.65G respectively. The extra lowfield peak in Figure V.4 probably arises from the overlap of two closely spaced site signals. No hf detail was observed for g_x.

(iii) Argon matrices: These matrices gave values of $g_z=2.069$, $g_x=2.008$ and $g_y=2.004$. Figure V.6 shows the spectrum of $^6LiO_2$. The spectrum was recorded at 10°K after a 155 min photolysis. The Li atom transitions show an unusual intensity distribution. Figure V.7 shows the hf quartet of the g_z transition of $^7LiO_2$. Again, as in other matrices, no hf detail is observed for the g_y transition.

(iv) Neon matrices: These matrices were difficult to produce and maintain and generally had very poor S/N character. Figure V.8 shows a spectrum of $^6LiO_2$. The g_z transition occurs at 2.061. g_x at 2.0097 is partly overlapped by the $m_I=0$ atom transition. No g_y signal is apparent in this sample.

Table V.2 summarizes the observed magnetic parameters of LiO_2 in the various matrices.

V.3 Discussion

ESR data on LiO_2 are consistent with ionic model $Li^+O_2^-$ of C_{2v} geometry and $^2A_2$ ground state. Spectra

<u>Table V.2</u> Magnetic parametes of LiO_2 in various matrices.(a)

	Matrix	g_z	g_x	g_y	a_z	a_y
					in Gauss	
$^7LiO_2$	N_2	2.0667(3)	2.0080(2)	-	2.33(8)	-
$^6LiO_2$	"	2.0677(1)	2.0083(3)	-	-	-
$^7LiO_2$	Ar	2.0697(1)	2.0082(2)	2.0034(7)	2.19(4)	3.25
$^6LiO_2$	"	2.0690(3)	2.0082(8)	2.0035(1)	-	
$^7LiO_2$	Kr	2.0570(1)	2.0095(1)	2.0026(13)	3.01(5)	2.65
$^6LiO_2$	"	2.0573(1)	2.0093(2)	2.0028(1)	0.97(3)	0.82
$^6LiO_2$	Ne	2.0606(12)	2.00965(8)	-	-	-

(a) No hf details were observed for any g_x transition.

Figure V.3 ESR spectrum of $^{6}LiO_2$ in a Krypton matrix at 4.2K. The g_z, g_x and g_y transitions are labeled. The additional signals are unreacted ^{6}Li atoms.

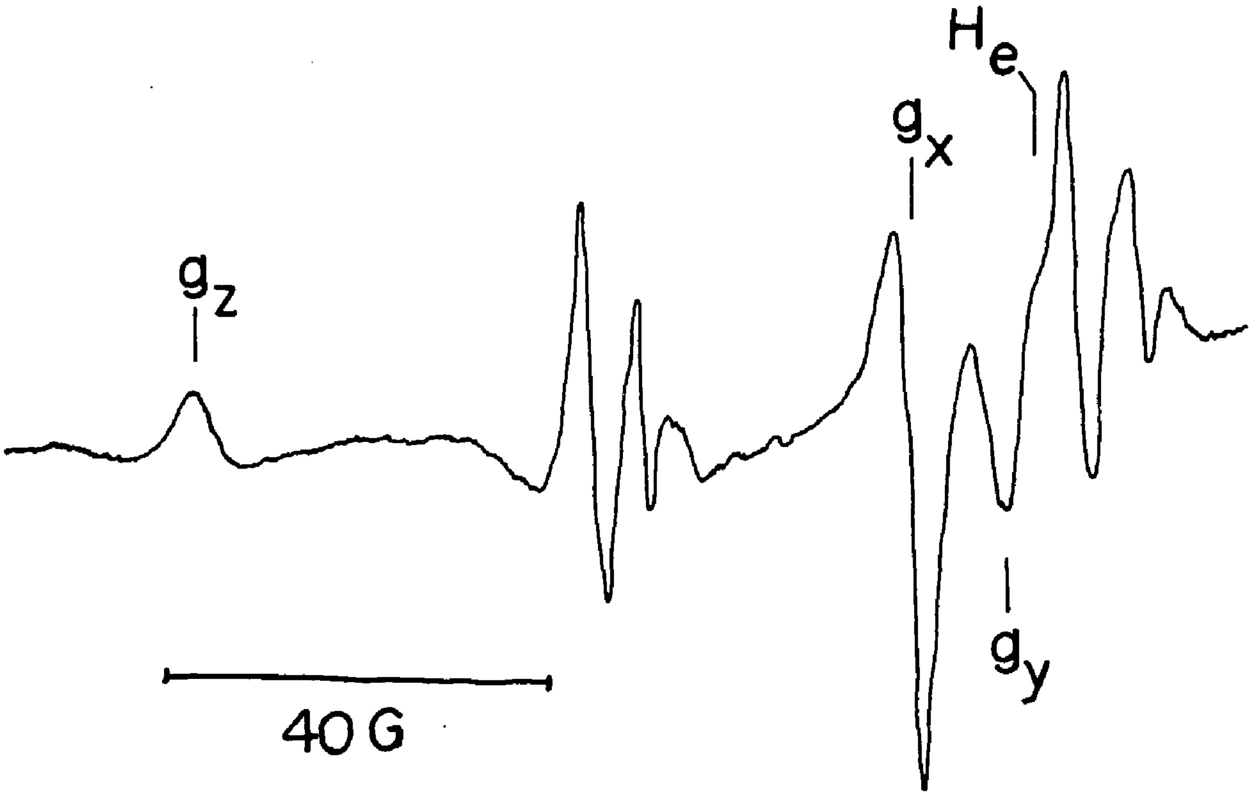

Figure V.4 Detail of the g_z region of $^6LiO_2$ in a Krypton matrix at 4.2K. The hf splitting is 0.97G. The quartet of hf signals is due to the overlap of signals from two sites.

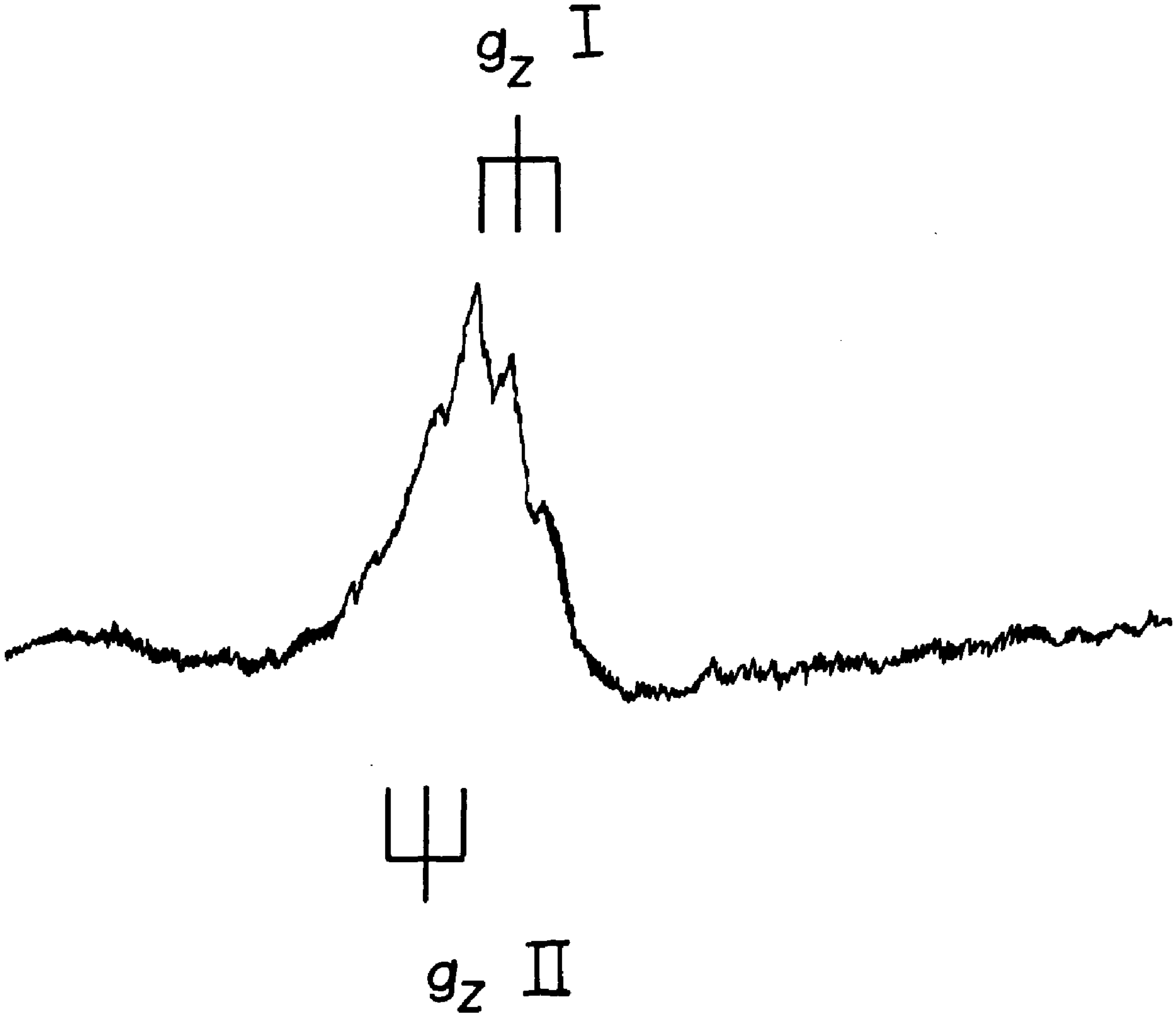

Figure V.5 Detail of g~2 region of $^7LiO_2$ in a Krypton matrix. The g_y transition has a hf splitting of 2.65G. The g_x signal shows no hf detail.

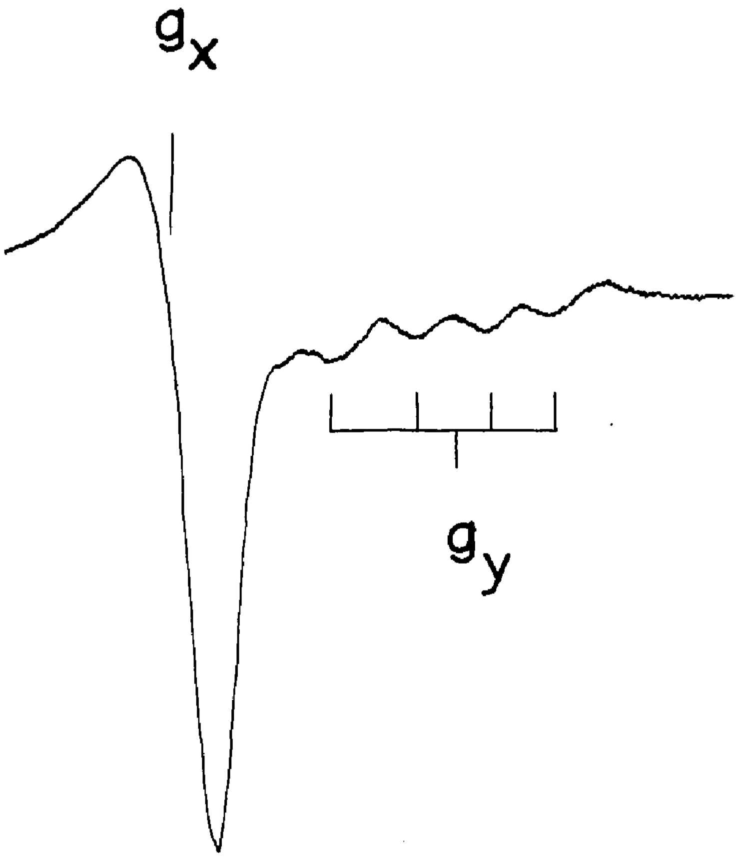

Figure V.6 ESR spectrum of $^6LiO_2$ in Argon at 10K after 155 min of photolysis. The g_z, g_y and g_x transitions are clearly visible. No hf details are present in this sample. Me denotes methyl radical transitions. The Li atom transitions show an unusual intensity distribution.

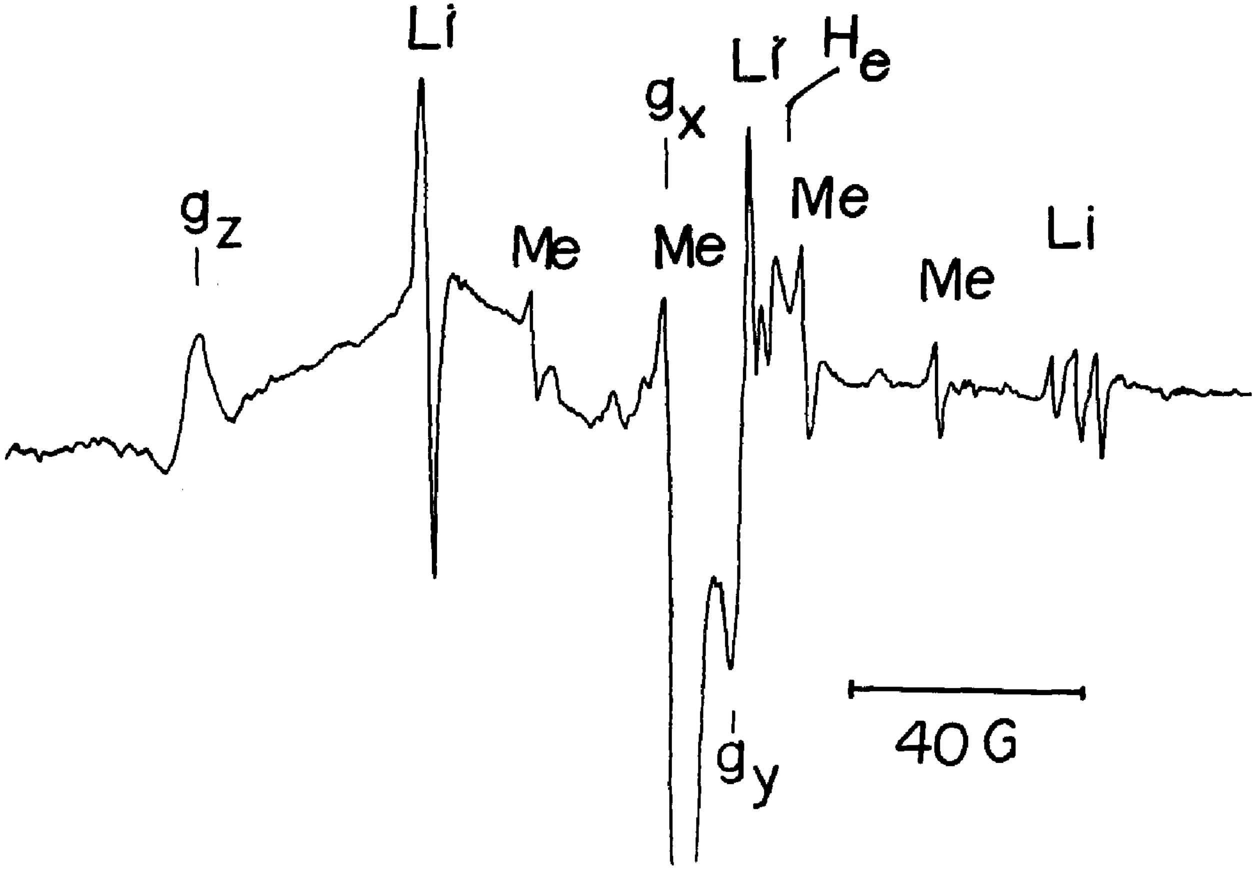

Figure V.7 Detail of the g_z transition of $^7LiO_2$ in Argon.

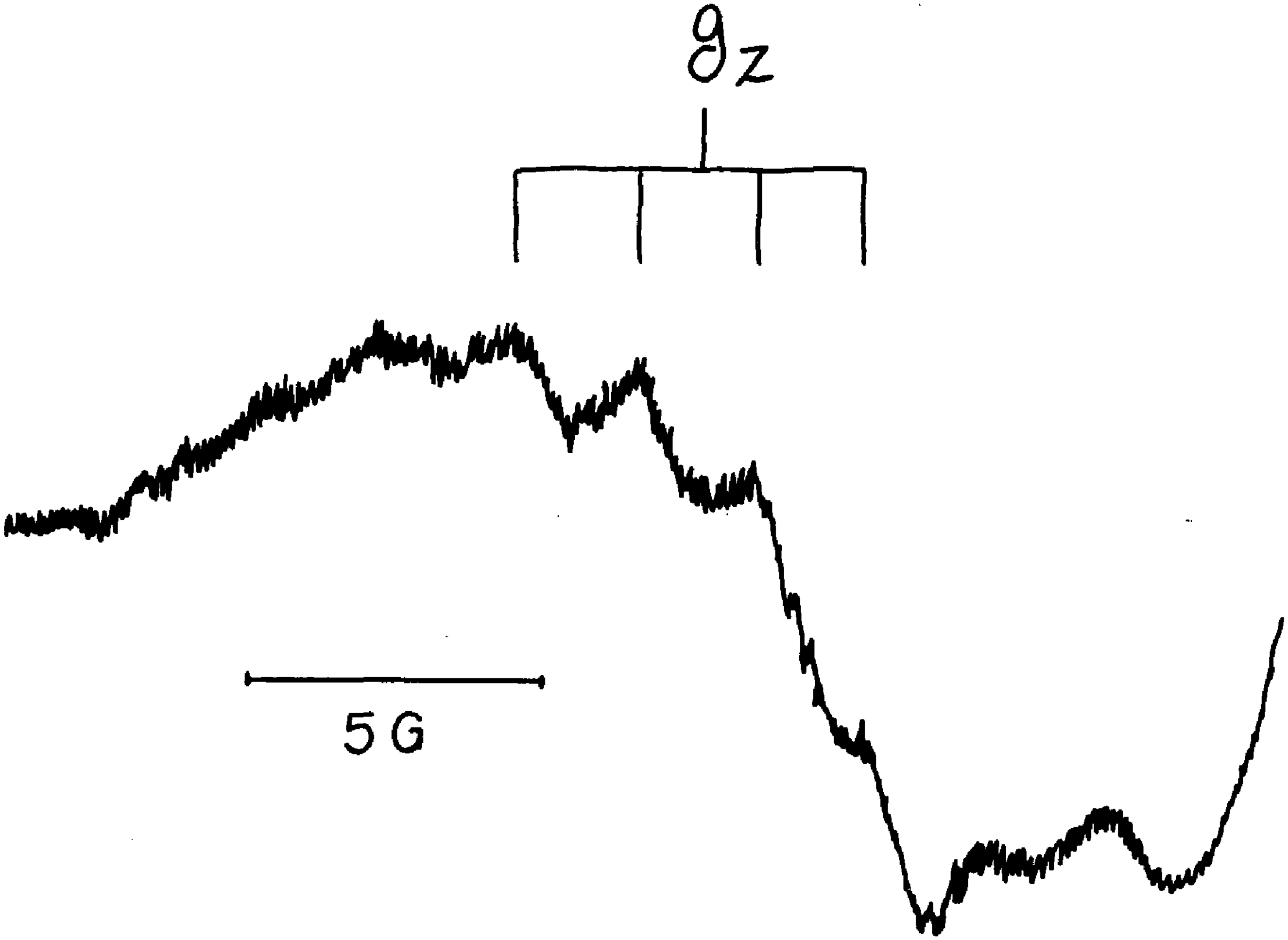

Figure V.8 ESR spectrum of $^6LiO_2$ in a Neon matrix. Li denotes unreacted ^6Li atom signals.

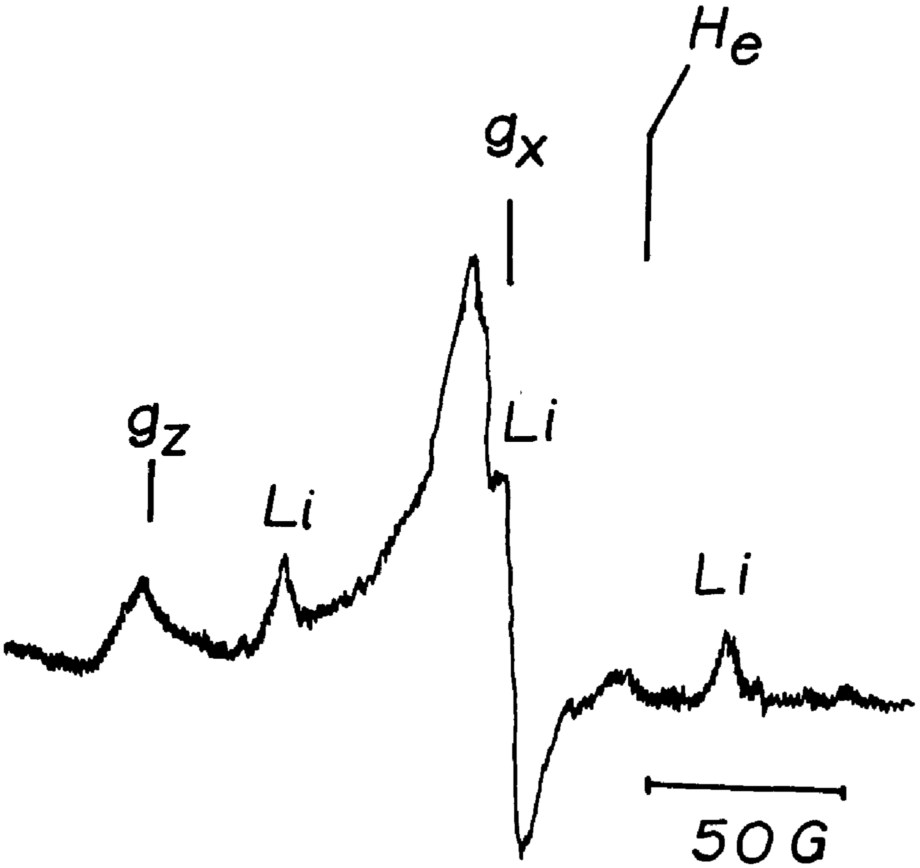

showed a triplet structure arising from the three principle axes of the orthorhombic g tensor. Hf detail occurs because the electron tansfer is not entirely complete and some spin density is left on the Li cation. The resolution of the hf components was not consistent from experiment to experiment in a given matrix (as noted previously). The g_x transition was always narrow (5-8G) and showed no hf detail in any of the matrices. The g_z and g_y transitions were broader (10-20G) and hf details, (generally weak), were sometimes observed. Tortional motion along an axis will cause broadening of the lines associated with the other two axes by modulating their orientations with respect to the external magnetic field. Tortional motion about the z axis is favored because of the low moment of inertia, and also because motion along this axis doesn't alter the electrostatic interaction between the M^+ and O_2^- ions. This qualitatively explains the broadening of g_z and g_y. Slight differences in the matrix gas:O_2 gas mixture can affect the lattice structure, modifying the dimensions of trapping sites, which in turn effects the degree of tortional motion. This may explain the variable occurrence of hf detail for a given matrix. Estimates of the dimensions of trapping cages have been made for the tetrahedral (4 atom substitutions) and octahedral (6 atom substitutions) sites of several pure noble gas matrices.

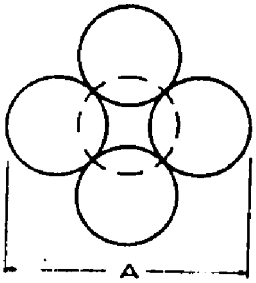

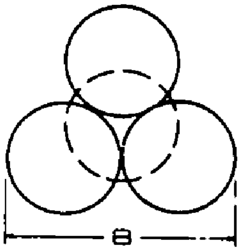

	A	B
Ne(96)	7.56A	6.26A
Ar(97)	9.07A	7.52A
Kr(98)	9.65A	8.00A

Using an averaged Li-O distance of 1.8A and O-Li-O angle of ~44° from values summarized by Grow and Pinter (91) give an estimated O-O distance of 1.25A. Doubling this to allow for extension of the p orbitals indicates that LiO_2 fits easily within the cages and, indeed, has a significant amount of room to "rattle" about in.

Where hf was observed, the anisotropic character was negligable compared to that of the corresponding electronic Zeeman. Therefore, the hf corresponds to the principle axes of $\bar{g}$, which are not necessarily the same as those of $\bar{A}$. In that case, the average, even if the signs of the individual a's were known, would not equal the isotropic hf constant. Detailed analysis done on the NaO_2 and $NaSO_4$ systems by Adrian showed that the two sets of axes were coincident. By analogy, the axes are considered coincident for LiO_2 as well.

Figure V.9. shows a schematic of the molecular orbitals of the alkali superoxide system. The presence of the alkali cation lifts the degeneracy of the HOMO of the O_2^- anion into an in-plane component, π_x^*, of b_1 symmetry, and an out-of-plane member, π_y^*, of a_2 symmetry. Next to each of the six MOs constructed by mixing the O_2^- valence orbitals with the symmetry allowed combinations of alkali p and d orbitals are the coefficients relevant to the covalent mixing. Only π_x^* can mix with the p_z orbital of the cation, lowering its energy relative to π_y^* and thereby lifting the degeneracy. The unpaired electron occupies the out-of-plane orbital and gives the system a $^2A_2$ ground state. The crystal field splitting parameter, δ, measures the extent to which the cation lifts the degeneracy of the π antibonding pair. The g values summarized on Table V.2 are sensitive to the matrix involved, the g_z transitions more so than the g_x and g_y values which remain close to the free electron value. The principle components of the g tensor can be described by (100,101)

$$\Delta g_z \simeq +2\lambda_o/\delta \qquad [5.1]$$

Figure V.9 Schematic of the molecular orbitals of $M^+O_2^-$. (Ref.36).

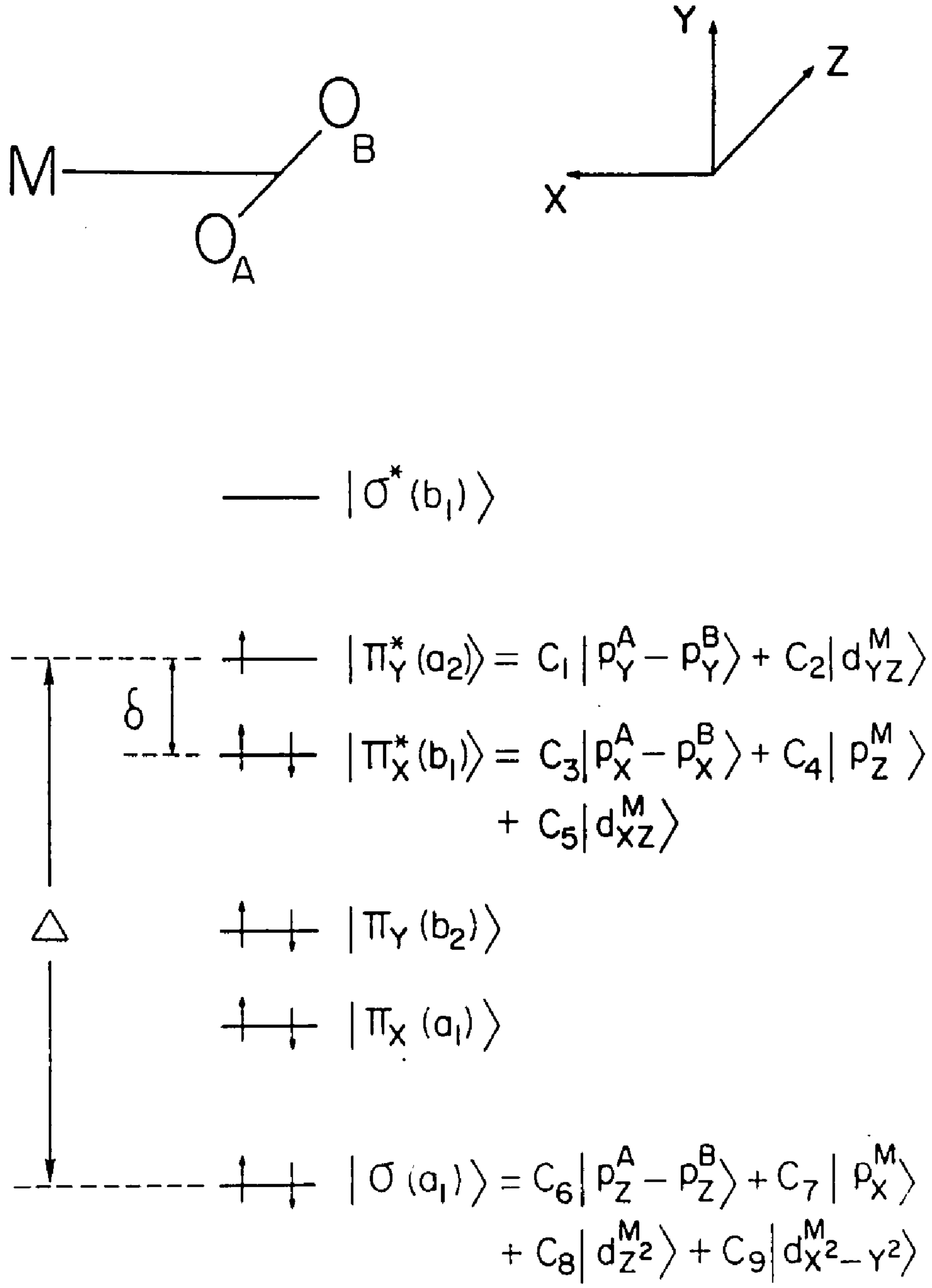

$$\Delta g_y \sim -\lambda_o^2/\delta^2 \qquad [5.2]$$

$$\Delta g_x \sim +(2\lambda_o/\Delta) - (\lambda_o^2/\delta^2) \qquad [5.3]$$

where $\Delta g_i = g_i - g_e$ gives the shift away from the free electron value; $\lambda o \sim 150$ cm^{-1} (84), is the spin orbit coupling constant of O_2; δ is the split between the in and out of plane components of π^*; and Δ is the seperation of the $\sigma(a_1)$ and the $\pi^*(a_2)$ orbitals. Although values of δ can be estimated from both [5.1] and [5.2] only [5.1] is used in the following discussion. Eq.[5.2] gives larger values of δ, and due to the presence of the square factor, smallcalibration errors in evaluating g_y will cause large errors in the estimated value of δ. Using Eqs.[5.1] and [5.3], the value of Δ can be estimated for LiO_2. In the various matrices this value falls within the range of 40-45,000 cm^{-1} which agrees well with the values of O_2^- in other systems (100,101) including the heavier alkali superoxides (36). Variations in δ with matrix reflects matrix effects on the alkali-oxygen distance. Table V.3 summarizes the estimated δ values for LiO_2 in the various matrices.

Table V.3 Experimental crystal field splittings for LiO_2 in various matrices.

Matrix	g_z	Δg_z	δ, cm^{-1}
N_2	2.0667	0.0644	4660
Ar	2.0697	0.0677	4430
Kr	2.0570	0.0547	5490
Ne	2.0590	0.0577	5200

Finally,as noted in section, the near *ab initio* SCF-LCAO-STO-MO computations predicted two stable forms of LiO_2 of comparable energy (87). The isosceles triangle, C_{2v}, observed in matrix work and a C_s species analogous to HO_2 where Li is bound at an angle of 135 to one of the oxygen atoms (88). The low force constant for motion of the Li atom parallel to the O-O axis implied by the IR data prompted Andrews to propose the possible photoisomerization of the C_{2v} to the C_s species (89). SCF calculations (90-92) suggested that the C_{2v} form might represent a matrix mediated equilibrium geometry, but that the true energy minimum is the C_s geometry. Proposed explanations for why the C_{2v} geometry is the only one observed even though the C_s form is expected to be more stable, include the possible dependence of the product geometry on the method of preparation; that the C_s form's signals are swamped by the greater intensity of IR transitions in systems with largely ionic bonding (C_{2v}) relative to systems with predominantly covalent bonding (C_s); or that the C_{2v} form is kineticly more stable because, unlike the C_s form which has a channel back to the reactants, the C_{2v} form must change its electronic state from a $^2B_2$ ground state to $^2A_2$ in order to dissociate or isomerize. This last argument comes from the Billingsly calculations (87) which predict $^2B_2$ as the ground state. That experiment and other computational methods support the $^2A_2$ ground state does not invalidate the rest of their argument.

In an ionic molecule, $M^+O_2^-$, the largest g shift is predicted to be associated with the oxygen internuclear axis (99,100), regardless of the angle of approach of M^+ to O_2^-. Eq.[5.1] can be rewritten in the more general form

$$\Delta g_z = 2\lambda_o[\lambda_o^2 + \delta^2]^{-1/2} \qquad [5.4]$$

where $\delta << \lambda_o$

From this, it is predicted that

$$\lim_{\delta \to 0} . \Delta g_z = 2$$

where by symmetry, this limit should be found when $C_{2v} \rightarrow C_s \rightarrow C_{\infty v}$. If an alternative geometry did occur, there should be a substantially larger shift in the g_z value. However, a careful search of the spectra in the various matrices under varying conditions of temperature and exposure to photolysis failed to provide evidence of a second geometry. This supports C_{2v} as being the true ground state geometry.

V.4 Comparison of δ for the Alkali Superoxides

The simple ionic model predicts a monotonic decrease in δ with an increase in R, the distance from the cation to the O-O bond. Tables V.4 and 5 compare the values of δ for the alkali superoxides in Argon and Krypton respectively. The absolute value of δ decreases from $LiO_2 \rightarrow RbO_2$ and then increases for CsO_2 in contradiction to the simple ionic model. The ionic model can be improved by allowing for polarization of the ionic orbitals and/or by including covalent bonding. Lindsay (36) has presented a detailed description of two models which can account for this nonmonotonic trend in δ, the reversal case and the inversion case.

(i) Reversal case: The value of δ remains positive down the alkali series but additional interactions, either ionic or covalent in nature, decrease its magnitude. Covalent interactions involve the mixing in of d-orbitals from the cation with π^* pair of O_2^-. In the alkali series the energy of the d-orbitals admixture will decrease the energy of both members of the π^* pair since both can mix with the d-orbitals. An ionic interaction can arise from the partial quenching of the polarizability of the pair. As the in-plane orbital, $\pi_x^*(a_2)$ expands toward M^+, it is counteracted by repulsive short range forces between the ionic cores of M^+ and O_2^-. No such restriction applies to the out-of-plane orbital, $\pi_y^*(b_1)$. In reality, however,

Table V.4 Experimental crystal field splittings for the alkali superoxides in Argon matrices.(a)

	R(b), A	g_z	Δg_z	δ (cm^{-1})
$^{7}LiO_2$	1.64	2.0697	0.674	+4450
$^{23}NaO_2$	1.96	2.1136	0.1113	+2700
$^{39}KO_2$	2.18	2.1181	0.1158	+2590
$^{87}RbO_2$	2.48	2.1196	0.1173	±2560
$^{133}CsO_2$	2.59	2.1090	0.1067	±2810

(a) All values except LiO_2 are from Ref.36.

(b) Distance from M^+ to midpoint of O_2^- bond from Ref.34.

Table V.5 Experimental crystal field splittings for the alkali superoxides in Krypton matrices.(a)

	g_z	Δg_z	δ (cm^{-1})
$^{7}LiO_2$	2.0570	0.547	+5485
$2^{3}NaO_2$	2.1106	0.1083	+2770
$3^{9}KO_2$	2.1184	0.1161	+2585
$^{87}RbO_2$	2.1227	0.1204	±2490
$1^{33}CsO_2$	2.1069	0.1069	±2870

(a) All values except LiO_2 are from Ref.36.

since the electron cloud is not a point charge, this orbital too may be partially quenched by the charge cloud of the cation. This effect will increase with increasing cation size.

(ii) Inversion case: The value of δ is positive down to RbO_2 and /or CsO_2 where the in-plane orbital becomes less stable than the out-of-plane orbital and the ground state changes from $^2A_2$ and $^2B_1$. This can arise from fairly weak covalent mixing of the anion valence orbitals with the inner shell p-orbitals of the cation. For the heavier alkalis the energy of the p-orbitals are above that of the pair so that admixture will increase their energy. Since the b1 member is the only one allowed by symmetry to interact with the p_z orbitals of the metal, this MO will increase in energy while the value of the a_2 member remains constant. The net effect is that the value of δ decreases. If the interaction is large enough the energy of the b_1 orbital will be pushed above that of the a_2 orbital and the ground state will have inverted.

As just described qualitaively, the ionic model can be improved by including the polarizabilities of M^+ and O_2^-. Assuming that the in-plane $\pi_x{}^*(b_1)$ is quenched, its energy remains the same as in the simple ionic model. However, the out-of-plane $\pi_y{}^*(a_2)$ can be polarized, so that its energy decreases. This can account for the inversion case. If the model is further modified so that the out-of-plane component can also be partially quenched, the reversal case will be expected, since the quenching will increase with increasing M^+ size. Therefore, introducing the polarizability does not make one model less likely than the other.

In terms of covalent mixing, the inversion case is slightly favored. In the inversion case, covalent mixing of the π^* orbitals with the alkali inner shell p orbitals increases the energy of the in-plane component because by symmetry it is the only member that can interact with p_z of the cation. The mixing increases as you go down the alkali series. In the reversal case, covalent mixing involves the cation p, d, and f orbitals, and requires about a 20% admixture of d-character (36). This is rather high in view of the vibrational spectra data (34).

Depending on the interpretation of the sign of δ, the data of Table V.4 (or V.5) can be arranged in two patterns corresponding to the two models. This is illustrated in Fig. V.10. Ignoring the LiO_2 value, for the reversal case, the values are grouped together in a plateau ~1000 cm^{-1} wide, as represented by the solid line. In the inversion case, the values between NaO_2 and CsO_2 cover a large jump of ~6000 cm^{-1}. Including the LiO_2 value, for the reversal case, it is isolated from the plateau of the other δ values. However, for the inversion case, the gap

Figure V.10 Qualitative representations of the δ values of the alkali superoxides in terms of an inversion model (- - -), and a reversal model (——). (Ref.36.)

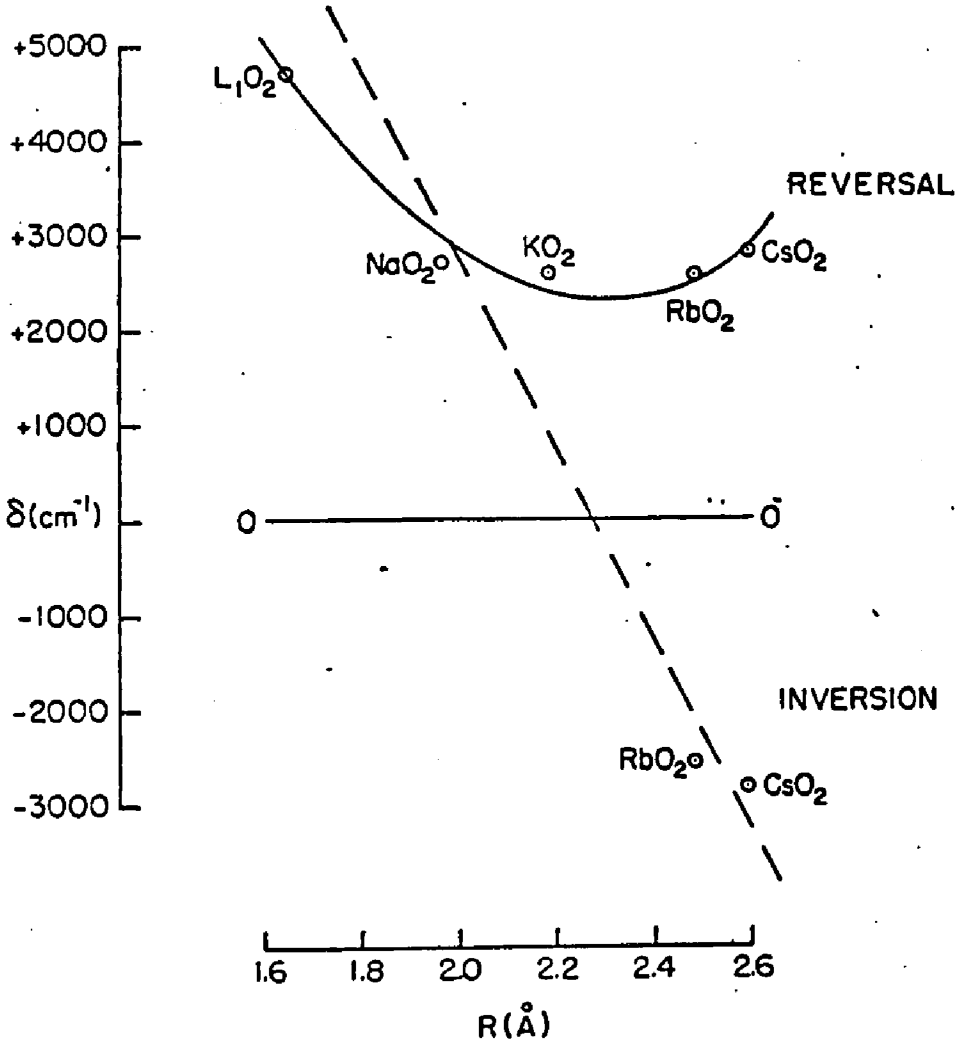

between LiO_2 and NaO_2 is comparable to the gap between NaO_2 and CsO_2. THe LiO_2 value suggests that the inversion case is more the likely. Taken together with the arguments that inner shell bonding analogous to the alkali monoxides is plausible (36) and that the degree of covalency required to account for the observed hf in CsO_2 seems unreasonably high, there is strong support for the inversion of states model in explaining the trend in δ for the heavier alkali superoxides.

Appendix A.1 Reprint: J. Chem. Phys. 80, 4761 (1984)

ESR spectra of matrix isolated Li_7 clusters

D. A. Garland and D. M. Lindsay
Department of Chemistry, City University of New York, The City College, New York, New York 10031

(Received 16 January 1984; accepted 17 February 1984)

ESR spectra assigned to $^6Li_7$ and $^7Li_7$ have been produced by co-depositing atomic lithium with excess argon in a liquid helium cooled cryostat. The spectra are characterized by an isotropic g value, $g_0 = 2.00045(6)$ for $^7Li_7$, and hf coupling constants $a_1 = 36.39(5)\ G$ for two equivalent ^7Li nuclei plus $a_2 = 2.19(2)\ G$ for (most likely) five equivalent ^7Li nuclei. Both g_0 and a_2 show a small temperature dependence in the range 4.1–30 K, but the mechanism for this effect remains open. As in the case of Na_7 and K_7, the ESR spectra may be interpreted as arising from a pentagonal bipyramidal molecule with ground state symmetry $^2A_2''$. The average p character for Li_7 is much greater than in the corresponding sodium and potassium septemers and, if $a_2 < 0$, is comparable in magnitude to the hybridization of the bulk metal.

I. INTRODUCTION

Previous electron spin resonance (ESR) studies have demonstrated that co-deposition of sodium or potassium with argon gives rise to an alkali trimer molecule[1,2] plus an additional cluster believed to be the alkali septemer.[3] The hyperfine (hf) splitting pattern of the septemer was characteristic of a single upaired electron of dominant s character, largely confined to two equivalent nuclei but having a small spin population on a second set of (most likely) five equivalent nuclei. It was deduced from extensive simple Hückel calculations that a likely structure for Na_7 and K_7 was a pentagonal bipyramidal geometry with ground state symmetry $^2A_2''$.

In this paper we report ESR spectra for the analogous ^6Li and ^7Li clusters and note that these results confirm the original assignment of the stoichiometry, structure, and bonding of the sodium and potassium septemers. We further note that recent *ab initio* calculations[4] predict not only an exceptional stability for the pentagonal bipyramidal geometry but also hf coupling constants in reasonable agreement with those observed. In this context it is interesting to add that, despite the cubic structure of most solids, the preferred packing arrangement for seven atom clusters is pentagonal bipyramidal. Indeed, the general importance of pentagonal symmetry in the nucleation and growth sequence of small clusters and microparticles has been recognized for some time.[5-7] A prevalance of polyicosahedral structures has been observed by electron microscopy on large supported aggregates[8-10] and by electron diffraction studies on gas-phase argon clusters in the range of 20 ~ 50 atoms.[11,12] However, until quite recently the experimental evidence for a preferential formation of "magic number" cluster sizes has been absent. In fact, for neutral aggregates, then aside from the work presented here and in Ref. 3, we know only of the mass spectral results of Sattler and co-workers on Xe[13] and Pb[14] clusters, the seeded beam study of Kappes *et al.*[15] on sodium clusters and the tentative identification of an icosahedral Sc_{13} cluster trapped in a neon matrix.[16]

II. EXPERIMENTAL

Lithium septemers were formed by co-depositing atomic lithium, either naturally abundant (Alfa, 99.9%) or isotopically enriched (Oak Ridge National Laboratory, 98% ^6Li and 99.9% ^7Li) with excess argon (Airco, 99.9998%) on a sapphire plate mounted inside a TE_{102} X-band ESR cavity. The cavity was attached to a variable temperature cryostat whose design has been described elsewhere.[1,2] Lithium was evaporated at approximately 500 °C from a water shielded Knudsen effusion source, metal fluxes being monitored by a quartz microbalance (Veeco, QM-301). For the spectra presented here, the Ar:Li ratios were approximately 30:1 with 0.3 μmol/h of Li incident on the sapphire plate and total deposition times of 5–7 h. At low Li fluxes (Ar:Li ratio ~400:1) and deposition temperatures close to 4.2 K, septemer intensities were weak and the dominant spectral feature was atomic lithium[17] in a single matrix site. The same ratio of Ar to Li, but now deposited at temperatures somewhat in excess of 4.2 K ("warm deposition" conditions, as described in Ref. 1) resulted in a fourfold decrease in the atom signal and an approximate doubling of the septemer intensity. The 30:1 ratio of Ar:Li gave a further enhancement of 2–3 in the septemer intensity, without introducing any noticeable spectral perturbations. All experiments were run at approximately the same Ar flux. Annealing by warming the matrix to 30 K gave a major improvement in spectral resolution but had little effect on Li_7 intensities. No further irreversible changes occurred provided the matrix temperature (measured with a carbon resistance thermometer accurate to ± 5%) did not exceed 30–35 K. As discussed previously,[18] no Li_3 spectrum was observed without photolysis except, possibly, a transient spectrum of the static trimer which disappears on annealing.

All spectra were recorded on a modified[18] JEOL ME-3X ESR spectrometer (microwave power 0.5–1 mW) using 100 kHz magnetic field modulation (peak-to-peak amplitude 0.25–1.5 G) and phase sensitive detection. The signal from the JEOL lock-in amplifier was further processed either with an active filter (typically a 1 s time constant for a scan rate of 2 G min^{-1}) or by averaging repetitive scans on a multichannel analyzer (Tracor Northern, TN 1710). The resonance frequency of the cavity plus sapphire plate and matrix sample, 9.2825 (2) GHz over the temperature range 4.2–30 K, was measured periodically with a microwave frequency counter (HP 5243L plus HP 5255 A plug in). Individual spectra were calibrated with a proton magnetometer (Micronow, model 515). Relative and absolute field positions are judged accurate to 0.5% and ± 1 G, respectively.

J. Chem. Phys. 80 (10), 15 May 1984 0021-9606/84/104761-06$02.10

III. SPECTRA AND ANALYSIS

Figure 1 shows the ESR spectrum assigned to $^7\mathrm{Li}_7$. This consists of seven groups of first derivative transitions (isotropic hf splitting a_1) centered near the resonance field $H_e = 3312.3(1)$ G for a free electron. No features corresponding to a zero-field splitting or to changes of greater than unity in the electron spin projection were observed.[19] The septemer exists in two principal matrix sites whose spectra are nearly overlapped at 4.2 K. As discussed in more detail below, the magnetic parameters show a noticeable temperature dependence so that for $T \sim 30$ K two comparably intense sets of transitions are resolved. In addition to atomic lithium[17] and $^7\mathrm{Li}_7$, several other relatively weak sets of transitions were observed in both the ^{6}Li and ^{7}Li experiments, but these have not been assigned to a paticular carrier. As discussed in Ref. 18, some of these spectra may arise from adduct formation between lithium and impurity molecules, e.g., H_2O. In one experimental run with ^{6}Li, what appears to be a very large cluster was observed. The ESR spectrum consisted of over 450 approximately equally spaced (but poorly resolved) transitions with a hf splitting of ~ 0.1 G.

A. Hyperfine structure

Since, qualitatively, Fig. 1 is remarkably similar to the spectra attributed to both Na_7 and K_7, the assignment of transitions closely follows that discussed elsewhere.[3] The septet structure arises from two magnetically equivalent $I = 3/2$ nuclei, whose total nuclear spin angular momentum has magnitude J_1 and projection M_1. Including terms up to second order in a_1/H, the transition fields of each origin are[1,3,19,20]

$$H(J_1,M_1) = \frac{g_e}{g_0}(H_e - a_1 M_1) - \frac{1}{2}\left(\frac{g_e}{g_0}\right)^2 \frac{a_1^2}{H}[J_1(J_1+1) - M_1^2], \tag{1}$$

where $g_e = 2.002\,32$ and g_0 are, respectively, the free electron g value and the (isotropic) g value of the cluster and H is the magnetic field at a particular transition.

As shown in Fig. 1, the first order and second order hf interactions cause a splitting into, respectively, seven groups $M_1 = +3, \ldots, -3$ each with a substructure $3 > J_1 > |M_1|$, for a total of 16 components. Superimposed on each (J_1, M_1) origin is a superhyperfine (shf) pattern of (most likely) 16 equally spaced transitions described by adding to Eq. (1) a term

$$H(M_2) = -\frac{g_e}{g_0} a_2 M_2, \tag{2}$$

where $a_2 < a_1$ is the shf splitting constant and $M_2 = \pm 1/2, \pm 3/2, \ldots$ is the nuclear spin projection quantum number for this second set of magnetically equivalent ^{7}Li nuclei.[21]

Figure 2 shows in more detail the $M_1 = -3$ region for $^7\mathrm{Li}_7$ in argon. The linewidth of these transitions $\Delta H_{pp} \simeq 300$–400 mG is remarkably small for a polycrystalline sample[22] and may, in fact, be limited by magnet inhomogeneities. Clearly visible are 16 transitions labeled $M_2 = +15/2, \ldots, -15/2$. A 16 line shf structure was also observed for $M_1 = +3$. However, because of the relative weakness of the outer transitions it is difficult to assign unambiguously an upper bound to $|M_2|$. Thus, as shown for the high field wing of $M_1 = -3$, the signal-to-noise (S/N) ratio for $M_2 = -15/2$ is approximately 3:1 and the S/N ratio of a hypothetical $M_2 = -17/2$ transition might be as low as 1:1.[23,24] A similar problem pertains to the ESR spectrum of Na_7.[3] However, the intensity data for the lithium experiments is considerably better than that for the corresponding sodium cluster. The shf arising from five equivalent ^{7}Li nuclei should have relative intensities 1:5:15:35:65:101:135:155:155:...:1, corresponding to $M_2 = +15/2, \ldots, -15/2$. For most (J_1, M_1) components, measured intensities are in quite good agreement with those expected for $^7\mathrm{Li}_7$. For example, the relative peak-to-peak heights (normalized to $M_2 = \pm 1.2$) for $M_1 = -3$ are 155(1):138(7):109(3):73(7):43(5):18(4):6(2):3(2), where these data represent an average of the $+M_2$ and $-M_2$ intensities with one standard deviation uncertainty in parentheses.[25] However, the ratio of shf intensities varies with (J_1, M_1) and is usually not quite symmetric about the origin. These distortions arise, apparently, from a partial overlap of the spectra of clusters in different matrix sites, the effect of which is accentuated at large M_2. Accordingly, the intensity data alone cannot rule out a nine atom cluster with seven equivalent $I = 3/2$ nuclei, but do make still larger clusters seems unlikely.

Table I compares the observed $H(J_1, M_1)$ for $^7\mathrm{Li}_7$ with those computed from Eq. (1) and the best fit parameters g_0 and a_1 given in Table II. Estimated errors (in parentheses) are one standard deviation uncertainty in the fit to the experimental data. However, the calibration errors noted earlier are larger. Table I includes average $\langle a_2 \rangle$ values determined for each (J_1, M_1) component; the mean (standard deviation in parentheses) of these values is given in Table II.

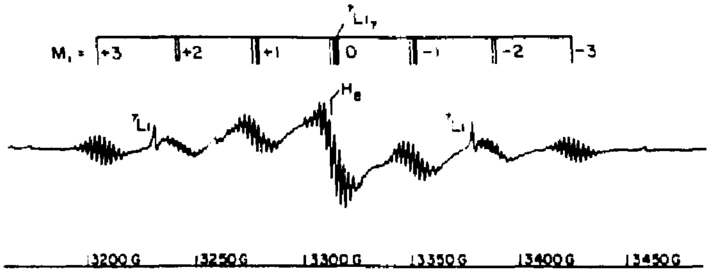

FIG. 1. ESR spectrum of $^7\mathrm{Li}_7$ in an argon matrix at 4.2 K. M_1 is the nuclear spin projection for two equivalent ^{7}Li nuclei. Also shown are $m = \pm 1/2$ for ^{7}Li. The resonance field for a free electron is $H_e = 3312.3(1)$ G. Isotopically enriched ^{7}Li was used.

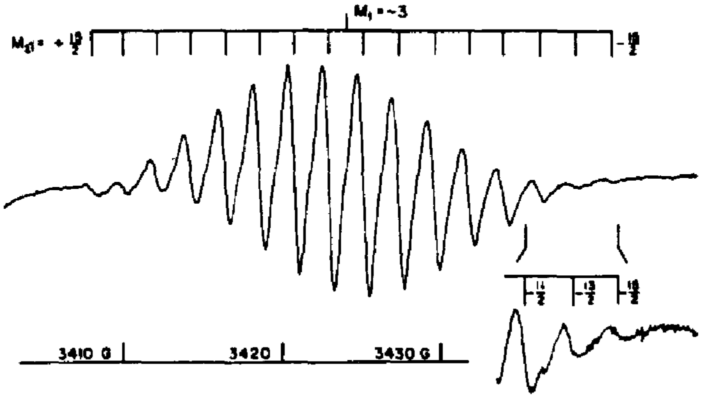

FIG. 2. Overview of the $M_1 = -3$ transitions of $^7Li_7$ in argon at 4.2 K. The overall spectrum and high field detail were obtained by signal averaging for 3 and 4 h, respectively. Isotopically enriched ^7Li was used.

shown in Table II are isotropic spin populations ρ_1 and ρ_2, obtained by dividing a_1 and a_2 by the hf splitting constant of the gas-phase atom.[26] Because of their large magnitude, both a_1 and ρ_1 may be assumed positive. However, the ESR spectra do not determine the sign of the much smaller a_2 constant.

Experiments using isotopically enriched ^6Li gave ESR spectra with a quintet hf pattern ($M_1 = +2, +1, 0, -1, -2$) characteristic of two equivalent $I = 1$ nuclei and a shf structure of up to 11 first derivative transitions ($M_2 = +5, \ldots, -5$) which implies a second set of five equivalent nuclei. The ESR spectrum of $^6Li_7$ is shown in Fig. 1 of Ref. 18. Before photolysis, however, the septemer spectrum was 3–4 times more intense than shown in this figure. As in the case of $^7Li_7$, the ESR spectra do not completely rule out a cluster larger than the septemer. For several M_1 components, the relatively weak transitions in the region $M_2 = \pm 5$ are obscured by overlap with features arising from the other carriers noted above. In cases where this overlap is apparently absent, the spectral resolution is poor. Thus the shf splitting for $^6Li_7$ is $a_2 \sim 0.8$ G, comparable in magnitude to the linewidths of these transitions $\Delta H_{pp} \sim 0.4$ G. Since relative intensities fall off rapidly at large M_2, the outer transitions are not fully resolved and any hypothetical $M_2 = \pm 6$ transition would be difficult to detect even with the quite good S/N ratio realized in these experiments. Although incomplete resolution makes relative intensity measurements less reliable than those discussed for $^7Li_7$, these data are most consistent with the presence of a seven atom cluster.

TABLE I. Comparison of measured (matrix site I) and calculated transition fields, $H(J_1, M_1)$ defined in Eq. (1), for $^7Li_7$ in argon at 4.2 K. Experimental $\langle a_2 \rangle$ are average shf constants for individual (J_1, M_1). Units are Gauss.

		$H(J_1,M_1)$			$\langle a_2 \rangle$
M_1	J_1	Meas.	Calc.		$\pm \leq 0.01$
+3	3	3205.4	3205.6	−0.2	2.19
+2	2	3242.3	3242.2	+0.1	2.19
	3	3241.1	3241.0	+0.1	2.19
+1	1	3279.0	3278.8	+0.2	2.18
	2	3278.1	3278.0	+0.1	2.19
	3	3276.9	3276.8	+0.1	2.18
0	0	3315.4	3315.4	0.0	2.22
	1	3315.2	3315.0	+0.2	2.22
	2	3314.2	3314.2	+0.1	2.20
	3	3313.0	3313.0	0.0	2.22
−1	1	3351.9	3351.6	+0.3	2.18
	2	3350.9	3350.8	+0.1	2.18
	3	3349.7	3349.6	+0.1	2.18
−2	2	3387.9	3387.8	+0.1	2.18
	3	3386.8	3386.6	+0.2	2.18
−3	3	3423.6	3424.0	−0.4	2.16

Table II gives the best fit parameters g_0, a_1, and a_2 for $^6Li_7$. Because of the small value of a_2, the splitting between transitions having the same M_1 quantum number but a different J_1 was not resolved. However, a small average shift was deduced from the last term of Eq. 1 and is included in the g value given in Table II. The small (approximately 0.7 G) discrepency between the g values for $^6Li_7$ and $^7Li_7$ probably arises from the calibration uncertainties noted earlier. The ratios of experimental hf constants, $^7a_1/^6a_1 = 2.641(3)$ and $^7a_2/^6a_2 = 2.639(15)$ are in excellent agreement with the ratio of nuclear g factors $g_7/g_6 = 2.641$.[27]

B. Temperature dependence

Both $^6Li_7$ and $^7Li_7$ occur in multiple trapping sites whose line positions show a small, but noticeable, shift with temperature. Figure 3 contrasts the ESR spectra of the

TABLE II. Magnetic parameters for atomic lithium and lithium septemers (matrix site I) in argon at 4.2 K. Estimated errors (see the text) are in parentheses. Units of a_1, a_2 are Gauss.

	g_0	a_1	$\pm a_2$	ρ_1[a]	$\pm \rho_2$[a]
^6Li	2.000 11(1)	56.06(7)		1.03	
$^6Li_7$	2.000 13(2)	13.78(3)	0.83(1)	0.254	0.015
^7Li	2.000 19(2)	147.96(9)		1.03	
$^7Li_7$	2.000 45(6)	36.39(5)	2.19(2)	0.254	0.015

[a] Isotropic spin populations ρ_1 and ρ_2 are ratios of a_1 and a_2 to hf constant of free atom $a(^6Li) = 54.29$ G and $a(^7Li) = 143.36$ G from Ref. 26.

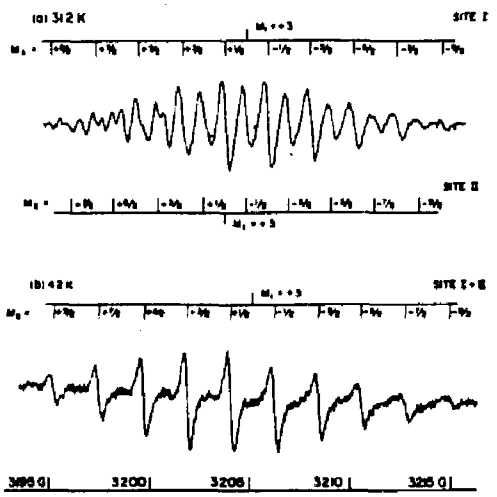

FIG. 3. Comparison of the $M_I = +3$ transitions for $^7Li_7$ in argon at (a) 31.2 K (b) 4.2 K. Roman numerals denote principal matrix sites.

$M_I = +3$ transitions for $^7Li_7$ in argon at $T = 31.2$ and 4.2 K. At higher temperatures [Fig. 3(a)] the two dominant matrix sites (labeled I and II) are well resolved, but, as shown in Fig. 3(b), there is a near complete overlap of these features at 4.2 K.

Figure 4 shows the measured temperature dependence of the *relative* origins ($H_I - H_{II}$) of the $M_I = +3$ transitions for matrix sites I and II. Although the *absolute* field position (H_I or H_{II}) changes by no more than 0.02 G K^{-1}, relative values are quite well determined since calibration uncertainties tend to cancel. A similar, but less complete, analysis was made for both $J = 2$ and 3 of $M_I = \pm 2$. The same behavior was observed for all M_I components, but spectral congestion in the $M_I = 0, \pm 1$ regions precludes a reliable analysis. Because of its relatively small hf constant, an analogous difficulty pertains to $^6Li_7$.

The results shown in Fig. 4 suggest that $H_I - H_{II}$ varies linearly with temperature in the range $10 \lesssim T \lesssim 35$ K.[28] These trends may be attributed to a small temperature dependence in the a_1 constant and g value for the two matrix sites of $^7Li_7$.[29] From Eq. (1) (ignoring the second order correction term) and the data of Fig. 4, a reasonably accurate estimate can be made for the temperature dependence in the *relative* Zeeman and hf interactions of the two matrix sites $\Delta H_0 = H_0(\mathrm{I}) - H_0(\mathrm{II})$, where $H_0 = g_e H_e / g_0$ and $\Delta a_1 = a_1(\mathrm{I}) - a_1(\mathrm{II})$, respectively. In units of Gauss, this analysis gives (estimated errors in parentheses)

$$\Delta H_0 = 0.172(34) - 0.0022(15)T$$

and (3)

$$\Delta a_1 = -0.640(11) + 0.0097(5)T.$$

Although these results pertain to measurements made on $M_I = \pm 3$, they predict quite well the observed temperature behavior of $H_I - H_{II}$ for $M_I = \pm 2$.

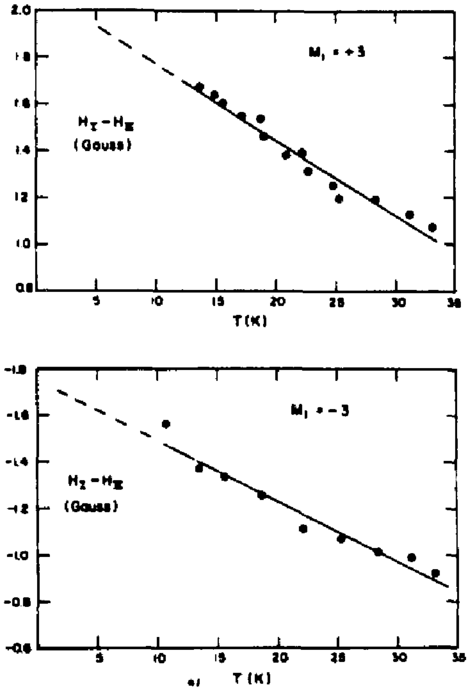

FIG. 4. Temperature dependence in relative origins ($H_I - H_{II}$) of $M_I = \pm 3$ transitions for matrix sites I and II of $^7Li_7$ in argon.

Temperature dependent hf constants have been reported for transition metal ions,[30–32] color centers,[33] and small organic[34–36] and inorganic[37–40] radicals isolated in a variety of solid hosts. The origin of these phenomena has been attributed to (1) the direct expansion of the surrounding lattice,[30] (2) a modulation of the hf constant by a *single*, lattice, or radical, vibration,[32,33] and (3) the coupling of the radical to the *continuous* phonon spectrum of the host via the orbit-lattice interaction.[30–31] In several instances it has been possible to distinguish between the last two mechanisms by measuring the functional form for the temperature dependence of the radical hf constant.[35–40] A similar analysis for $^7Li_7$ in argon is less straightforward since (1) our data pertain to the change in the relative hf constants for two matrix sites and (2) the temperature range over which measurements can be made is relatively restricted. Thus, although low frequency modes might be expected to be important for a radical such as Li_7, we are unable at present to assign a particular mechanism for the observed temperature dependence.[41]

IV. DISCUSSION

The ESR spectra reveal a distinctive symmetry for the wave function of the unpaired electron. Spin population resides on two sets of completely equivalent ^6Li or ^7Li nuclei: one set composed of two nuclei plus a second set of (most likely) five equivalent nuclei. The isotropic spin population on the two equivalent nuclei ($\rho_1 \sim +25\%$) is large, whereas that on the remaining five nuclei ($\rho_2 \sim \pm 1.5\%$) is much smaller. This distribution is qualitatively identical to that observed for matrix isolated Na_7 and K_7.[1] In Ref. 3 it was inferred from extensive simple Hückel calculations that a pentagonal bipyramidal geometry (point group D_{5h}) was most likely for the sodium and potassium septemer. Consequently, a similar structure would be expected for Li_7. The simple Hückel calculations predict an electron configuration—$a_1'^2 e_1'^4 a_2''$ giving rise to a ${}^2A_2''$ ground state for which $\rho_1 = 50\%$ on each of the two apical atoms and $\rho_2 = 0$ on the five ring atoms. It was further argued that any realistic calculation, including both a more extensive basis set (s and p orbitals) and spin polarization effects, should give rise to (1) *isotropic* spin populations $\rho_1 < 50\%$ and (2) a small spin density at each of the ring nuclei.[3] A pentagonal bipyramidal geometry would, therefore, have an ESR spectrum in close correspondence to that observed for Li_7, Na_7, and K_7.

In contrast to the situation for $M_3 \sim M_6$, there have been few *ab initio* calculations on alkali septemer molecules.[42,43] A notable exception is the recent study by Fantucci *et al.*,[4] which predicts a particular stability for pentagonal bipyramidal clusters. Employing MRD CI methods,[44] all electron for Li_7 but with a pseudopotential approximation for Na_7 and K_7, the authors of Ref. 4 find a ground state configuration—$a_1'^2 e_1'^4 a_2''$ with $\rho_1 \sim 35\%$ for Li_7 and $\rho_1 \sim 45\%$ for Na_7 and K_7. The remaining spin population is predicted to reside in valence p orbitals and is largely concentrated on the ring atoms, as might be expected for an orbital of a_2'' symmetry.

Since even a relative large admixture of p character will have only a minor influence on the ESR spectra,[18] our results do not give a direct measurement of anisotropic spin populations. However, as in the case of all previously studied M_3[1,2,18,45] and M_7[3] clusters, the total isotropic spin population for Li_7 does not sum to unity and this deficit provides a measure of the average degree of hybridization in the cluster. While no calculation to date has predicted either the magnitude or sign of ρ_2, the analogous parameter for Na_3 and K_3 is negative and spin polarization effects might also be expected to induce a negative spin density on the ring atoms of M_7.[46] Thus, the total isotropic spin population for the lithium septemer (ξ_7) is $2\rho_1 + 5\rho_2 = 0.43$, implying a p character of nearly 60%. Table III, an expanded version of Table II in Ref. 18, compares ξ_7 for Li_7, Na_7, and K_7. Also given in Table III are total isotropic spin populations for the atom (ξ_1, constrained to be unity) and the trimer (ξ_3). As explained in more detail in Ref. 18, ξ_2 and ξ_∞ are the fractional s character for, respectively, an electron in the valence σ orbital of the dimer and an electron at the Fermi surface of the bulk metal. Viewed as a whole, the data of Table III reveal several interesting trends in the chemical bonding of the alkali metal clusters. Thus, for a given size, the s character of the "Fermi electron" in sodium is almost identical to that of potassium, but the corresponding lithium cluster always has a much greater proportion of p character. For all three metals there is a monotonic decrease in s character with increasing cluster size and this culminates in a close approach to the bulk hybridization for the three-dimensional alkali septemer molecules.

TABLE III. Average s character for the "Fermi electron" of alkali metal clusters in argon matrices.

	ξ_1	ξ_2^{a}	ξ_3^{b}	ξ_7^{c}	ξ_∞^{d}
Li	1.00	0.86	0.68	0.43	0.42(2)
Na	1.00	0.93	0.87	0.64	0.66(4)
K	1.00	0.94	0.87	0.63	0.66(4)

[a] From: L. Pauling, Proc. R. Soc. London Ser. A 196, 343 (1949).

[b] Li, Ref. 18; Na, Refs. 1 and 45; K, Ref. 2.

[c] Li_7, this work; Na_7 and K_7, Ref. 3. ξ_7 assumes $\rho_2 < 0$ (see the text).

[d] Bulk metal, see Ref. 18.

ACKNOWLEDGMENTS

This research was supported in part by the City University of New York Faculty Research Award Program and by The National Science Foundation under Grant CHE 83-07164.

---

[1] D. M. Lindsay, D. R. Herschbach, and A. L. Kwiram, Mol. Phys. 32, 1199 (1976).

[2] G. A. Thompson and D. M. Lindsay, J. Chem. Phys. 74, 959 (1981).

[3] G. A. Thompson, F. Tischler, and D. M. Lindsay, J. Chem. Phys. 78, 5946 (1983).

[4] P. Fantucci, J. Koutecky, and G. Pacchioni, J. Chem. Phys. 80, 325 (1984).

[5] M. R. Hoare and P. Pal, Nature Phys. Sci. 230, 5 (1971); 236, 35 (1972).

[6] M. R. Hoare and P. Pal, Adv. Phys. 20, 161 (1971).

[7] M. R. Hoare, Adv. Chem. Phys. 40, 49 (1979).

[8] S. Ino, J. Phys. Soc. Jpn. 21, 346 (1966).

[9] K. Kimoto and I. Nishiyda, J. Phys. Soc. Jpn. 22, 940 (1967).

[10] J. G. Allpress and T. V. Sanders, Surf. Sci. 7, 1 (1967).

[11] J. Farges, B. Raoult, and G. Torchet, J. Chem. Phys. 59, 3454 (1973).

[12] J. Farges, M. F. de Feraudy, B. Raoult, and G. Torchet, J. Chem. Phys. 78, 5067 (1983).

[13] O. Echt, K. Sattler, and E. Recknagel, Phys. Rev. Lett. 47, 1121 (1981).

[14] J. Muhlbach, K. Sattler, P. Pfau, and E. Recknagel, Phys. Lett. A 87, 415 (1982).

[15] M. M. Kappes, R. W. Kunz, and E. Schumacher, Chem. Phys. Lett. 91, 413 (1982).

[16] L. B. Knight, Jr., R. W. Woodward, R. J. Van Zee, and W. Weltner, Jr., J. Chem. Phys. 79, 5820 (1983).

[17] C. K. Jen, V. A. Bowers, E. L. Cochran, and S. N. Foner, Phys. Rev. 126, 1749 (1962).

[18] D. A. Garland and D. M. Lindsay, J. Chem. Phys. 74, 959 (1983).

[19] W. Weltner, Jr., *Magnetic Atoms and Molecules* (Van Nostrand, New York, 1983).

[20] N. M. Atherton, *Electron Spin Resonance* (Wiley, New York, 1973).

[21] A bound on the possible inequivalency of these nuclei may be estimated from the ESR linewidth, approximately 0.3 G. If for example, four nuclei are equivalent and distinct from the fifth, then the hf constants of these two groups can differ by no more than ~5%.

[22] A linewidth of this magnitude might result from molecular tumbling. It was also observed that the optimum phase angle of the lock-in amplifier was not the same for both Li_7 and atomic lithium. This phenomenon is often indicative of motional effects. See, for example: C. P. Poole, Jr., *Electron Spin Resonance* (Wiley, New York, 1983).

[23] For a nine atom cluster having seven equivalent $I = 3/2$ nuclei, then, $M_I = +21/2, \ldots, -21/2$. The relative intensities of $M_I = \pm 15/2$ and $M_I = \pm 17/2$ are expected to be 3:1.

[24] Owing to instabilities in the JEOL field scan circuitry, acquisition times much longer than 4 h were impractical.

[25] Except in the case of $M_I = \pm 15/2$ where there is an obvious intensity perturbation at low fields.

[26] P. Kusch and V. W. Hughes, *Handbuch der Physik*, edited by S. Flugge

(Springer, Berlin, 1959).

[27] E. R. Andrew, *Nuclear Magnetic Resonance* (Cambridge University, London, 1955), Appendix I.

[28] The accuracy of these measurements does not preclude higher order terms, however.

[29] Any temperature dependence in the a_2 constant is too small to be observed.

[30] W. M. Walsh, J. Jeener, and N. Bloembergen, Phys. Rev. A 139, 1338 (1965).

[31] E. Simanek and R. Orbach, Phys. Rev. 145, 191 (1966).

[32] K. Zdansky, Phys. Status Solidi 28, 181 (1968).

[33] W. Dreybrodt, Phys. Status Solidi 21, 99 (1967); W. Assmus and W. Dreybrodt, *ibid.* 34, 183 (1969).

[34] P. J. Krusic and P. Meakin, J. Am. Chem. Soc. 98, 228 (1976); D. Griller, K. U. Ingold, P. J. Krusic, and H. Fischer, *ibid.* 100, 6750 (1978).

[35] D. Griller, P. R. Marriott, and K. F. Preston, J. Chem. Phys. 71, 3703 (1979).

[36] D. Griller and K. F. Preston, J. Am. Chem. Soc. 101, 1975 (1979).

[37] A. R. Boate, J. R. Morton, and K. F. Preston, J. Magn. Reson. 29, 243 (1978).

[38] A. R. Boate, J. R. Morton, K. F. Preston, and S. J. Strach, J. Chem. Phys. 71, 388 (1970).

[39] J. R. Morton, K. F. Preston, and S. J. Strach, J. Phys. Chem. 83, 2628 (1979).

[40] J. R. Morton, K. F. Preston, and S. J. Strach, J. Phys. Chem. 84, 2478 (1980).

[41] Nevertheless, the data do show that the a_1 constant for matrix site I increases by about 1/2% as the temperature is raised from 4.2 to 31.2 K. This change is of the same order of magnitude (but opposite in sign) to that expected from the approximately 0.02 Å increase in the lattice constant of solid argon [G. L. Pollack, Rev. Mod. Phys. 36, 748 (1964)], if the interaction between $^7Li_7$ and its argon cage is assumed comparable to that of atomic lithium in argon. Thus, Jen *et al.* (Ref. 17) attribute the hf constants $a = 147.8$ G and $a = 141.1$ G for the two-matrix sites of ^7Li in argon to trapping sites for which the argon–lithium distances are 3.95 and 4.14 Å, respectively. Accordingly, an increase in the argon–lattice distance of 0.02 Å corresponds to an approximately 1/2% decrease in the atomic hf coupling constant.

[42] J. Flad, H. Stoll, and H. Preuss, J. Chem. Phys. 71, 3042 (1979).

[43] G. Pacchioni, D. Plavsic, and J. Koutecky, Ber. Bunsenges. Phys. Chem. 87, 503 (1983).

[44] Multireference diexcited configuration interaction.

[45] D. M. Lindsay and G. A. Thompson, J. Chem. Phys. 77, 1114 (1982).

[46] Both the simple Hückel (Ref. 3) and *ab initio* (Ref. 4) calculations predict a ground state configuration—$a_1'^2 e_1'^4 a_2''$. The unpaired electron resides in an a_2'' molecular orbital giving rise to a large α spin population on the two apical atoms and a nodal plane through the ring atoms. The doubly occupied a_1' orbital has nonvanishing coefficients for both the apical and the ring atoms with, to a first approximation, equal α and β spin distributions. The exchange interaction will favor different spatial functions for the α

Appendix A.2 Reprint : J. Chem. Phys. 78, 2813 (1983).

ESR of pseudorotating $^6Li_3$ and $^7Li_3$

D. A. Garland and D. M. Lindsay

Department of Chemistry, City University of New York, The City College, New York, New York 10031

(Received 16 November 1982; accepted 15 December 1982)

ESR spectra assigned to pseudorotating $^6Li_3$ and $^7Li_3$ molecules have been produced by arc lamp photolysis of argon matrices doped with isotopically enriched ^{6}Li or ^{7}Li. The spectrum of $^6Li_3$ consists of seven equally spaced first derivative transitions with relative intensities in good agreement with the expected values for three equivalent $I = 1$ nuclei. The measured hf constant and g value are $\bar{a} = 12.21(1)$ G and $g_i = 2.002\,82(1)$. The absence of a stationary trimer spectrum suggests that the ground vibronic state of Li_3 is relatively nonlocalized. The average isotropic spin population of the trimer $\bar{\rho} = 0.225$ is in excellent agreement with the predictions of *ab initio* calculations. The total isotropic spin population $3\bar{\rho} \simeq 0.68$ suggests an approximately 30% p-character for the unpaired electron wave function. A comparison of the orbital composition of M, M_2, M_3, M_4 (M = Li, Na, K) shows (i) a diminishing s-character with increasing cluster size, (ii) a remarkable similarity between Na and K for all cluster sizes, and (iii) a smaller s-character (greater hybridization) for Li clusters.

I. INTRODUCTION

As a consequence of the Jahn–Teller theorem, the equilateral triangle (point group D_{3h}) is not a stable geometry for the ground electronic state of an alkali trimer molecule. The orbitally degenerate $^2E'$ state (equal spin populations on all atoms) will be split into a $^2A_1$ and $^2B_2$ state by a distortion to C_{2v} symmetry. Both electron spin resonance (ESR) spectra of matrix isolated Na_3[1,2] and K_3[3,4] and *ab initio* calculations on Li_3[5] and Na_3[6] show that the $^2B_2$ partner (apical angle > 60°) lies lowest in energy. This gives rise to a nondegenerate ground state and an unequal spin distribution for the trimer. As revealed by the ESR spectra,[1-4] the spin population on the two base atoms (ρ_2 on each) is large and positive while that of the third atom (ρ_1) is small and, for Na_3 and K_3, negative.

The distortion of an equilateral trimer takes place through appropriate[1,2,5] linear combinations of the degenerate e' vibrational mode and produces *three* equivalent potential energy wells, each with a $^2B_2$ electronic symmetry. The three minima are separated from their neighbors by an energy barrier and if this is sufficiently large they will support localized nuclear wave functions. For a realistic potential,[5,6] however, the vibrational wave functions of adjacent minima overlap and the trimer is again doubly degenerate. For this situation, the ground state is a *vibronic* ($E' \times e'$) doublet with symmetry $^2E'$.

On the ESR time scale, the trimer might either appear trapped in the three "stationary" $^2B_2$ configurations or it might exchange ("pseudorotate") by, for instance, tunneling between adjacent wells. In the latter case the three alkali atoms become, on average, equivalent. For matrix isolated Na_3 and K_3 both stationary and pseudorotating spectra are observed.[1-4] If the ground vibronic state is very close to, or even above, the barrier to pseudorotation, then there exists the possibility of a fluxional molecule which can never be described as localized in a particular geometry.

In this paper we report on the ESR spectra of pseudorotating $^6Li_3$ and $^7Li_3$ in argon matrices. Since, despite a careful search, no stationary spectra were observed this suggests that the lithium trimer corresponds more closely to a completely fluxional molecule than do either Na_3 or K_3. This trend is consistent with the *ab initio* calculations which predict a pseudorotation barrier of approximately 100 cm^{-1} for Na_3,[6] but shallow minima, insufficiently deep to support a vibrational level, for Li_3.[5] The ESR spectra of $^6Li_3$ show a pattern of seven equally spaced hyperfine (hf) transitions with relative intensities close to the expected values for three equivalent $I = 1$ nuclei. The average isotropic spin population $\bar{\rho} = 0.225$ on each atom is significantly smaller than the corresponding parameter for Na_3 or K_3. This result is interpreted in terms of a larger s-p hybridization in the lithium trimer. The orbital character of Li_3, Na_3, and K_3 is reviewed in the context of the bonding in the alkali dimer molecules and the bulk metal phase.

II. EXPERIMENTAL

Lithium clusters were formed by co-depositing atomic lithium, either naturally occurring (Alfa, 99.9%) or isotopically enriched (Oak Ridge National Laboratory, 98% ^{6}Li and 99.9% ^{7}Li) with excess argon (Airco, 99.9998%) on a sapphire plate bonded to the inside of a TE_{102} X-band ESR cavity. The cavity was attached to a variable temperature cryostat, whose construction has been described elsewhere.[1,3] Lithium was evaporated at approximately 465 °C from a water shielded Knudsen effusion source recently modified to include a sliding quartz microbalance (Veeco, QM-301). For the results presented here, the Ar:Li ratio was 75:1 with 0.1 μmol/h of lithium incident on the sapphire plate and a total deposition time of 7 h. Matrices were grown at or slightly above 4.2 K, subsequently annealed by warming to 31 K and then photolyzed for up to 4 h at 30 K with a 150 W Xe arc lamp (Schoeffel, LPS 251). Matrix temperatures were measured with a calibrated carbon resistor and are accurate to ±5%.

Spectra were recorded on a JEOL ME-3X ESR spectrometer (microwave power incident on cavity ~0.5 mW) using 100 kHz magnetic field modulation (peak-to-peak amplitude 0.25 G) and phase sensitive detection. The

0021-9606/83/062813-04$02.10

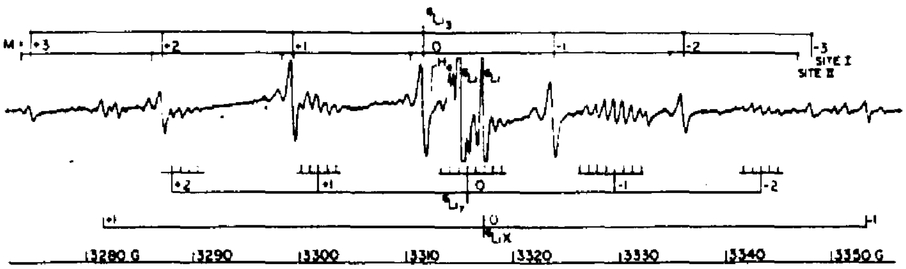

FIG. 1. ESR spectrum of pseudorotating ^{6}Li$_3$ in an argon matrix at 28.5 K. Roman numerals designate matrix sites. Also shown are atomic lithium, ^{6}Li$_7$ and a radical designated ^{6}LiX (see the text). He = 3312.27 G is the resonance field of a free electron at a cavity frequency of 9.282 55 GHz.

microwave bridge of the spectrometer was modified to include a three port circulator (*E&M, X104 LT*) and directional coupler. Scan times for the spectra presented here were 25 min with a time constant of 0.5 s. The resonance frequency of the cavity plus sapphire plate and matrix sample was measured with a microwave frequency counter (HP 5243L plus HP 5255A plug in). Individual spectra were calibrated with a proton magnetometer (Micronow, model 515). Relative and absolute magnetic field positions are judged accurate to 0.5% and ±1 G, respectively.

III. SPECTRA AND ANALYSIS

Figure 1 shows the ESR spectrum observed when argon matrices doped with isotopically enriched ^{6}Li were annealed to approximately 30 K and then photolyzed for 4 h. Several spectra are assigned: atomic lithium, the pseudorotating trimer, the lithium septemer, and a radical designated ^{6}LiX. Trimer features were entirely absent prior to photolysis. The trimer spectrum grew monotonically with photolysis time, while the intensities of the remaining radicals (present both before and after photolysis) decreased. Trimer spectra were observed in several experimental runs, but relative and absolute yields were rather unpredictable. When photolyzed matrices were warmed above ca. 32 K, the trimer intensity was suddenly and irreversibly halved while that of ^{6}Li$_7$ increased approximately threefold. Septemer intensities remained relatively constant up to ca. 38 K. The trimer linewidth increases monotonically and reversibly with decreasing temperature. Unlike matrix isolated Na$_3$ and K$_3$,[3,4] the spectra of Li$_3$ show no evidence of an alternating linewidth effect in the range of 30–3 K. Since the atomic spectra also broaden with decrease in temperature, this suggests that saturation, and not the exchange mechanism postulated for Na$_3$ and K$_3$,[3,4] may be responsible for the linewidth behavior of Li$_3$. Except possibly as a transient during annealing,[7] no stationary trimer spectra were observed despite a careful search at several temperatures between 4.2 and 30 K. Both the optimum conditions for trimer formation and its subsequent temperature behavior will be studied in future experiments.

The spectrum assigned to pseudorotating ^{6}Li$_3$ (Fig. 1) consists of seven equally spaced hf transitions with *measured intensities (in the ratio* 1.1 : 3.3 : 6.2 : 7.0 : 5.7 : 3.0 : 1.1) in good agreement with the expected values (1 : 3 : 6 : 7 : 6 : 3 : 1) for three equivalent $I = 1$ nuclei. Experimental transition fields were fit to the high field *expression*,[1-4]

$$H(M) = g_e/g_0 \cdot H_e - g_e/g_0 \cdot \bar{a} M , \qquad (1)$$

where g_e, H_e are the g value and resonance field for a *free electron* and $M = +3, \ldots, -3$ is the projection of the total nuclear spin angular momentum of the three $I = 1$ nuclei. In Eq. (1), g_0 is an isotropic g value and $\bar{a}$ is the average hf splitting constant for the pseudorotating trimer. Table I gives g_0 and $\bar{a}$ obtained by a least-squares fit of the experimental data to Eq. (1). Error limits (in parentheses) represent one standard deviation uncertainty in this fit. However, the estimated calibration errors noted earlier $\pm\frac{1}{2}$% and ±1 G in, respectively, the relative and absolute magnetic field, are much larger. A second matrix site for the trimer (see Fig. 1) has $g_0 = 2.003\,54(2)$ with $\bar{a} = 12.12(1)$ G.

Photolysis of argon matrices containing isotopically enriched ^{7}Li gave rise to a ten line ESR spectrum (with two components obscured) as would be expected[2-4] for three equivalent $I = \frac{3}{2}$ nuclei. Table I gives the experimental g value and hf constant for pseudorotating ^{7}Li$_3$. A small, averaged[4] second order correction, not in-

TABLE I. Magnetic parameters for atomic lithium and pseudorotating ^{6}Li$_3$, ^{7}Li$_3$ in argon matrices. Experimental uncertainties (see the text) are given in parentheses. Units of $\bar{a}$ are Gauss.

	g_0	$\bar{a}$	$\bar{\rho}$[a]
^{6}Li	2.000 11(1)	56.06(7)	1.03
^{7}Li	2.000 19(2)	147.96(9)	1.03
^{6}Li$_3$	2.002 82(1)	12.21(1)	0.225
^{7}Li$_3$	2.002 62(2)	32.19(9)	0.225

[a] Average isotropic spin population $\bar{\rho} = \bar{a}/a$(Li) where a(^{6}Li) = 54.29 G, a(^{7}Li) = 143.36 G are gas-phase hf constants from Ref. 10.

cluded in Eq. (1), was applied to each hf component. The small discrepancy between the g values for ^{6}Li$_3$ and ^{7}Li$_3$ probably arises from a combination of calibration errors and unresolved second order splittings. However, the ratio of experimental hf constants $^7\bar{a}/^6\bar{a} = 2.636 \pm 0.009$ is in excellent agreement with that predicted from the ratio of nuclear g factors $g_7/g_6 = 2.6410$.[9] Table I also gives isotropic spin populations $\bar{\rho} = \bar{a}/a$(Li) where a(Li) is the atomic isotropic hf constant of the gas-phase atom.[10]

Also shown in Fig. 1 is the central hf component of atomic lithium[11] (in two matrix sites) and a more complicated spectrum tentatively identified as the septemer ^{6}Li$_7$. The latter shows a principal hf splitting ($a_1 = 13.9$ G) into five groups of transitions as would be expected for *two* equivalent $I = 1$ nuclei. Each group consists of at least eleven equally spaced components (hf splitting, $a_2 = 0.8$ G), which indicates a further *five* equivalent nuclei. An analogous spectrum is observed for ^{7}Li in argon and both spectra will be the subject of a separate article.[12] For comparison purposes, Table I includes the experimental (to second order in a/H) g value and hf constant (one standard deviation uncertainty in parentheses) for atomic ^{6}Li and ^{7}Li in an argon matrix.

A fourth ESR spectrum, designated ^{6}LiX in Fig. 1, most probably arises from adduct formation between a single ^{6}Li atom and an impurity species X. The propensity for lithium atoms to form weakly bound complexes has been demonstrated both experimentally[13] and computationally.[14] The spectrum consists of three groups of transitions labeled $m = 0, \pm 1$ with, in Fig. 1, the central ($m = 0$) group entirely obscured by the stronger features of ^{6}Li and ^{6}Li$_7$. Since the components within each group are not equally spaced, this splitting is assumed to arise from matrix site effects with, possibly, a small hf interaction arising from the species X. For some spectra $m = 0$ transitions were observed and for these measured line positions give an excellent fit to the spin Hamiltonian for a radical containing a single ^{6}Li nucleus. For example, the hf constant and g value of the three transitions identified in Fig. 1 are (to second order in a/H) $^6a = 35.9(1)$ G with $g_0 = 1.9989(1)$. Scaling by $g_7/g_6 = 2.6410$,[9] the predicted[15] hf constant for an adduct ^{7}LiX is 95.0(3) G. Both this value and $g_0 = 1.9989(1)$ are close to, but not within experimental error of, the corresponding parameters[13] for ^{7}LiH$_2$O.

IV. DISCUSSION

A previous comparison[5] of ESR spin populations with those derived from *ab initio* calculations pointed out the approximately quantitative agreement between the measured[1] and calculated[6] values for Na$_3$. It was also noted that the experimental data for Na$_3$ were qualitatively similar to those predicted[5,16,17] for the $^2B_2$ state of Li$_3$. The present measurements show that this similarity is also quantitative. Thus the average spin population on the trimer $\bar{\rho} = 0.225$ from Table I is in near exact[18] agreement with the corresponding *ab initio* values $\bar{\rho} = \frac{1}{3}(2\rho_0 + \rho_3) = 0.24$[5,16] and 0.20.[16,17]

Since neither experiment nor theory gives a total *isotropic* spin population ($3\bar{\rho}$) close to unity, this suggests[1,5,18] a bonding participation by the valence $2p$ orbitals of lithium. The experimental result for Li$_3$ is $3\bar{\rho} = 0.68$, which implies a total p character of approximately 30%.[16,18] A similar deficit has been noted for Na$_3$[1] and K$_3$,[3] but for these molecules the p character is significantly less than 30%. This comparison is made in Table II, where $\xi_3 = 3\bar{\rho}$ is the average s character for the unpaired electron in the trimer.

TABLE II. Orbital composition (average s character) for the "Fermi electron" of alkali atom clusters M_n.

	ξ_1	ξ_2[a]	ξ_3[b]	ξ_∞[c]
Li	1.00	0.86	0.68	0.42(2)
Na	1.00	0.93	0.87	0.66(4)
K	1.00	0.94	0.89	0.66(4)

[a] ξ_2 = 1-fractional p character, from Ref. 20.

[b] Total isotropic spin populations, $\xi_3 = 3\bar{\rho}$. Li, this work; Na, Refs. 1 and 2; K, Refs. 3 and 4.

[c] Bulk metal, see the text.

Table II also gives the valence s character for the atom (ξ_1, constrained to be unity) and analogous quantities for the dimer (ξ_2) and bulk metal (ξ_∞). The dimer values ξ_2 = 1-fractional p character derive from semiempirical arguments made by Pauling[20] and represent the s character of an electron in the doubly occupied valence σ orbital of ground state Li$_2$, Na$_2$, or K$_2$. The bulk metal parameter is[21,22]

$$\xi_\infty = |\psi_F(0)|^2/|\psi_A(0)|^2 , \tag{2}$$

where $|\psi_F(0)|^2$ is the square of the wave function at the nucleus for an electron on the Fermi surface of the metal and $|\psi_A(0)|^2$, directly related to the atomic hf constant,[10] is the corresponding entity for the free atom. The probability density for the bulk metal was derived from,[21,23]

$$|\psi_F(0)|^2 = 1.277 \times 10^{23} \frac{KT_F}{\chi_p/\chi_0} \text{ cm}^{-3} , \tag{3}$$

where K is the experimental Knight shift for Li, Na, or K and T_F is the Fermi temperature.[23] The denominator of Eq. (3) is the ratio of the Pauli spin susceptibility of the metal (χ_p) to the paramagnetic susceptibility of a Fermi gas of conduction electrons (χ_0). The ratios assumed, $\chi_p/\chi_0 = 2.8(1)$, 1.6(1), and 1.7(1) for ^{7}Li, ^{23}Na, and ^{39}K, respectively, are an average of several tabulated values.[24] The assigned uncertainty, approximately representative of the spread in the tabulated χ_p/χ_0 was used to establish a rough error in the values of ξ_∞ derived from Eq. (2). The ξ_∞ given in Table II show that Na and K have a very similar s character, but the hybridization in Li is greater. A similar trend has been noted by Pauling,[20] but his semiempirical s character is consistently larger than the values derived from Eq. (2).

The data collected in Table II are striking in that they suggest (i) a diminishing s character for the "Fermi electron" with increasing cluster size, (ii) a remarkable similarity between Na and K for all cluster sizes, and, (iii) a distinctly smaller *s* character for the Li clusters. Work in progress suggests that these features also pertain to Li_7, Na_7, and K_7.[12] The trend in orbital composition for Li, Na, and K does not follow the order of the $ns \to np$ promotion energy for these elements (1.85, 2.10, and 1.61 eV for Li, Na, and K, respectively)[25] and so must reflect the relative ease of overlap between adjacent *p* orbitals. This is, apparently, *most favorable* for the smaller Li atom. The inaccessibility of the 2*p* orbitals of atomic hydrogen is presumably at least partly responsible for the instability of ground state H_3.

ACKNOWLEDGMENTS

This research was supported in part by the City University of New York PSC-BHE research award program and by the National Science Foundation under grant number CHE 79-13260. We thank Professor John Lombardi for the use of the arc lamp and Professor Stewart Novick for the loan of a microwave frequency counter.

---

[1] D. M. Lindsay, D. R. Herschbach, and A. L. Kwiram, Mol. Phys. 32, 1199 (1976).

[2] D. M. Lindsay and G. A. Thompson, J. Chem. Phys. 77, 1114 (1982).

[3] G. A. Thompson and D. M. Lindsay, J. Chem. Phys. 74, 959 (1981).

[4] G. A. Thompson, F. Tischler, D. Garland, and D. M. Lindsay, Surf. Sci. 106, 408 (1981); D. M. Lindsay, D. Garland, F. Tischler, and G. A. Thompson, Am. Chem. Soc. Symp. Ser. 179, 69 (1982).

[5] W. H. Gerber and E. Schumacher, J. Chem. Phys. 69, 1692 (1978); E. Schumacher, W. H. Gerber, H. P. Harri, M. Hofmann, and E. Scholl, Am. Chem. Soc. Symp. Ser. 179, 83 (1982); W. H. Gerber, *Theorie des Dynamischen Jahn-Teller-Effekts in* Li_3, Ph.D. thesis, University of Bern, 1980. The last two references suggest that the potential surface for Li_3 is much flatter than originally predicted.

[6] R. L. Martin and E. R. Davidson, Mol. Phys. 36, 1713 (1978).

[7] In the structure expected (Refs. 1 and 3) for stationary Li_3, two nuclei are equivalent (hf constant $a_0 > 0$) and the third is distinct (hf constant $|a_3| \ll a_0$). The spectrum observed during annealing of ^{7}Li doped matrices, a partially obscured septet of quartets, has $a_0 = 46.1(2)$ G with $a_3 = +6.8(3)$ G and $g_0 = 2.0047(4)$. These parameters are in reasonable accord with the hf constant (Refs. 2 and 3), $\bar{a} = \frac{1}{3}(2a_0 + a_3)$, and g value of the stable, pseudorotating trimer provided $a_3 > 0$. A positive value for a_3 is predicted by *ab initio* calculations (Ref. 5), but is opposite in sign to the negative hf constant found (Refs. 2 and 4) for Na_3 and K_3.

[8] The second order shift is discussed in Ref. 2. For each of $M = +\frac{3}{2}, \ldots, -\frac{3}{2}$ an averaged shift was used. A further assumption was $\overline{a^2} \approx \bar{a}^2$ (notation of Ref. 2).

[9] E. R. Andrew, *Nuclear Magnetic Resonance* (Cambridge University, London, 1955), Appendix 2.

[10] P. Kusch and V. W. Hughes, *Handbuch der Physik*, edited by S. Flugge (Springer, Berlin, 1959).

[11] C. K. Jen, V. A. Bowers, E. L. Cochran, and S. N. Foner, Phys. Rev. 126, 1749 (1962).

[12] D. A. Garland and D. M. Lindsay (to be published). Qualitatively similar spectra have been observed for Na_7 and K_7; G. A. Thompson, F. Tischler, and D. M. Lindsay, J. Chem. Phys. (in press).

[13] P. F. Meier, R. H. Hauge, and J. L. Margrave, J. Am. Chem. Soc. 100, 2108 (1978).

[14] M. Trenary, H. F. Schaeffer, and P. Kollman, J. Am. Chem. Soc. 99, 3885 (1977); J. Chem. Phys. 68, 4047 (1978).

[15] The observed ^{7}LiX spectrum was very weak. In some experiments there was a much stronger spectrum consisting of an additional quartet of hf transitions with $g_0 = 1.9898(2)$ and $a = 131.3(3)$ G. A "g shift" of this magnitude might imply a spin state $S > \frac{1}{2}$.

[16] D. M. Lindsay, D. R. Herschbach, and A. L. Kwiram, Mol. Phys. 39, 529 (1980). The accompanying table contains a typographical error under the entry for Li_3(CEPA). The spin population for nucleus three of the $^2B_2$ state should read 0.02 and not 0.22 as shown.

[17] J. Kendrick, Mol. Phys. 35, 593 (1978).

[18] Spin populations derived by scaling the molecular hf constant by the corresponding atomic value may be in error due to matrix effects and to orbital contraction or expansion upon molecule formation. As shown by the atomic data in Table I, the former effect can contribute an error of several percent.

[19] Even a relatively large anisotropic spin population will have only a minor effect on the ESR spectra of Li_3. For example, a 10% admixture of 2*p* character on a ^{6}Li atom in the trimer will give rise to an anisotropic hf of approximately 0.04 G.

[20] L. Pauling, Proc. R. Soc. London Ser. A 196, 343 (1949).

[21] C. P. Slichter, *Principles of Magnetic Resonance* (Springer, Berlin, 1980).

[22] R. T. Schumacher, *Magnetic Resonance* (Benjamin, New York, 1970).

[23] C. Kittel, *Introduction to Solid State Physics* (Wiley, New York, 1976).

[24] L. Wilk, A. H. MacDonald, and S. H. Vosko, Can. J. Phys. 57, 1065 (1979); A. H. MacDonald, K. L. Liu, S. H. Vosko, and L. Wilk, *ibid.* 59, 500 (1981).

[25] C. E. Moore, *Atomic Energy Levels*, Natl. Bur. Stand. (U.S.) Circ. 467 (1952).

Appendix A.3 Reprint: **Am. Chem. Soc. Symp. Ser.** 179,
Chapter 7, 69 (1982).

7

ESR of Stationary and Pseudorotating Alkali Trimer Molecules

D. M. LINDSAY, DENISE GARLAND, FRANCES TISCHLER,
and G. A. THOMPSON

City University of New York, Department of Chemistry, City College,
New York, NY 10031

The relaxation theory of ESR linewidths is specialized to the case of pseudorotating K_3. Trimer molecules are assumed to fluctuate randomly between the three stable configurations which correspond to static Jahn-Teller distortions from D_{3h} symmetry. A simulated ESR spectrum is shown to be in quite good agreement with the linewidth alternation observed for K_3 in argon at low temperatures. Measured linewidths give approximate correlation and transverse relaxation times, 10^{-8} sec $\leq \tau_c \leq 10^{-10}$ sec and 10^{-8} sec $\leq T_2 \leq 10^{-6}$ sec, for the temperature range 4.2 K $\leq T \leq$ 20 K. The temperature dependence of τ_c is well represented by either exponential or power law behavior. Possible pseudorotation mechanisms, including a temperature dependent tunneling, are outlined.

Small metal clusters have received considerable attention because of their possible involvement as "active sites" in a variety of catalyzed reactions. Although not particularly noted for their catalytic activity, alkali clusters have a simple chemical composition and may, therefore, model the more complicated systems in a manner analogous to the role played by the hydrogen atom in atomic structure. Less emphasized is the fundamental nature of alkali clusters *per se*. Since the ground state of H_3 is not chemically bound, alkali trimers are the most elementary species which can exhibit a Jahn-Teller interaction.

In previous electron spin resonance (ESR) studies of matrix isolated Na_3 (1, 2) and K_3 (3, 4), alkali trimers have been shown to be chemically bound and well described both by simple bonding ideas (1, 3) and by the more sophisticated calculations recently employed for Li_3 (5), Na_3 (6) and K_3 (7). For the potassium trimer in argon, two distinct ESR spectra are observed (3). An obtuse angled isomer corresponds to one of three static Jahn-Teller distortions from D_{3h} symmetry, and is surprisingly similar to the structure reported for Na_3 (1). A "pseudorotating" isomer is both qualitatively and quantitatively consistent with fast exchange between the three "stationary" trimer geometries. In a preliminary report on the trimer lineshape, the pseudorotating spectrum was shown to exhibit an "alternating linewidth" effect, as would be expected for an exchanging radical (4). In this paper, trimer linewidths are reported and discussed from the viewpoint of a purely phenomenological model involving a stochastic modulation of the trimer hyperfine splitting. Linewidth expressions, derived for the particular case of pseudorotating K_3, lead to a simulated ESR spectrum in quite good agreement with that observed. Approximate values for the trimer correlation and transverse relaxation times are computed. Possible exchange mechanisms are outlined in the last section.

Experimental

The experimental details have been reported elsewhere (1, 3). Briefly, matrices are formed by codeposition of excess argon with atomic potassium on a sapphire plate mounted inside an ESR cavity which is itself attached to a variable temperature liquid helium dewar. Cluster formation occurs during deposition and is accomplished by warming the sapphire surface above a nominal deposition temperature of 4.2 K. For spectra shown here, temperature measurements were made with a calibrated carbon resistor and are judged accurate to within ± 5%.

Trimer Spectra

Alkali trimer molecules have a relatively flat potential surface, whose principal features are a conical peak surrounded by a trough containing three potential wells (3, 5, 6). Figure 1 shows the trimer potential surface plotted as a function of Q_x and Q_y, the doubly degenerate pair of normal mode coordinates for D_{3h} symmetry (3). The central peak corresponds to a degenerate, $^2E'$ ground state of equilateral triangular geometry. The three potential minima have obtuse angled isosceles geometry ($^2B_2$ symmetry) and arise from three possible Jahn-Teller distortions from D_{3h} symmetry. Adjacent minima are separated by relatively low energy saddle points of acute isosceles geometry ($^2A_1$ symmetry). As shown by the broken line in Figure 1 this situation permits the intraconversion of obtuse triangular forms without passing through the energetically remote equilateral triangle ("pseudorotation").

In Reference 3, two distinct ESR spectra were identified for potassium clusters in argon matrices. Both spectra have doublet ground states ($S = ½$) and a well resolved hyperfine (hf) structure arising from the Fermi contact interaction of the unpaired electron spin with three $I = ½$ nuclei. Seven groups of four transitions each were assigned to a potassium trimer of $^2B_2$ symmetry whose apical and two equivalent terminal atoms have hf splitting

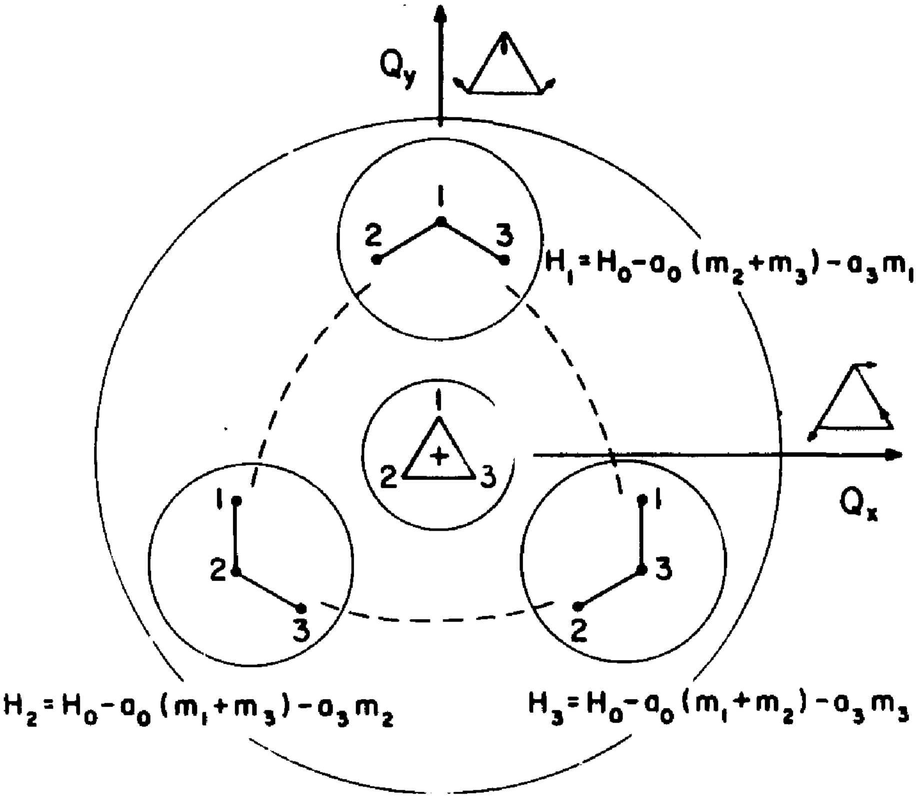

Figure 1. Normal coordinate and real space description of pseudorotating K_3. Circles represent energy contours for the trimer potential surface (3).

constants a_3 and a_0, respectively. Powder spectra were fit to

$$H_i = H_0 - a_0 M - a_3 m_i \qquad (1)$$

in which $m_i = m_1$, m_2 or m_3 is the spin projection quantum number for the apical nucleus and M is the sum of the corresponding quantities for the remaining two atoms. The term $H_0 = g_e/g_0\ H_e$, where H_e and g_e denote the resonance field and g value for a free electron, describes the Zeeman interaction for an isotopic g tensor, $g = g_0 1$. For K_3 (estimated uncertainties in parentheses), $g_0 = 1.9985(5)$ with $a_0 = 39.0(3)$ gauss and $a_3 = \pm\ 4.7(2)$ gauss (3). The a_0 constant originates from bonding 4s orbitals on the terminal atoms and is positive; a_3, however, arises from spin polarization effects and may be either positive or negative (1, 2, 3).

Figure 1 gives magnetic field positions, derived from Equation (1) with $i = 1$, 2 or 3, for the three distorted trimer geometries. Since these differ only by a numbering of the nuclei, the ESR spectrum of "frozen" K_3 molecules will consist of a superimposition of indistinguishable obtuse angled trimer species. If, however, adjacent minima can exchange on a sufficiently fast time scale, then an average spectrum,

$$\langle H \rangle = \tfrac{1}{3} \sum_{i=1}^{3} H_i = H_0 - \tfrac{1}{3}(2a_0 + a_3)M' \qquad (2)$$

for which all three ^{39}K nuclei appear equivalent, will be observed. Since $M' = m_1 + m_2 + m_3$ ranges from $+\tfrac{9}{2}$ to $-\tfrac{9}{2}$ in integral steps, a ten line hf pattern having $\langle a \rangle = \tfrac{1}{3}(2a_0 + a_3)$ and a g value identical to that for the "frozen" trimer would be predicted. As discussed in Reference 3, the second ESR spectrum observed for argon matrices exactly fulfills these requirements. Previously denoted K_n, this spectrum was shown to have magnetic parameters $g_0 = 1.9990(5)$ and hf constant $a = 24.5(7)$ gauss, in excellent agreement with the predictions of Equation (2), $g_0 = 1.9985(5)$ and $a = 24.3(3)$ gauss, if a_3 is assumed to be negative.

Figure 2 shows the pseudorotating trimer spectrum at $T = 34.2$ K (4). Also shown in this figure is a "stick spectrum" in which component intensities, in the ratio 1:3:6:10:12:12:10:6:3:1, reflect the M' degeneracy of three equivalent $I = \tfrac{3}{2}$ nuclei in the high field limit (3, 4). Magnetic field positions for the simulated spectrum were computed using Equation (2) and the experimental parameters of Reference 3. A broadening of the low field transitions is observed at all temperatures and most likely arises from the trapping of radicals in more than one matrix site. Aside from this asymmetry in the linewidths, the agreement between computed and observed intensity ratios is quite good. At low temperatures, however, component intensities differ markedly from the expected 1:3:6:10:12:12:10:6:3:1 pattern. As shown for $T = 4.2$ K in Figure 3a the $M' = \pm\ \tfrac{7}{2}$, $\pm\ \tfrac{5}{2}$ and $\pm\ \tfrac{1}{2}$ components show a pronounced line broadening whereas $M' = \pm\ \tfrac{9}{2}$ and $\pm\ \tfrac{3}{2}$ remain narrow.

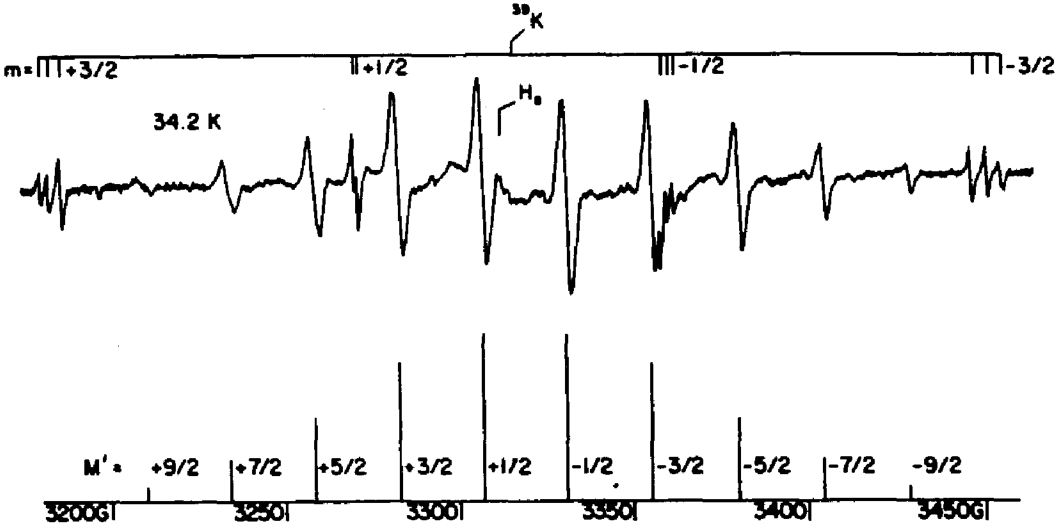

Figure 2. ESR spectrum of pseudorotating K_3 in an Ar matrix at 34.2 K. The "stick spectrum" shows the predicted intensity distribution for three equivalent ^{39}K nuclei. Also indicated are K atom resonances for several matrix sites. $H_e = 3312.3$ G is the resonance field of a free electron for a cavity frequency of 9.2824(2) GHz.

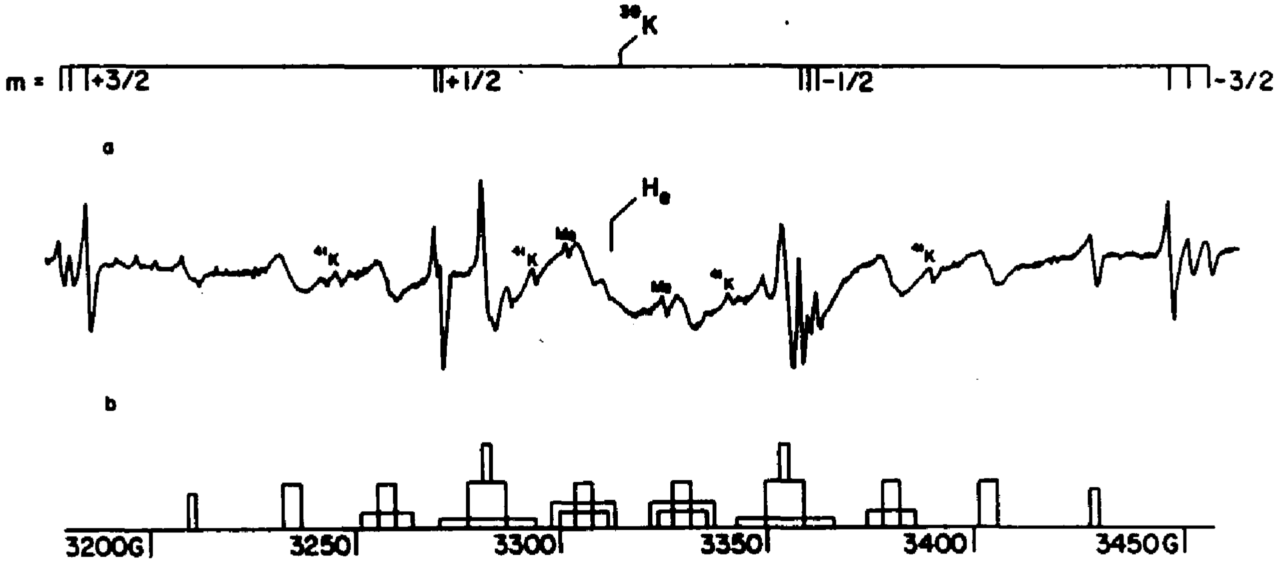

Figure 3. Comparison of observed (a) and simulated (b) spectra for pseudorotating K_3 in Ar matrices at 4.2 K. See also Fig. 2.

In Reference 4, this "alternating linewidth" effect (8) was shown to be consistent with a temperature dependent pseudorotation in K_3. A correlation diagram, which relates transition fields for the three obtuse angled trimer geometries, qualitatively predicts line broadening for $M' = \pm 7/2, \pm 5/2$ and $\pm 1/2$ when pseudorotation is relatively slow. At high temperatures fast exchange leads to the motionally averaged spectrum shown in Figure 2.

Trimer Linewidths

The linewidth analysis for pseudorotating K_3 closely follows the more familiar treatment of relaxation mechanisms in both the NMR and ESR of chemically exchanging systems (8 - 12). Physically, the electron spin interacts with both the static, laboratory magnetic field and a random, fluctuating magnetic field arising from an isotropic hf coupling with the nuclear spins of the trimer. Hyperfine coupling constants are not explicitly time dependent. Rather they assume different values according as to possible occupancies of the three $^2B_2$ minima shown in Figure 1. Thus the hf interaction is time dependent only if the trimer is assumed to "jump" randomly from one well to another.

Two terms may contribute to the trimer linewidth. Diagonal elements of the hf interaction produce a secular modulation of the magnetic levels of both electron spin states without causing transitions. Off diagonal elements, which cause (lifetime broadening) transitions between Zeeman levels, give rise to a non-secular contribution. For either effect to be significant, the hf interaction must have "sufficient" magnitude. Non-secular terms face the additional requirement that the Fourier spectrum of the interaction be rich at the Larmor frequency, $\omega_0/2\pi = 9.3$ GHz. For K_3 in argon, the exchange rate for jumping between adjacent $^2B_2$ minima is never sufficiently fast for non-secular terms to make an appreciable contribution.

Several formalisms have been applied to relaxation in exchanging radicals. Principal among these are modifications of the classical Bloch equations (8, 12) and the more rigorous quantum mechanical theory of Redfield *et al.* (8 - 11). When applied in their simplest form, as in the present case for K_3, both approaches lead to the same result. Since the theory has been elegantly described by many authors (8 - 12), only those details which pertain to the particular example of K_3 will be presented here. Secular terms contribute to the ESR linewidth (Γ) and transverse relaxation time (T_2) by an amount

$$\Gamma = T_2^{-1} = \int_0^\infty G(\tau)\, d\tau \tag{3}$$

where the correlation function $G(\tau) = \langle h_i h_j \rangle$ is the appropriate ensemble average for exchanging trimer species, and,

$$h_i = H_i - \langle H \rangle \tag{4}$$

is defined, through Equations (1) and (2), in order to make $\langle h_i \rangle$ vanish. Although Equation (3) is strictly applicable to absorption spectra having Lorentzian lineshapes, its use in connection with a powder spectrum will have only a minor effect on the conclusions of this paper. The several approximations applied to deriving Equation (3) are well described in Reference 10. Most significant is the neglect of perturbation terms past second order. As a consequence, expressions derived in this section will be valid over most, but not all, of the temperature range employed in the ESR experiments.

Figure 4 shows the "three jump model" used in deriving $G(\tau)$ for pseudorotating K_3. Jumping between adjacent wells ($i = 1, 2$ or 3) is assumed to be a stationary, Markov process which may be characterized by a single, phenomenological rate constant λ. The three potential minima are assumed to be identical so that the probability of occupying any one well at a particular time τ is given by $P_i(\tau) = \frac{1}{3}$. Under these circumstances

$$G(\tau) = \sum_{i,j=1}^{3} h_i h_j P_i(o) P_{ij}(\tau) \qquad (5)$$

where the $P_{ij}(\tau)$ are conditional probabilities relating the occupancies of wells i and j at the times $\tau = o$ and $\tau = \tau$, respectively. The $P_{ij}(\tau)$ may be formally derived by application of the Kolmogorov equations of probability theory (13). For the situation represented in Figure 4,

$$\begin{aligned} dP_{ii}/dt &= -2\lambda P_{ii} + 2\lambda P_{ij} \\ dP_{ij}/dt &= -\lambda P_{ij} + \lambda P_{ii} \end{aligned} \qquad (6)$$

analogous to the more familiar expressions often encountered in the elementary theory of chemical reactions. For initial conditions $P_{ii}(o) = 1$ and $P_{ij}(o) = 0$, the simultaneous Equations (6) have a solution

$$\begin{aligned} P_{ii}(\tau) &= \tfrac{1}{3}[1 + 2e^{-\tau/\tau_c}] \\ P_{ij}(\tau) &= \tfrac{1}{3}[1 - e^{-\tau/\tau_c}] \end{aligned} \qquad (7)$$

where $\tau_c = (3\lambda)^{-1}$ is a characteristic, correlation time for trimer exchange. Substitution of 4 and 7 in the expression 5 gives

$$G(\tau) = \tfrac{2}{3}(a_0 - a_3)^2 f(M', k) e^{-\tau/\tau_c} \qquad (8)$$

where

$$f(M', k) = M'^2 - e(m_1 m_2 + m_1 m_3 + m_2 m_3) \qquad (9)$$

with $k = m_1 m_2 m_3$. The function $f(M', k)$ is listed in Table I.

Table I. Parameters appearing in linewidth variation of pseudorotating K_3, Equation (10) of text.

M'	k	f(M', k)	D_k
±9/2	27/8	0	1
±7/2	9/8	1	3
±5/2	3/8	1	3
	-9/8	4	3
±3/2	1/8	0	1
	-3/8	3	6
	-27/8	9	3
±1/2	-1/8	1	3
	3/8	4	3
	-9/8	7	6

Also shown in this table are the number (D_k) of transitions (m_1, m_2, m_3) which contribute to a given k. Applying Equation (3) to individual hf components M' = $+\frac{9}{2}$,--,$-\frac{9}{2}$ gives

$$(M', k) = \tfrac{2}{3}(a_0 - a_3)^2 \cdot f(M', k) \cdot \tau_c \qquad (10)$$

where the last expression has been notated to show that exchange contributions to the trimer linewidth will, in general, be a sum of Lorentzian functions k. Equation (10) also shows that ESR linewidths are temperature dependent only through a corresponding variation in the correlation time τ_c.

Results for K_3

Table II shows the temperature variation in the peak-to-peak

Table II. Measured linewidth variation for pseudorotating K_3.

	Γ(gauss)			Γ(gauss)	
T(K)	M' = $-\frac{7}{2}$	M' = $-\frac{5}{2}$	T(K)	M' = $-\frac{7}{2}$	M' = $-\frac{5}{2}$
4.2	4.55	4.85	15.2	2.67	2.67
6.7	4.36	4.36	15.3	2.87	2.87
7.6	4.06	3.56	16.2	2.97	2.77
9.5	3.17	3.17	17.1	2.48	2.87
11.7	2.97	3.07	19.1	2.77	2.77
			20-35	2.18	2.57

linewidth for the M' = $-\frac{7}{2}$ and M' = $-\frac{5}{2}$ components for pseudorotating K_3. After an initial annealing of the matrix, measured linewidths (Γ) are independent of the sample history and, within experimental error, depend only upon temperature. Above T ~ 20 K, ESR linewidths remain approximately constant and are represented by average values, Γ_0, as shown in the last entry of Table II. Γ_0 is taken to be a measure of temperature independent contributions to the ESR linewidth. Although powder spectra are most often inhomogeneously broadened, the exchange contribution to the trimer linewidth is assumed to be given by $\Gamma - \Gamma_0$. Owing to the 10-20% uncertainty in Γ, there is considerable scatter in these differences, particularly at higher temperatures. However, the linewidth data do give approximate values for τ_c and T_2 and allow an experimental test of the "three jump model" introduced in the preceding section.

Figures 3a and 3b show, respectively, observed and simulated spectra for the pseudorotating trimer at T = 4.2 K. Absorption linewidths for the "bar spectrum" were derived from Equation (10), with f(M', k) from Table I and $\frac{2}{3}(a_0 - a_3)^2 = 3.4 \times 10^{15}\ \text{sec}^{-2}$ from Reference 3. The correlation time, $\tau_c = 3.8 \times 10^{-9}$ sec, was chosen to give the measured linewidth for $M' = -\frac{7}{2}$, $\Gamma = \Gamma_0 + \Gamma(M', k) = 4.6$ G from Table II. Relative areas in Figure 3b reflect the D_k degeneracy given in Table I. For ESR transitions, $(m_1, m_2, m_3) = (\pm\frac{3}{2}, \pm\frac{3}{2}, \pm\frac{3}{2})$ and $(\pm\frac{1}{2}, \pm\frac{1}{2}, \pm\frac{1}{2})$, f(M', k) = 0 and trimer exchange is not predicted to contribute to the linewidth. Accordingly, bar spectra for these transitions correspond to $\Gamma = \Gamma_0 = 2.2$ G with ESR intensities equal to that measured for $M' = -\frac{9}{2}$. Aside from the matrix site effects noted earlier, the general features of the observed spectrum are quite well represented in Figure 3b.

Trimer linewidths were compared with both an exponential, $\tau_c = \tau_0 e^{\delta/T}$, and a power law, $\tau_c = \tau_0 T^{-n}$, temperature dependence in the correlation time τ_c. Figure 5 shows the least squares fit for $M' = -\frac{7}{2}$. Both plots represent the experimental linewidth equally well (correlation coefficient, r = 0.90) and the present data are not sufficiently accurate to distinguish between the two interpretations. For reasons given below, the data point at T = 4.2 K was not included in this fit. Similar results (but with r = 0.98) pertain to $M' = -\frac{5}{2}$. Although, as shown in Figure 3b, two k components contribute to this transition, it is most likely that the broad, f(M', k) = 4 and narrow, f(M', k) = 1, features are sufficiently well separated for the latter to dominate the observed $M' = -\frac{5}{2}$ linewidths.

Table III gives the computed parameters for both $M' = -\frac{7}{2}$ and

Table III. Least squares parameters (defined in text) for trimer correlation times (τ_c). Estimated errors are given in parentheses.

	$\tau_c = \tau_0\, e^{\delta/T}$		$\tau_c = \tau_c\, T^{-n}$	
M'	$\tau_0 \times 10^{11}$(sec)	δ(K)	$\tau_0 \times 10^{8}$(sec K^{n})	n
$-\frac{7}{2}$	17(5)	16(3)	3.4(21)	1.5(3)
$-\frac{5}{2}$	5.8(11)	21(2)	18(11)	1.9(2)

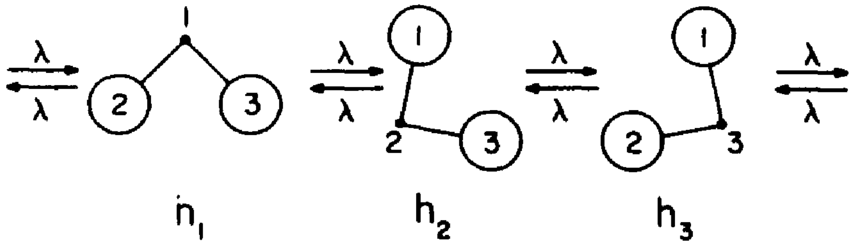

Figure 4. Three-jump model for pseudorotating K_3. See Eq. 4 for definition of h_i.

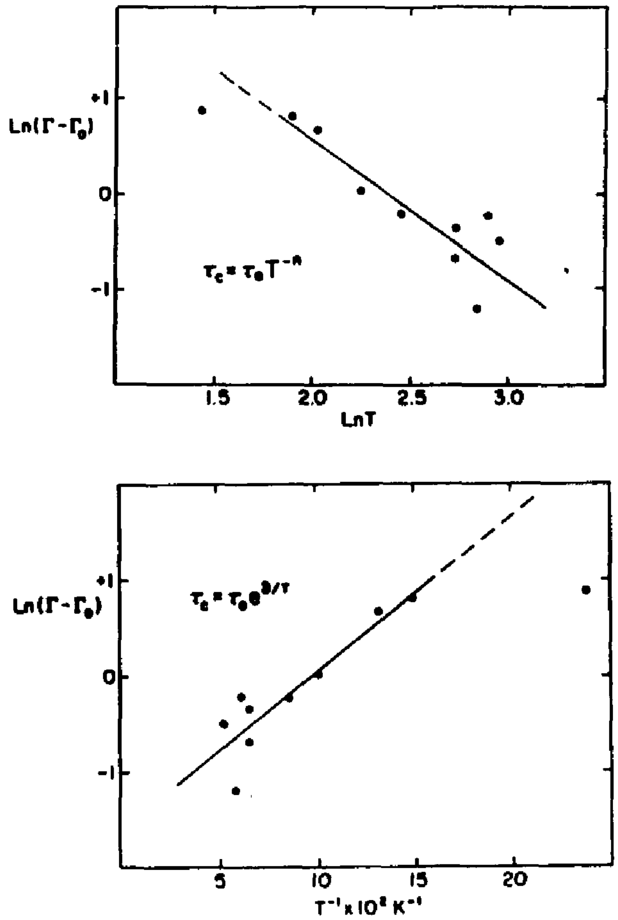

Journal of Chemical Physics

Figure 5. Comparison of measured ESR linewidths (Γ) with assumed temperature dependence in trimer correlation times (τ_c) a, $\tau_c = \tau_0 T^{-n}$ b, $\tau_c = \tau_0 e^{b/T}$.

$M' = -\frac{1}{2}$. Estimated uncertainties, in parentheses, represent one standard deviation in the least squares fit to the experimental data. Table IV summarizes several parameters of interest for pseudorotating K_3. These data were calculated from Equation (10), with $f(M', k) = 1$ and $\frac{2}{9}(a_0 - a_3)^2 = 3.4 \times 10^{15}$ sec^{-2} from Reference 3, together with the least squares τ_0 and δ from Table III. These example results permit a check on several of the approximations alluded to earlier. A necessary condition for second order perturbation theory to be valid is $(\tau_C/T_2)^{\frac{1}{2}} << 1$ (10). As shown by the data in column 5 of Table IV, this approximation breaks down at low temperatures and predicted linewidths become much larger than those actually observed. The ratio of the non-secular to the secular contribution to the trimer linewidth is of order $(1 + \omega_0{}^2\tau_C{}^2)^{-1}$ (8 - 12). As shown by the last entry in Table IV line broadening by non-secular terms is quite negligible over the temperature range T = 4-20 K.

Table IV. Temperature variation in correlation time (τ_C), secular linewidth, $\Gamma(M', k)$, and transverse relaxation time (T_2) for $M' = -\frac{1}{2}$. The Larmor frequency $\omega_0/2\pi = 9.3$ GHz. For an explanation, see text.

T (K)	$\tau_C \times 10^{10}$ (sec)	$\Gamma(M', k)$ (gauss)	$T_2 \times 10^8$ (sec)	$(\tau_C/T_2)^{\frac{1}{2}}$	$\omega_0\tau_C$
4	93	11	3.2	0.54	540
6	24	2.9	12	0.14	140
8	13	1.6	23	0.08	76
10	8.4	1.0	35	0.05	49
15	4.9	0.6	60	0.03	29
20	3.8	0.5	77	0.02	22

Discussion

Contingent upon the details of the potential surface for K_3, several mechanisms may give rise to the observed temperature dependence in τ_C. If the ground vibronic state for the trimer is of order kT below the energy barrier to pseudorotation, then the correlation time (inversely proportional to the rate constant for exchange) would be expected to show Arrhenius type behavior. Alternatively, the trimer ground state might lie above the pseudorotation barrier, as has been suggested for Li_3 (5). In this situation a fast, but temperature independent, exchange would be predicted. However, since the trimer potential surface is markedly flat, matrix effects may play a particularly important role. Thus the matrix might "lock" the trimer into an obtuse angled geometry at some temperatures but be sufficiently fluid to allow pseudorotation at others.

For Na_3, which is expected to be more closely analogous to the potassium trimer than Li_3, Martin and Davidson (6) estimate a zero point vibrational energy $\omega \sim 85$ cm^{-1} with a barrier to pseudorotation, $2\beta \sim 200$ cm^{-1}. Particularly critical for Jahn-Teller systems (14), is the distortion parameter ρ_0 (Δ in the notation of (6)). Referring to Figure 1, ρ_0 is the radial distance from the conical peak to the average energy minimum in the trough region of the trimer potential surface. For Na_3, $\rho_0 \sim 0.5$ Å (6). If vibrational frequencies, potential parameters, and bond distances scale according to, respectively, the force constant, bond energy, and internuclear distance of the corresponding alkali dimers, then, very approximately, $\omega \sim 65$ cm^{-1} with $2\beta \sim 150$ cm^{-1} and $\rho_0 \sim 0.6$ Å for K_3. Consequently the ground vibronic level of K_3 is some 85 cm^{-1} below the pseudorotation barrier and, for $4 \leq T \leq 35$ K, exchange can only occur by quantum mechanical tunneling. This rate may be approximately calculated using a WKB method similar to that applied to the more familiar case of ammonia inversion (15). Using the previously estimated parameters for K_3 (reduced mass, $\mu = \frac{2}{3}m = 26$ amu) and numerical integration of an assumed cosine potential we find a tunneling frequency of order 1 GHz.

Although temperature dependent tunneling is not, of course, to be expected for gas-phase molecules, its occurence for transition metal complexes in the solid phase has been well documented (14, 16, 17). Even in carefully prepared crystals, random strains are of sufficient magnitude to make the previously assumed equivalence of potential minima no longer valid. If, for K_3 in argon, matrix effects contribute a similar blurring of the trimer energy levels, then tunneling between adjacent wells no longer conserves energy. Transitions from the vibronic ground state of one well to the corresponding level of its inequivalent neighbor must now be stimulated by phonon absorption or emission. As given elsewhere (14, 16, 17), the several possible mechanisms correspond to the direct Raman or Orbach processes more familiarily applied to spin lattice relaxation. In all three cases this situation leads to an attenuation of the gas-phase tunneling frequency and complex, generally hyperbolic, temperature behavior for τ_c. In certain limiting situations either an exponential or power law temperature dependence is predicted. Consequently our results for K_3 in argon are also consistent with a trimer zero point energy well below the pseudorotation barrier.

Acknowledgments

This work was supported by the City University of New York PSC-BHE Research Award Program and by the National Science Foundation under grant number CHE 79-13260. Acknowledgment is made to the Donors of The Petroleum Research Fund, administered by the American Chemical Society, for partial support of this research.

Literature Cited

1. Lindsay, D. M.; Herschbach, D. R.; Kwiram, A. L. Mol. Phys. 1976, 32, 1199.
2. Lindsay, D. M.; Herschbach, D. R.; Kwiram, A. L. Mol. Phys. 1980, 39, 529.
3. Thompson, G. A.; Lindsay, D. M. J. Chem. Phys. 1981, 74, 959.
4. Thompson, G. A.; Tischler, F.; Garland, D.; Lindsay, D. M. Surf. Sci. 1981, in press.
5. Gerber, W. H.; Schumacher, E. J. Chem. Phys. 1978, 69, 1692.
6. Martin, R. L.; Davidson, E. R. Mol. Phys. 1978, 36, 1713.
7. Dietz, E. R. Phys. Rev. 1981, A23, 751.
8. Atherton, N. M. "Electron Spin Resonance"; Wiley: New York, 1973.
9. Freed, J. H.; Fraenkel, G. K. J. Chem. Phys. 1963, 39, 326.
10. Abragam, A. "The Principles of Nuclear Magnetism"; Oxford: London, 1961.
11. Slichter, C. P. "Principles of Magnetic Resonance"; Harper and Row: New York, 1963.
12. Carrington, A.; McLachlan, A. D. "Introduction to Magnetic Resonance"; Harper and Row: New York, 1967.
13. Feller, W. "An Introduction to Probability Theory and Its Applications", Wiley: New York, 1967; Volume I.
14. Englman, R. "The Jahn-Teller Effects in Molecules and Crystals"; Wiley: New York, 1972.
15. Townes, C. H.; Schawlow, A. I. "Microwave Spectroscopy"; McGraw-Hill: New York, 1955.
16. Ham, F. S. in "Electron Paramagnetic Resonance", edited by Geschwind, S.; Plenum: New York, 1972.
17. Williams, F. I. B.; Krupka, D. C.; Breen, D. P. Phys. Rev. 1969, 179, 255.

RECEIVED September 18, 1981.

Appendix A.4 Reprint: Sur. Sci. 106, 408 (1981).

Surface Science 106 (1981) 408–414
North-Holland Publishing Company

TEMPERATURE DEPENDENCE IN THE ESR INTENSITIES OF MATRIX ISOLATED POTASSIUM CLUSTERS

G.A. THOMPSON, Frances TISCHLER, Denise GARLAND and D.M. LINDSAY
Department of Chemistry, City University of New York, City College, New York, New York 10031, USA

Received 8 September 1980; accepted for publication 22 October 1980

Two distinct ESR spectra are observed when atomic potassium and argon are codeposited under conditions favorable to aggregation. A pattern of seven equally spaced quartets may be attributed to potassium trimer molecules with a symmetric linear or obtuse angled isosceles geometry. Trimer transitions show a pronounced peaking in intensity at $T \sim 17$ K. A second ESR spectrum consists of ten equally spaced hyperfine components, whose relative intensities approach the predicted distribution for three equivalent ^{39}K nuclei at high temperatures, but show a noticeable "alternating linewidth" effect at lower temperatures. These observations are interpreted in terms of a temperature dependent "pseudorotation" between three Jahn–Teller distortions of a D_{3h} molecule, most likely the trimer.

1. Introduction

In previous work [1, 2] by two of us (G.A.T. and D.M.L.), we reported magnetic parameters for two matrix isolated potassium clusters: The trimer, K_3, and a radical of distinctly different spectral character which we designated K_n. Magnetic parameters for K_3 were found to be markedly similar to those of the isovalent sodium trimer [3]. A spin population analysis for both Na_3 [3, 4] and K_3 [1, 2] shows that the unpaired electron resides almost entirely on two equivalent alkali atoms and has predominantly s- rather than p-character. Polarization effects induce a small spin density on the third atom. These data are consistent with both simple bonding ideas [2, 3] and recent ab initio calculations [5, 6], suggesting a linear or obtuse angled isosceles geometry of ground state symmetry $^2\Sigma_u^+$ or $^2B_2$, respectively. The ESR spectrum of K_n [1, 2] implies that the unpaired electron in this species is equally distributed over *three* ^{39}K nuclei. Suggested [1, 2] candidates for the carrier of this spectrum were the potassium pentamer with a chain structure, for which the unpaired electron would be expected to reside equally on three atoms, or a "pseudorotating" isomer of K_3. In the latter case, all three atoms are made equivalent by rapid exchange between the three obtuse angled geometries which arise from Jahn–Teller distortions from D_{3h} symmetry.

In this paper we present temperature dependent ESR intensities for potassium clusters in argon matrices and show evidence for an "alternating linewidth" effect [7, 8] in the ESR spectrum of K_n. This phenomenon is characteristic of dynamic processes in molecules and so provides additional evidence for a pseudorotation interpretation of K_n. A correlation diagram, which relates transition fields for the three obtuse angled trimer molecules, qualitatively explains the observed linewidth alternation in K_n.

2. Experimental

The experimental details have been reported elsewhere [2, 3]. Briefly, matrices are formed by codeposition of excess argon with atomic potassium on a sapphire plate mounted inside an ESR cavity which is itself attached to a variable temperature liquid helium dewar. Cluster formation occurs during deposition and is accomplished by warming the sapphire surface above a nominal deposition temperature of 4.2 K. For spectra shown here, temperature measurements were made with a calibrated carbon resistor and are judged accurate to within ±5%.

3. Hyperfine structure

A detailed discussion of ESR line positions is given in ref. [2]. As an aid to describing the intensity measurements which follow, this section summarizes certain features of the previous analysis. Both K_3 and K_n have doublet ground states ($S = 1/2$) and a well resolved hyperfine (hf) structure arising from the Fermi contact interaction of the electron spin with several $I = 3/2$ nuclei. All observed transitions have a first derivative lineshape as would be expected for powder spectra having an isotropic g tensor ($g = g_0 I$) and an isotropic hf interaction ($A_i = a_i I$).

Magnetic field positions for the trimer spectrum, seven groups of four transitions each, are described by

$$H(M, m_3) = (g_e/g_0)\left[H_e - \sum_{i=1}^{3} a_i m_i\right] = (g_e/g_0)\,[H_e - a_0 M - a_3 m_3]\,, \tag{1}$$

where m_1 and m_2 are nuclear spin projection quantum numbers for two equivalent ^{39}K nuclei ($a_1 = a_2 = a_0$) and $M = m_1 + m_2$ is their sum. Since $I = 3/2$, $m_i = \pm 3/2$ or $\pm 1/2$ and M ranges in integral steps from +3 to −3. The quantum number m_3 and hf constant a_3 pertain to the third, non-equivalent nucleus. H_e and g_e denote, respectively, the resonance field and g value for a free electron. An expression similar to eq. (1), but with the added complication of a significant second order hf interaction, has been used to describe the ESR spectrum of Na_3 [3]. Since $a_3 \ll a_0$ [1, 2], eq. (1) gives rise to a septet of quartets as observed. For both K_3 and Na_3, a_0 arises from isotropic spin density on the trimer terminal atoms and is positive. However a_3 arises from spin polarization effects at the central or apical position and may be positive or negative.

Component transition fields for the ten line hf pattern observed for K_n were fit to,

$$H(M') = (g_e/g_0)[H_e - a_0 M'] \,. \tag{2}$$

Here $M' = m_1 + m_2 + m_3$ denotes the z-component of the total nuclear spin angular momentum of three magnetically equivalent ^{39}K nuclei ($a_1 = a_2 = a_3 = a_0$) and H_e, g_e have the same meaning as in eq. (1). For $I = 3/2$, M' ranges from $+9/2$ to $-9/2$ in integral steps.

4. Temperature dependence

Both K_3 and K_n are present in freshly deposited matrices at 4.2 K, but their spectra are difficult to deconvolute prior to an initial annealing of the matrix. Subsequently, the ESR intensities of both species are extremely reproducible, depending only upon the matrix temperature. It is these intensity data that we discuss in the present article. Transitions from atomic potassium, also observed in our matrices, show little intensity change with temperature.

Fig. 1 shows a plot of (first derivative) peak heights versus temperature for the $(M, m_3) = (+3, +1/2)$ component of the trimer spectrum and the $M' = -5/2$ component of K_n. The notation (M, m_3) and M' is the same as that introduced in connection with eqs. (1) and (2) of the preceding section. A marked peaking of intensity at $T \sim 17$ K is common to all unobscured (M, m_3) components of K_3 and is also apparent in spectra recorded during annealing. Within experimental error, trimer linewidths remain unchanged (after annealing) over the temperature range 4.2–25 K. This is somewhat surprising, since most mechanisms [2] for the intensity behavior in fig. 1 would be expected to give a broadening of ESR linewidths [9]. For K_n, there is a trend to smaller peak heights at lower temperatures, as shown for $M' = -5/2$ in fig. 2. This trend is common to all component transitions of K_n, but is reversed for $M' = \pm 9/2$ and $\pm 3/2$ below $T \sim 10$ K. Peak areas, approximated to the square of the linewidth times the (first derivative) peak height, show a less pronounced trend with temperature, but these data have a large experimental scatter.

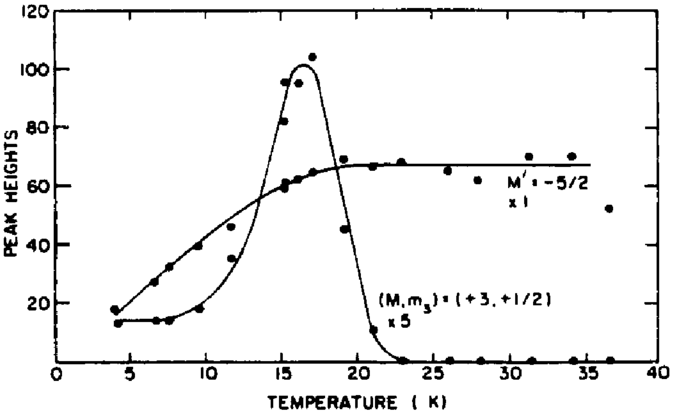

Fig. 1. Temperature dependence of ESR intensities for potassium clusters in argon matrices. $M' = -5/2$ and $(M, m_3) = (+3, +1/2)$ pertain to one component each of, respectively, the ESR spectrum shown in fig. 2 and the ESR spectrum of K_3, refs. [1, 2]. Relative to $M' = -5/2$, trimer intensities are 1/5 of those shown in the figure

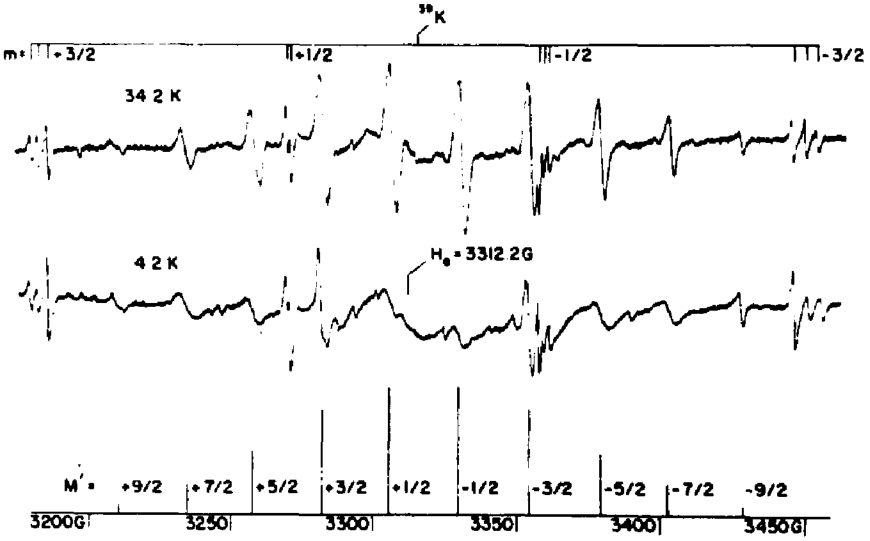

Fig. 2. Ten line spectrum of a radical $^{39}K_n$ in an argon matrix at 4.2 and 34.2 K. The "stick spectrum" shows the predicted intensity distribution for three equivalent ^{39}K nuclei. Also indicated are potassium atom resonances ($m = \pm 3/2, \pm 1/2$) for several matrix sites. H_e = 3312.2 G is the resonance field of a free electron for a cavity frequency of 9.2824(2) GHz.

In contrast to the trimer, however, K_n spectra show striking variations in linewidth with temperature, individual M' components being differently affected. Fig. 2 shows spectra recorded at two extreme values of temperature, 4.2 and 34.2 K. A broadening of the low field components, most pronounced for $M' = +9/2$, probably arises from two different matrix sites and gives an asymmetric appearance to the spectra at all temperatures. The "stick" diagram in fig. 2 was computed from eq. (2) and the best fit parameters of refs. [1, 2]. Component intensities, arising from the M' degeneracy of three equivalent ^{39}K nuclei in the high field limit [2, 10], are in the ratio 1:3:6:10:12:12:10:6:3:1. At high temperatures observed intensities do indeed approach the predicted ratio, but this is certainly not the case at $T = 4.2$ K. At low temperatures the $M' = \pm 7/2$, $\pm 5/2$ and $\pm 1/2$ components show pronounced line broadening, whereas $M' = \pm 9/2$ and $\pm 3/2$ are noticeably narrowed. A similar behavior in the ESR spectra of organic radicals in solution is generally termed the "alternating linewidth" effect [7, 8].

5. Discussion

Recent ab initio calculations on Li_3 [8] and Na_3 [9] emphasize the importance of dynamic Jahn–Teller effects in alkali trimer molecules. The principal features of the trimer potential surface are a central peak surrounded by a trough containing three potential wells. The three minima have obtuse isosceles geometry ($^2B_2$ symmetry) and are indistinguishable except for a numbering of the nuclei. Adjacent wells are separated by saddle points which provide a relatively low energy path for intraconverting one obtuse form into another (pseudorotation).

In earlier work [2] it was pointed out that sufficiently fast pseudorotation would lead to an averaged trimer spectrum in which all three ^{39}K nuclei would appear equivalent. Moreover, the measured hyperfine splitting constant for K_n was almost exactly equal to the appropriate average of the measured hf splitting constants for the trimer, when a_3 was assumed to be negative.

Our observation of an alternating linewidth effect is likewise consistent with a pseudorotation mechanism. Fig. 3 shows a partial correlation diagram for the transition frequencies of the three obtuse angled forms of K_3. Each stick spectrum represents a different occupancy of the apical position as indicated at the top of the figure. Transition frequencies, plotted vertically, correspond to the spectral assignment of refs. [1, 2], eq. (1) with

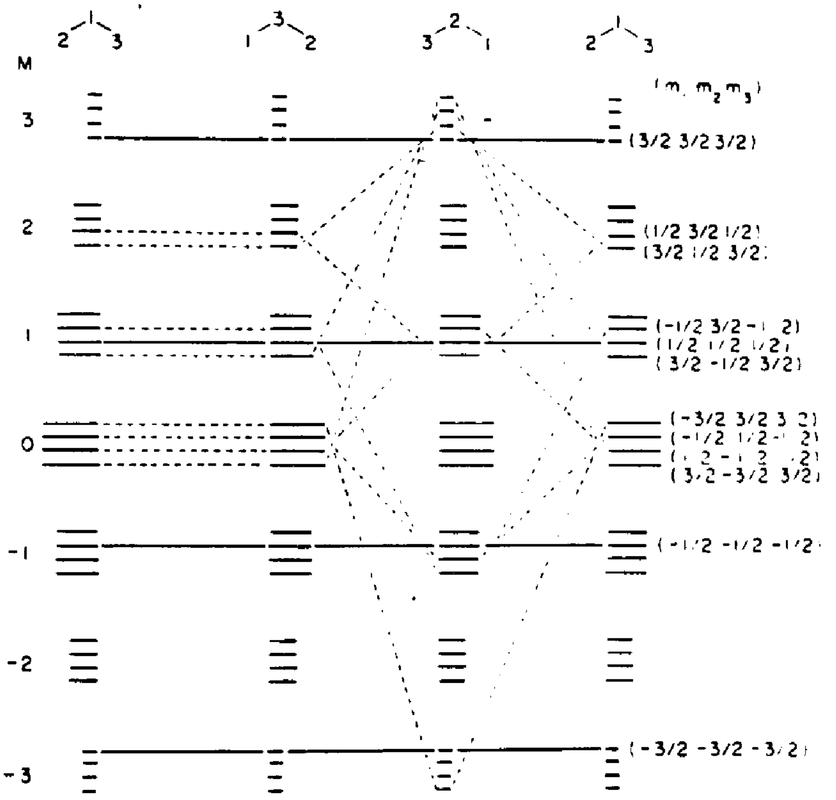

Fig. 3. Partial correlation diagram for the transition frequencies of three obtuse angled $^{39}K_3$ molecules. For an explanation, see text.

$a_3 < 0$. Relative intensities, plotted horizontally, denote the M-degeneracy associated with two equivalent $I = 3/2$ nuclei in the high field limit [3]. On the right hand side of fig. 3 several transitions have been labelled $(m_1 m_2 m_3)$, where $m_i = \pm 1/2, \pm 3/2$ is the magnetic quantum number for distinguishable nuclei $i = 1, 2$, or 3. Adjacent columns are correlated by joining just those transitions which have the same m-value for all three nuclei. Most correlations have been omitted for clarity. It is apparent that, while several transitions are unaffected by exchange between adjacent $^2B_2$ wells, in only four cases do frequencies remain constant when all three obtuse angled species are considered. These latter transitions have $(m_1 m_2 m_3) = (\pm 3/2 \pm 3/2 \pm 3/2)$ and $(\pm 1/2 \pm 1/2 \pm 1/2)$, corresponding to $M' = \pm 9/2$ and $\pm 3/2$, respectively. Thus the situation for K_n may be analogous to exchange effects in organic radicals in solution [7, 8]. At high temperatures, where exchange might be expected to be fast, all three nuclei become equivalent, giving an averaged ten line spectrum, as shown for $T = 34.2$ K in fig. 2. At low temperatures, however, pseudorotation rates may become comparable to the ESR timescale. In this regime $M' = \pm 9/2$ and $\pm 3/2$ are relatively unaffected by exchange and so remain narrow, but $M' = \pm 7/2, \pm 5/2$ and $\pm 1/2$ experience large frequency shifts and become broadened.

In conclusion, it should be pointed out that the pseudorotation mechanism outlined above need not imply that K_n is the potassium trimer. Any cluster for which the Jahn–Teller interaction might induce a similar three fold degenerate distortion is also plausible. For example, this situation also pertains to a potassium pentamer with a trigonal bipyramid structure (D_{3h} point group). For this geometry, simple Hückel calculations predict that the unpaired electron will occupy a doubly degenerate molecular orbital whose wavefunction has a node at both axial atoms. The spin distribution for the three equatorial atoms is identical to that in the equilateral triangle. Consequently a Jahn–Teller distortion to C_{2v} geometry would be expected to have consequences at least qualitatively similar to those in the trimer.

Acknowledgements

This work was supported by the City University of New York PSC-BHE Research Award Program and by the National Science Foundation under grant number CHE 79-13260. Acknowledgement is made to the Donors of The Petroleum Research Fund, administered by the American Chemical Society, for partial support of this research.

References

[1] D.M. Lindsay and G.A. Thompson, Bull. Am. Phys. Soc. 25 (1980) 244.
[2] G.A. Thompson and D.M. Lindsay, J. Chem. Phys. 74 (1981) 959.
[3] D.M. Lindsay, D.R. Herschbach and A.L. Kwiram, Mol. Phys. 32 (1976) 1199.
[4] D.M. Lindsay, D.R. Herschbach and A.L. Kwiram, Mol. Phys. 39 (1980) 529.
[5] W.H. Gerber and E. Schumacher, J. Chem. Phys. 69 (1978) 1692.

[6] R.L. Martin and E.R. Davidson, Mol. Phys. 36 (1978) 1713.
[7] N.M. Atherton, Electron Spin Resonance (Wiley, New York, 1973).
[8] J.H. Freed and G.K. Fraenkel, J. Chem. Phys. 39 (1963) 326;
G.K. Fraenkel, J. Phys. Chem. 71 (1967) 139;
P.D. Sullivan and J.R. Bolton, Advan. Magn. Reson. 4 (1970) 39.
[9] Not necessarily the case if matrix effects such as a phase transition are involved. While absent in pure argon, temperature dependent structural changes have been reported for doped matrices: B.I. Swanson and L.H. Jones, J. Chem. Phys. 73 (1980) 986.
[10] J.E. Harriman, Theoretical Foundations of Electron Spin Resonance (Academic Press, New York, 1978).

REFERENCES

1. K.H. Johnson and R.P. Messmer, **J. Vac. Sci. Technol.** 11, 236 1974).

2. E.L. Muetterties and M.J. Krause, **Angew. Chem. Int. Ed. Engl.** 22, 135, (1983).

3. M. Moskovits, **Accts. Chem. Res.** 12. 229 (1979).

4. D.P. DiLella, R.H. Lipson, P. McBreen and M. Moskovits, **J. Vac. Sci. Technol.** 18, 453 (1981).

5. R.P. Messmer, **"Cluster Model Theory"** in T.N. Rhodin and G.Ertl: The Nature of the Surface Chemical Bond, (North Holland, Amsterdam 1979).

6. "Proc. 2nd. Int. Meet. Small Particles and Inorganic Clusters", **Surf. Sci.** 106 (1981).

7. G. Delacretaz, J.D. Goniere, R. Monet and L. Woste, **Appl. Phys.** B29, 55 (1982).

8. G.C. Pimentel, **Angew. Chem.** 87, 220 (1975).

9. B. Meyer, Low Temperature Spectroscopy, (Elsevier, New York, 1971).

10. G. Ozin, M. Backer, S. Mitchell and D. McIntosh, **Angew. Chem. Int. Ed. Engl.** 22, 166 (1983).

11. V.E. Bondybey and L.E. Brus, **Adv. Chem. Phys.** 41, 269, (1980).

12. J. Bourdon, Growth and Properties of Metal Clusters, (Elsevier, Amsterdam 1980).

13. G.A. Ozin, F. Hughes, D.F. McIntosh and S. Mattar, **Am. Chem. Soc. Symp. Ser.** 218, 409 (1983).

14. G.A. Ozin and S.A. Mitchell, **Angew. Chem. Int. Ed. Engl.** 22, 674 (1983), and references therein.

15. T.H. Maugh II, **Sci.** 219, 474 (1983).

16. T.H. Maugh II, **Sci.** 220, 592 (1983).

17. T.H. Maugh II, **Sci.** 219, 944 (1983).

18. W. Weltner Jr., Magnetic Atoms and Molecules (Van Nostrand Reinhold Inc., New York 1983).

19. K.A. Gingerich, D.L. Cocke and F. Miller, J. Chem. Phys. 64. 4027 (1976).

20. G.A. Ozin, Catal. Rev. Sci. Eng. 16, 191 (1977); M. Moskovits, and D.P. DiLella, J. Chem. Phys. 72, 2267 (1980); V.E. Bondybey and J.H.English, J. Chem. Phys. 73, 42 (1980).

21. A. Hermann, E. Schumacher and L. Woste, J. Chem. Phys. 68, 2327 (1978); A. Hermann., S. Leutwyler and E. Schumacher, Helv. Chim. Acta. 61, 4353 (1978): A. Hermann, M. Hofmann, S. Leutwyler, E. Schumacher and L. Woste, Chem. Phys. Lett. 62, 216 (1979).

22. T.G. Dietz, M.A. Duncan, D.E. Powers and R.E. Smalley, J. Chem. Phys. 74, 6511 (1981); M.M. Kappes, R.W. Kunz and E. Schumacher, Chem. Phys. Lett. 91, 413 (1982).

23. D.M. Lindsay, D.R. Herschbach and A.L. Kwiram, Mol. Phys. 32, 1199 1976.

24. D.M. Lindsay and G.A. Thompson, J. Chem. Phys. 77, 1114 (1982).

25. G.A. Thompson and D.M. Lindsay, J. Chem. Phys. 74, 959 (1981).

26. G.A. Thompson, F. Tischler, D. Garland and D. M. Lindsay, Surf. Sci. 106, 408 (1981).

27. D.M. Lindsay, D. Garland, F. Tischler and G.A. Thompson, Am Chem. Soc. Symp. Ser. 179, Chap. 7 (1982).

28. C. Calzaferri, Chem. Phys. 87, 443 (1982).

29. D.W. Davies and G. del Conde, Molec. Phys. 33, 1813 (1977); Faraday Discuss. 55, 369 (1973); Chem. Phys. 12, 45 (1976); P.S. Bagus, G. del Conde and D.W. Davies, Faraday Discuss. 62, 321 (1977).

30. J. Kendrick, Molec. Phys. 35, 593 (1978); J. Kendrick and I.H. Hillier, *ibid.* 33, 635 (1977); I. H. Hillier, Faraday, Discuss. 62, 231 (1977).

31. A.L. Companion, D.J. Steible Jr. and A.J. Starshak, J. Chem. Phys. 49, 3637 (1968).

32. W.H. Gerber and E. Schumacher, J. **Chem. Phys.** 69, 1692 (1978).

33. R.L. Martin and E.R. Davidson, **Molec. Phys.** 36, 1713 (1978).

34. L. Andrews J. **Chem, Phys.** 54, 4935 (1971); R.R. Smardzewski and L. Andrews. *ibid.* 57, 1327 (1972); L. Andrews, *ibid.* 50, 4288 (1969); D.A. Hatzenbuhler and L. Andrews, *ibid.* 56, 3398 (1972); L. Andrews and R.R. Smardzewski, *ibid.* 58, 2258 (1973); R.R. Smardzewski and L. Andrews, J. **Phys. Chem.** 77, 801 (1973); L. Andrews, *ibid.* 73, 3922 (1969); L. Andrews, J. T. Hwang and C. Trindle, *ibid.* 77, 1065, (1973); H. Huber and G. A. Ozin, J. **Mol. Spectrosc.** 41, 595 (1972).

35. D.M. Lindsay, D.R. Herschbach and A.L. Kwiram, Chem. **Phys. Lett.** 25, 175 (1974).

36. D.M. Lindsay, **Ph.D. Thesis**, Harvard University (1974).

37. D.M. Lindsay, D.R. Herschbach and A.L. Kwiram, J. **Phys. Chem.** 87, 2113 (1983).

38. J.E. Wertz and J.R. Bolton, Electron Spin Resonance McGraw-Hill, New York, 1972).

39. A. Carrington and A.D. McLachlan, Introduction to Magnetic Resonance (Harper and Row, New York, 1967).

40. P.B. Ayscough, Electron Spin Resonance in Chemistry (Methuen, London 1967).

41. C.P. Slichter, Principles of Magnetic Resonance (Harper and Row, New York, 1963).

42. N.M. Atherton, Electron Spin Resonance (Wiley, New York, 1973).

43. W. Gordy, Theory and Applications of Electron Spin Resonance, (Wiley, New York, 1980).

44. W. Low, Paramagnetic Resonance in Solids, Supplement 2 to Solid State Physics Series, Ed. F. Seitz and D. Turnbull (Academic Press, New York, 1960).

45. C.P. Poole Jr., Electron Spin Resonance, 2nd Ed. (Wiley, New York, 1983).

46. G. Breit and L.I. Rabi, **Phys. Rev.** 38, 2082 (1931).

47. JES-ME-3X Electron Spin Resonance Instrument Manual, Japan Electron Optics Laboratories Co., Ltd., Tokyo, Japan.

48. ER Series Users Manuals (1984), IBM Instruments Inc., Danbury, Conn.

49. A. N. Nesmeyanov, Vapour Pressure of the Chemical Elements, (Elsevier, New York, 1963).

50. D.M. Lindsay, D.R. Herschbach and A.L. Kwiram, Mol. Phys. 32, 1190 (1976).

51. D.A. Garland and D.M. Lindsay, J. Chem. Phys. 78, 2813 (1983).

52. D.A. Garland and D.M. Lindsay, J. Chem. Phys. 80, 4761 (1984).

53. P. Kusch and V.W. Hughes, Handbuch der Physik, edited by S. Flugge (Springer, Berlin 1959).

54. C.K. Jen, V.A. Bowers, E.L. Cochran and S.N. Foner, Phys. Rev. 126, 1749 (1962).

55. S.N. Foner, E.L. Cochran, V.A. Bowers and C.K. Jen, J. Chem. Phys. 32, 963 (1960).

56. C.S. Barrett and L. Meyer, J. Chem. Phys. 41, 1078 (1969).

57. F.J. Adrian, J. Chem. Phys. 32, 972 (1960).

58. J.H. Ammeter and D.C. Schlosnagle, J. Chem. Phys. 59, 4783 (1973).

59. D.Y. Smith, Phys. Rev. 133, A1087 (1964).

60. H. C. Longuet-Higgins, U. Opik, M.H.L. Pryce and R.A. Sacks, Proc. Roy. Soc. (London) A244, 1 (1958).

61. H.C. Longuet-Higgins, Adv. Spectrosc. 2, 429 (1961).

62. M.D. Morse, J.B. Hopkins, P.R.R. Langridge-Smith and R.E. Smalley, J. Chem. Phys. (1983).

63. W.H. Gerber, Ph.D. Thesis, University of Bern, Switzerland (1980).

64. J.G. Fripiat, K.T. Chow, M. Boudet and K.H. Johnson, J. Mol. Catal. 1, 59 (1975).

65. R.N. Yardley and G.G. Balent-Kurte, **Chem. Phys.** 16, 287 (1976).

66. D.W. Davies and G. DelConde, **Chem. Phys.** 12,45 (1976).

67. P.S. Bagus, G. DelConde and D.W. Davies, **Faraday Discuss. Chem. Soc.** 62, 321 (1977).

68. G.A. Thompson, F. Tischler and D.M. Lindsay, **J. Chem. Phys.** 678, 5946 (1983).

69. S.C. Richtsmeter, D.A. Dixon and J.L. Gole, **J. Chem. Phys.** 86, 3942 (1982).

70. B.R. Pickup, **Proc. R. Soc. London Ser. A.** 333, 69 (1973).

71. M.R. Hoare and P. Pal, **Natur. Phys. Sci.** 230, 5 (1971); *ibid*. 236, 35 (1972).

72. M.R. Hoare and P. Pal, **Adv. Phys.** 20, 161 (1971).

73. M.R. Hoare, **Adv. Chem. Phys.** 40, 49 (1979).

74. D. Plavsic, J. Koutechy, G. Pacchioni and V. Bonacic-Koutecky, **J. Phys. Chem.** 87, 1096 (1983).

75. P. Fantucci and J. Koutecky and G. Pacchione, **J. Chem Phys.** 80, 325 (1984).

76. C.S. Barrett and L. Meyer, **J. Chem. Phys.** 41, 1078 (1969).

77. G.L. Pollack, **Rev. of Mod. Phys.**, July 1964, 748.

78. A.R. Boates, J.R. Morton, K.F. Preston and S.J. Strach, **J. Chem Phys.** 71, 388 (1979).

79. E. Simanek and R. Orbach, **Phys. Rev.** 145, 191 (1966).

80. H. Klein, U Scherz, M. Schulz, H. Setyons and K. Wisznewski, **Z. Physik. B.** 28, 149 (1977).

81. L. Pauling, **Proc. R. Soc. London Ser. A** 196, 343 (1949).

82. C. Kittel, Introduction to Solid State Physics (Wiley, New York, 1976).

83. L. Wilk, A.H. MacDonald and S.H. Vosko, Can. J. Phys. 57, 1965 (1979); A.H. MacDonald, K.L. Liu, S.H. Vosko, and L. Wilks, *ibid*. 59. 500 (1981).

84. C.E. Moore, **Atomic Energy Levels**, Natl. Bur. Stand. (U.S.) Circ. 467 (1952).

85. H. Figger, W. Schrepp and Xu-hui Zhu, J. Chem. Phys. 79 , 1320 (1983).

86. W. Kanzig and M. Labhart, J. Phys. (Paris) 37, C7 (1976).

87. F.P. Billingsley II and C. Trindle, J. Phys. Chem. 76, 2995 (1972).

88. D.H. Liskew and H.F. Schaeffer III, J. Amer. Chem. Soc. 93, 6734 (1971).

89. L. Andrews, J. Chem. Phys. 50, 4288 (1969).

90. S. V. O'Neil, C. F. Bender and A.F. Schaeffer III, Chem. Phys. 59, 3608 (1973).

91. D.T. Grow and R. M. Pitzer, J. Chem. Phys. 67, 4019 (1977).

92. M.H. Alexander, J. Chem. Phys. 69, 3502 (1978).

93. A.D. Walsh, J. Chem. Soc. (Lond). 16, 2260 (1953).

94. M.E. Jacox and D.E. Milligan, J. Mol. Spectrosc. 42, 495 (1979).

95. J.L. Gole and E.F. Hayes, J. Chem. Phys. 57, 360 (1972).

96. D.E. Henshaw, Phys. Rev. 111, 1470 (1958).

97. C.S. Barrett and L. Meyer, J. Chem. Phys. 41, 1078 (1964).

98. G.L. Pollack, Rev. Mod. Phys. 36, 748 (1964).

99. W. Kanzig and M.H. cohen, Phys. Rev. Lett. 3, 509 (1959).

100. P.H. Kazai, J. Chem. Phys. 43, 3322 (1965).

101. H.R. Zeller and W. Kanzig, Helv. Phys. Acta. 40, 873 (1967); H.R. Zeller, R.T. Shuey and W. Kanzig, J. Phys.(Paris), C4, 81 (1967).

102. F.J. Adrian, E.L. Cochran and V.A. Bowers, J. Chem. Phys. 59, 56 (1974).